FROM DESIGN TO APPLICATION: THE SYNTHESIS OF METAL-ORGANIC FRAMEWORKS (MOFS) WITH AN ENVIRONMENTALLY BENIGN SOLVENT FOR APPLICATIONS IN ENVIRONMENTAL PROTECTION

by

© Jinfeng Zhang

A thesis submitted to the

School of Graduate Studies

in partial fulfilment of the

requirements for the degree of

Master of Science

Department of Chemistry

Memorial University of Newfoundland

December 2017

St. John's Newfoundland and Labrador

Abstract

Metal-organic frameworks (MOFs) are a series of porous materials made of well-organized inorganic metal nodes linked *via* organic ligands (linkers). MOFs have gained particular attention due to their applications in gas adsorption and separation, selective sorption of harmful chemicals, catalysis, energy, sensing, bioscience, and electronics.

The thesis will focus on two different aspects of MOFs. Briefly, in the first portion of the thesis, a less-toxic solvent than *N,N*-dimethylformamide (DMF) can be used to make MOFs will be demonstrated. In the latter portion of the thesis, my efforts to incorporate organic moieties into MOFs for sulfur dioxide sequestration will be described.

With regard to the use of less-toxic solvents, it should be noted that with notable exceptions (*e.g.*, mechanochemical, water-based, and electrochemical), the synthesis of MOFs is often carried out at elevated temperature using DMF or *N,N*-diethylformamide (DEF) as the solvent. However, the industrial-scale synthesis of MOFs from DMF/DEF may generate significant amounts of DMF waste, which can exhibit reprotoxicity and end-of-life issues associated with the formation of NO_x upon incineration. With the introduction of the Registration, Evaluation and Authorization of Chemicals (REACH) legislation in the European Union, there is a growing trend towards safer production and use of chemicals by industry. As such, it is crucial to develop green/sustainable methods of synthesizing MOFs.

Dihydrolevoglucosenone (Cyrene), a green bioderived solvent from waste cellulose, was applied to the synthesis of MOFs. The MOF, HKUST-1, exhibited a larger

Brunauer–Emmett–Teller (BET) surface area than HKUST-1 synthesized with DMF. Four additional archetypal MOFs were also synthesized to verify the universal application of Cyrene in the synthesis of MOFs. However, their BET surface areas were lower than DMF-made MOFs. It was observed that an aldol-condensation product of two Cyrene molecules, in addition to Cyrene trapped within the pores, were responsible for the lower-than expected surface areas. The use of Cyrene has led to a series of design principles that eliminate the need for problematic solvents such as DMF and can be applied to the synthesis of a wide range of MOFs.

With regard to sulfur dioxide sequestration, it should be noted that sulfur dioxide, a colorless gas belonging to SO_x family, yields detrimental effects *via* inhalation or absorption. Since MOFs are ideal sorbents for toxic gases, in Chapter 3, I will continue along the theme of reprotoxicity and end-of-life issues by designing MOFs which have the potential to chemically react with sulfur dioxide. Unlike the *de novo* synthetic pathways in the Chapter 2, the Chapter 3 will demonstrate how solvent-assisted linker exchange (SALE) and solvent-assisted linker incorporation (SALI) can be used to make MOFs with the ideal functionalities for sulfur dioxide sequestration.

In Chapter 3, the main focus of the work was to introduce the butadiene functional groups into different MOFs, namely UiO-66, UiO-66-MA (muconic-acid-functionalized UiO-66), MOF-808, MOF-808-BS (butadiene-sulfone-functionalized MOF-808) and MOF-808-BD (butadiene-functionalized MOF-808), the SALI method was vitalized to determine if the butadiene group could undergo a cheletropic reaction in the presence of sulfur dioxide inside the MOF. All MOFs were exposed to a constant flow of sulfur dioxide, the UiO-66-MA was observed to take up three times more sulfur dioxide than the unfunctionalized parent UiO-66. For the MOF-808 series, surprisingly,

the unfuctionalized MOF-808 was able to absorb more than two times the sulfur dioxide than MOF-808-BD, and five times higher than MOF-808-BS, respectively. This suggests that the terminal waters and hydroxide groups are responsible for the enhanced uptake. Despite the improved uptake of sulfur dioxide in UiO-66-MA and MOF-808, nuclear magnetic resonance (NMR) and infrared (IR) data indicate that no chemical change occurred to the butadiene-functionalized group, which suggests that a cheletropic reaction did not occur.

To my family.

Acknowledgements

This thesis was finished at the end of my master degree. However, it is just stage work of the two years I spent in the chemistry department of Memorial University of Newfoundland. Without all the people and help I received during my time at Memorial, I could not have had the opportunity to reach so far and accomplish so much.

Among all the help, I would like to thank my outstanding fantastic supervisor, Dr. Michael Katz, who influenced me deeply in both academia and life. For all these days, he mentored and taught me the skills of how to be a wonderful chemist. Mike, thank you for all the time we worked together tackling this unknown world, your unique and optimistic way to deal with problems always inspire and encourage me to go further at all the dark times. All the skills you taught me about either experiment itself, or treatment about all the experiment results lead me to approach the vision you set in front of me and other students in our group. Your excellent leadership gave me an independent, educational, fun, flexible, and fulfilling research experience. Thank you for making me a far better chemist.

I would like to thank my two committee professors, Dr. Francesca Kerton, and Dr. Travis Fridgen, for all the knowledge about green chemistry and the help for all the experiment issues.

I would like to say special thanks to Dr. Christopher Kozak, who saved my dream of being a chemist. Thank you for offering me so many opportunities. Thank you helping me to be an integral part of chemistry department, and thank you for teaching me all about organometallic chemistry; all the metal centers and ligands fascinate me

deeply.

Dr. Dave Davidson, thank you for your kind support on all my questions and issues about all my NMR results. Your excellent explanation of the beauty of NMR will never fade away in my memory. Dr. Celine Schneider, thank you for your introduction to the knowledge of NMR and thank you for lending me books. Dr. Wanda Aylward, I am very appreciating your effort of measuring all my PXRDs. Dr. Kelly Hawboldt, thank you for letting me use your gas adsorption equipment. Adam Beaton, Linda Winsor, and Nick Ryan, thank you all for teaching me how to use the TGA, MS, and UV-VIS, respectively.

I would like to thank all my collaborators. Dr. Andrew Hunt, thank you for your Cyrene sample and the help offered related to the Cyrene project; the Cyrene paper would never have been published without your effort. Dr. Jared DeCoste, thank you for all the effort you put in the micro-breakthrough reaction measurements; your support is always utmost on my mind when I talked about the sulfur dioxide project.

To all my colleagues, peers, and friends (inside and outside of the chemistry department), especially former and current members of the MOFia group, thank you for offering the happy, supportive, and friendly atmosphere all the time. The support and discussions during these two years will always be a fantastic memory to me.

I would like to thank the department of chemistry, and Memorial University School of Graduate Studies for the academic and financial support all the time. Without this, none of this would be possible.

This work is dedicated to my family, to my friends, and to MOFia group, thank you for the long-time trust, encourage, understand, and support.

Contents

List of Tables

List of Figures

List of Abbreviations and Symbols

δ	chemical shift
δ_{D}	dispersion interaction parameter
δ_{P}	polar interaction parameter
δ_{H}	hydrogen bonding interaction parameter
ρ	density
d	doublet
dd	doublet of doublets
ddt	doublet of doublet of triplets
dt	doublet of triplets
m	multiplet
q	quartet
qd	quartet of doublets
t	triplet
td	triplet of doublets
J	coupling constant
V_m	molar volume
4,4'-BPY	4,4'-bipyridine

AcOH	acetic acid
ADC	acetylenedicarboxylic acid
ANT	adiponitrile
A.U.	arbitrary unit
ATR-FT-IR	attenuated total reflection Fourier-transform infrared
BASF	Baden Aniline and Soda Factory
BDC	terephthalate
BET	Brunauer-Emmett-Teller
BP	boiling point
BPCN	4,4'-biphendicarbonitrile
BPDC	biphenyl-4,4'-dicarboxylate
BPDS	4,4'-biphenyldisulfonate
BTC	benzene-1,3,5-tricarboxylate
CCDC	Cambridge Crystallographic Data Center
Cyrene	dihydrolevoglucosenone
COSY	correlation spectroscopy
CPO	coordination polymer of Oslo
DABCO	1,4-diazabicyclo[2.2.2]octane
DABSO	1,4-Diazabicyclo[2.2.2]octane bis(sulfur dioxide) adduct
DBU	1,8-diazabicyclo(5.4.0)undec-7-ene
DCM	dichloromethane

DEF	*N,N*-dimethylformamide
DMAc	*N,N*-dimethylacetamide
DMSO	dimethyl sulfoxide
DOT	dioxidoterephthalate
Et	ethyl
GC-MS	gas chromatography-mass spectrometry
HKUST-1	Hong Kong University of Science and Technology-1
HPMO	pyrimidone
HSQC	heteronuclear single-quantum correlation spectroscopy
Im	imidazolate
INT	isonicotinic acid
IR	infrared
KAT	Kamlet-Abboud-Taft
MOFs	metal-organic frameworks
MeOH	methanol
MIL	Materials from Institute Lavoisier
MP	melting point
NMR	nuclear magnetic resonance
NMP	*N*-methylpyrrolidinone
NCPs	nanoscale coordination polymers
NDC	1,4-naphthalenedicarboxylate

NDS	2,6-naphthalenedisulonate
NOESY	nuclear overhauser effect spectroscopy
NU	Northwestern University
OAc	acetate ion
ODS	oxidation desulfurization
PCN	porous coordination network
PCPs	porous coordination polymers
PEG	poly(ethylene glycol)
PXRD	powder X-ray diffraction
PRM	pyrimidine
REACH	the Registration, Evaluation and Authorization of Chemicals
SA	surface area
SALEN	a contraction for salicylaldehyde and ethylenediamine
STP	standard temperature and pressure
SVHC	substances of very high concern
TGA	thermogravimetric analysis
TICs	toxic industrial chemicals
TPDC	*p*-terphenyl-4,4"-dicarboxylic acid
UiO	Universitetet i Oslo
VT	variable temperature
wt %	percentage by weight

ZIF zeolitic imidazolate framework

Chapter 1

Introduction

1.1 Porous Materials

Porous material is a type of material that contain a non-closed-packed skeletal framework. The unused space that is formed from the non-closed-packed framework is termed the void space, or the pore of the material. These pores are normally filled with a fluid, either liquid or gas.[1,2] Porous materials are an innovative research area due to their unique properties and associated applications in the field of applied science and engineering.[3,4] The applications of porous materials include filtration,[5] adsorption,[6] catalysis,[7] and gas storage,[8] to name a few.[9] Some common porous materials include, but are not limited to, zeolites, activated carbon, and metal-organic frameworks (MOFs).

Zeolites (Figure 1.1 left) are hydrated aluminosilicate minerals made from interlinked tetrahedral units of alumina and silica, that is, silicon or aluminum ions surrounded by four oxygen ions in a tetrahedral configuration.[10,11] Activated carbon

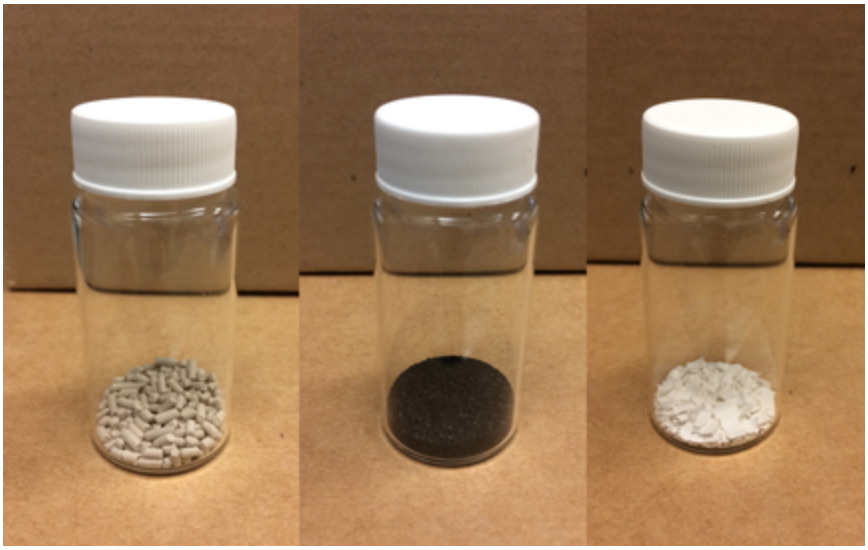

Figure 1.1: Zeolites, Activated Carbon and MOFs

(Figure 1.1 middle) is a form of carbon processed *via* physical or chemical activation to have small, low-volume pores that increase the surface area available for adsorption or chemical reactions.[12] One of the most recent additions to the porous material team is MOFs, the focus of this thesis (Figure 1.1 right).

1.1.1 Metal-Organic Frameworks

MOFs are a family of porous materials made of well-organized inorganic metal cations, clusters, or neutral metals (nodes) linked to one another by organic ligands (linkers) *via* coordination bonds (Figure 1.2).[13,14] The organic linkers feature Lewis-basic groups such as carboxylates, phosphonates, amines, phenolates, pyridyls, sulfones, and *N*-heterocyclic compounds.[15] Moreover, these organic linkers can be functionalized as shown in Figure 1.2. Owing to the large database of available organic linkers, their derivatives, and metal nodes, the physiochemical properties of MOFs can be

judiciously chosen for a particular application.[16–20]

Frustratingly, especially for new researchers in the field, scientists have spent considerable amount of time naming MOFs using a trivial naming system unrelated to the components of the MOFs.[21] Some MOFs were named after the university they were first synthesized in (*e.g.*, UiO (University of Oslo),[22,23] NU (Northwestern University),[24] and MIL (Materials from Institute Lavoisier)[25]). Some of the names are due to the family of MOFs that they are related to (*e.g.*, PCN (Porous Coordination Network),[26] MOF,[27] and ZIF (Zeolitic Imidazolate Framework)[28]). Some MOFs even have the same components but different names (*e.g.*, PCN, UiO, and some NU MOFs are all made from Zr-clusters and carboxylate-based linkers; MOF-74 is also called CPO-27).[22,29–35]

1.1.2 Applications of MOFs

The number of MOFs synthesized and characterized have increased steadily in the past two decades. The driving force of this enormous enthusiasm lies in the versatility of the metal-organic coordination chemistry and the wide range of organic linkers as well as their functionalities. With this in mind, researchers have tuned MOFs toward applications in gas adsorption and separation,[36–41] selective sorption of harmful chemicals,[42–44] catalysis,[45–48] energy storage,[49,50] sensing,[51,52] bioscience,[53] biomedical,[54,55] and electronics.[56–58]

1.1.2.1 Gas Adsorption and Separation

High porosity, tunable pore sizes, and even topology make MOFs an ideal gas sorbent candidate over other materials such as activated carbon and zeolites. For this reason,

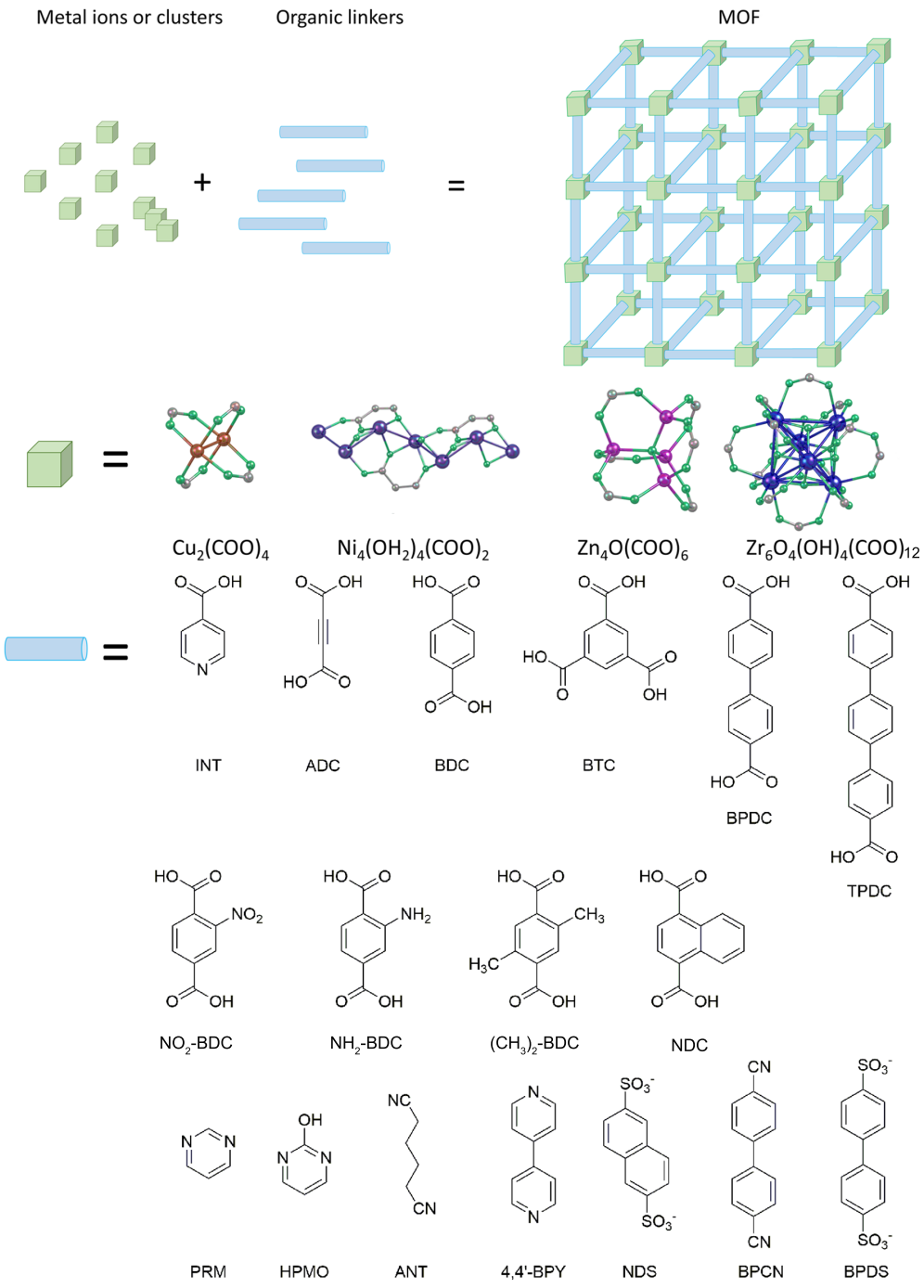

Figure 1.2: Tunable Metal Nodes (Green Boxes) [Cu, Red; Ni, Dark Blue; Zn, Purple; Zr, Blue; C, Grey; O, Green] and Organic Linkers (Blue Bars).

even from the early days of MOF research, numerous research groups focused on gas adsorption and separation.[18,59–61] In the dictionary of MOF chemistry, activation is a key aspect to realize high porosity. The goal of activation is to remove guest molecules occupying the pore of the MOF while maintaining the structural integrity of the material (*i.e.*, preventing structural collapse). This is often achieved *via* mild heating, vacuum, flowing another gas through the material, supercritical drying, or the combination of several techniques.[62]

Adsorption, which represents the enrichment of one or more components (guests) in the MOF (host), involves the accumulation of excess of molecules at the interfacial between two phases. Adsorption is a consequence of interface energy.[63] When a surface is created, interface energy is used to quantify the disruption of intermolecular bonds that occur.

Isotherms, which illustrate the amount of adsorbate (host) on the adsorbent (guest) as a function of its pressure, or concentration, at constant temperature, are excellent tools to study adsorption. Adsorption processes are classified into two types, chemisorption and physisorption, according to the nature of the bonding involved between host and guest. Specifically, when weak van der Waals forces are dominant, physisorption occurs. However, when the formation of new chemical bonds are dominant, then chemisorption occurs.

Hydrogen, the carbon free high mass energy density carrier, abundantly available from water, is an ideal replacement for the combustion of fissile fuels. However, hydrogen storage is still an issue as this chemical is a gas under ambient temperature and pressure; either high pressure, low temperature, or both are required for transporting. Therefore, low cost, light weight, lower pressure, and mild-storage-condition

materials are needed. To that end, several MOFs have been previously synthesized and their hydrogen adsorption capacity investigated.[37,64–66]

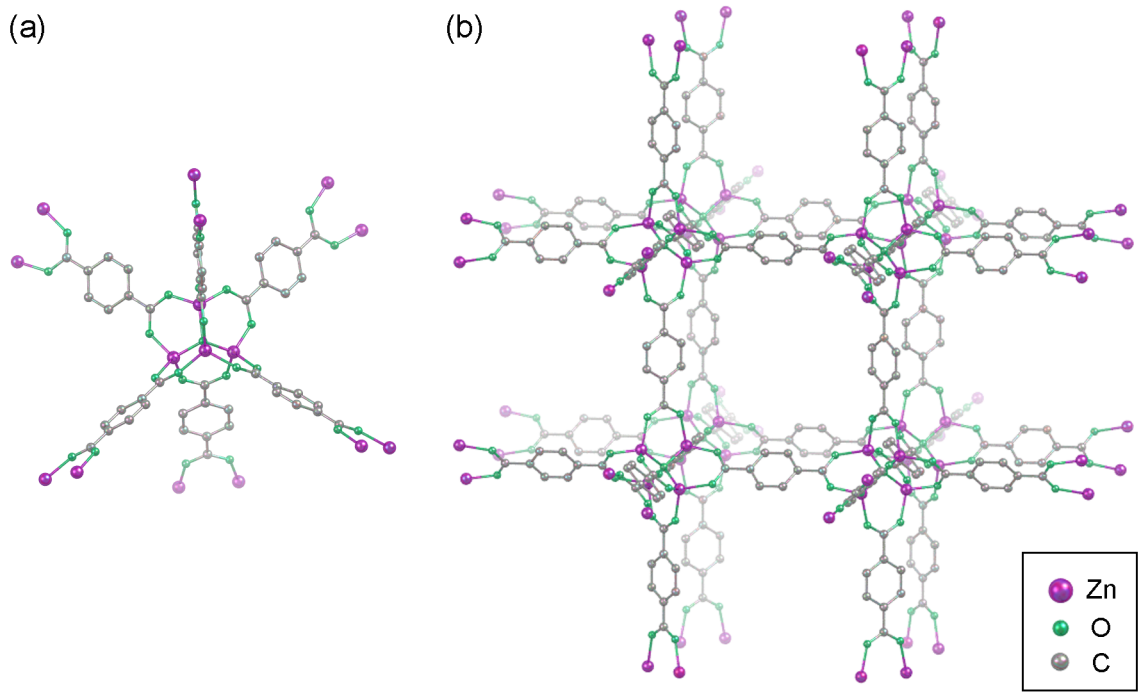

Figure 1.3: (a) Representative Fragment Structure of MOF-5 with Zn_4O Clusters Coordinated with Terephthalate Linkers. (b) 3-Dimensional Structure of MOF-5 Showing the Cubic Pore.

MOF-5, a cubic carboxylate-based framework containing a Zn_4O node (see Figure 1.3), was found to be a fantastic hydrogen adsorption candidate.[67] One of the most interesting things about MOF-5 in this regard is that the hydrogen uptake is dependent on a combination of the synthetic and activation method (the method by which the pores are emptied prior to gas adsorption measurements) applied.[61,67–71] Yaghi and co-workers found that MOF-5 has a hydrogen adsorption capacity of 4.5 wt %;

at the time, the U.S. Department of Energy has a target hydrogen storage capacity of 6.5 wt %.[61] However, if MOF-5 is properly activated,[62] thereby removing all the pore-bound guests, a 7.1 wt % hydrogen uptake can be achieved at 77 K and 40 bar. Remarkably, the hydrogen fill time can be as short as two minutes for a cold sample (77 K). Furthermore, the capacity of hydrogen storage in MOF-5 is maintained for 24 complete adsorption-desorption cycles. While 24 cycles may not seem high from an industrial point of view, considering MOF-5 is one of the first MOFs, its ability to function for so long clearly demonstrates what could be achieved with MOFs if linkers and nodes are selected for a desired application.

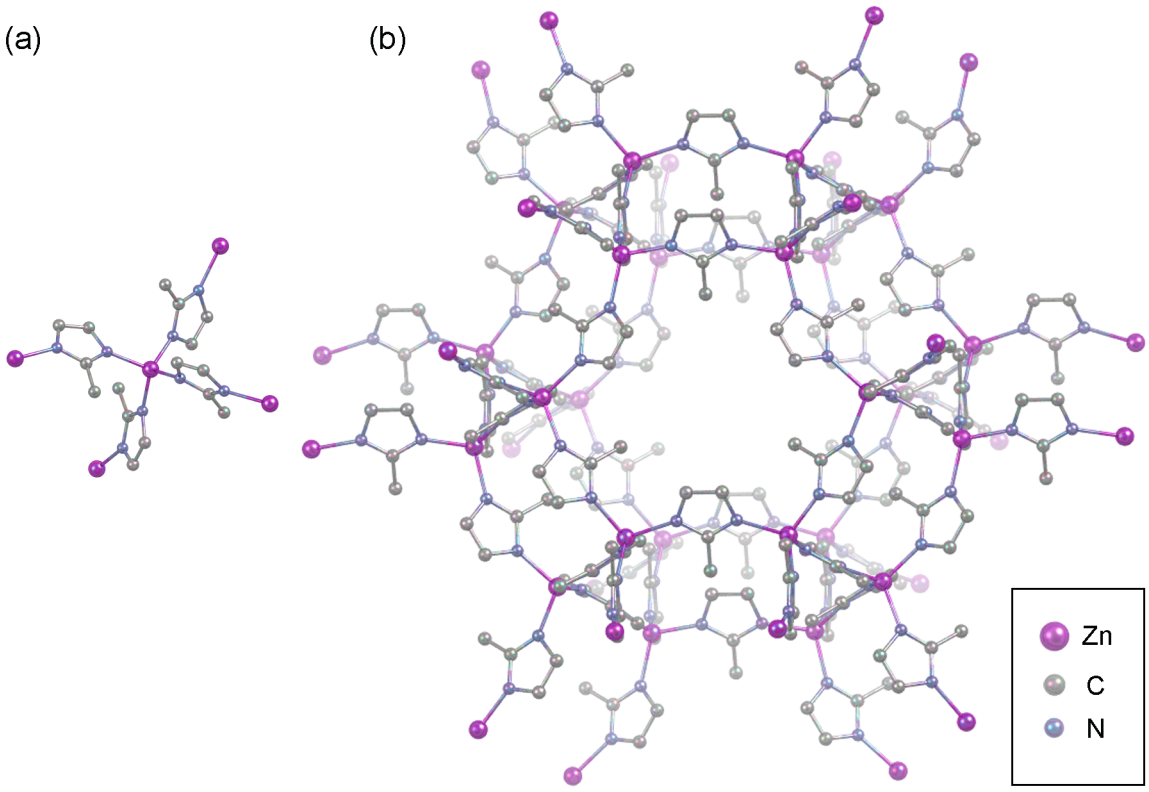

Figure 1.4: (a) Representative Fragment Structure of ZIF-8 with Zn(II) Cation Nodes Coordinated with Imidazolate Linkers. (b) 3-Dimensional Pore Structure of ZIF-8.

To illustrate the ability of linker and node modifications to address the challenges with hydrogen storage, numerous other MOFs, beyond MOF-5, were designed and synthesized. For example, ZIF-8, as seen in Figure 1.4, a MOF made by zinc ions coordinated by four imidazolate rings, was reported with a 3.3 wt % hydrogen storage capacity at 77 K and 30 bar, while NU-100, as shown in Figure 1.5, a MOF with bridging Cu_2-paddlewheel units with hexacarboxylate linkers ($H_6\mathbf{L}$) ($[Cu_3(\mathbf{L})(H_2O)_3]$), was found to have a 9.0 wt % hydrogen gas storage capacity at 77 K and 56 bar.[71,72] The varity of hydrogen uptake is mostly related to the porosity (*i.e.*, the amount of free space) of the MOF. The simulated surface areas of these three MOFs range between 3500 and 6500 m^2g^{-1}. However, the experimental data obtained may differ due to incomplete removal of guest molecules, partial loss of structural integrity *via* improper activation, inaccessible corners of the structure to the guest, or a combination of these factors.[72]

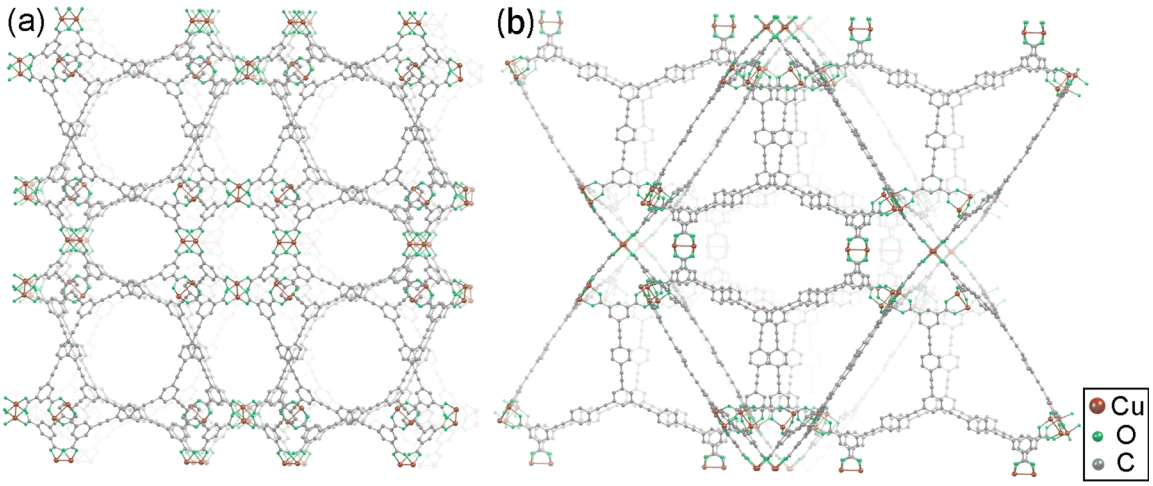

Figure 1.5: Variable Angles of Pore Structure of NU-100

Another fuel source that is commonly featured in MOF research is natural gas.

As one of the alternative petroleum-based fuels, natural gas has a great advantage due to its nearly 50 % lower carbon dioxide production per unit of energy compared to coal.[73] Like hydrogen, the storage of natural gas is one of the aspects which limited its application in transportation vehicles. Recently, several MOFs were designed, and characterized by their methane gas, the primary component of natural gas, uptake capacities.[8,74–76] Cu-based MOF HKUST-1 [$Cu_3(BTC)_2$] (Figure 1.6) exhibits a total volumetric methane storage capacity of 301 cm^3(STP) cm^{-3} at 270 K,[‡‡] which is

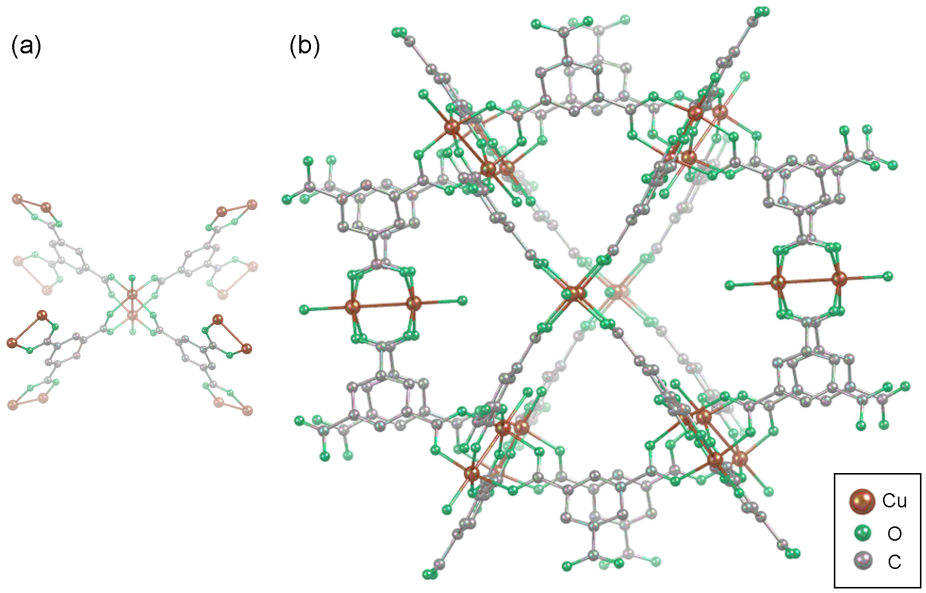

Figure 1.6: (a) Representative Fragment Structure of HKUST-1 with Cu(II) Cation Nodes Coordinated with BTC Linkers. (b) 3-Dimensional Pore Structure of HKUST-1 Showing How Cu_2-paddlewheels Connect to One Another *via* 1,3,5-Benzenetricarboxylate.

[‡‡] cm^3(STP) cm^{-3} : the standard temperature and pressure equivalent volume of methane per volume of the adsorbent material.

higher than any other MOFs reported so far.[74]

On the tail-end of a perfect combustion, carbon dioxide and water are the waste products. Carbon dioxide is credited as the primary anthropogenic greenhouse gas responsible for climate change.[77,78] Thus, selective carbon dioxide adsorption has been proposed in which MOFs play the role as porous sorbents.[38,79] To illustrate the importance of MOFs in this field, MOF-5, the parent MOF to the field of MOFs, exhibits a capacity of 58.0 wt % carbon dioxide at 10 bar and 273 K.[80]

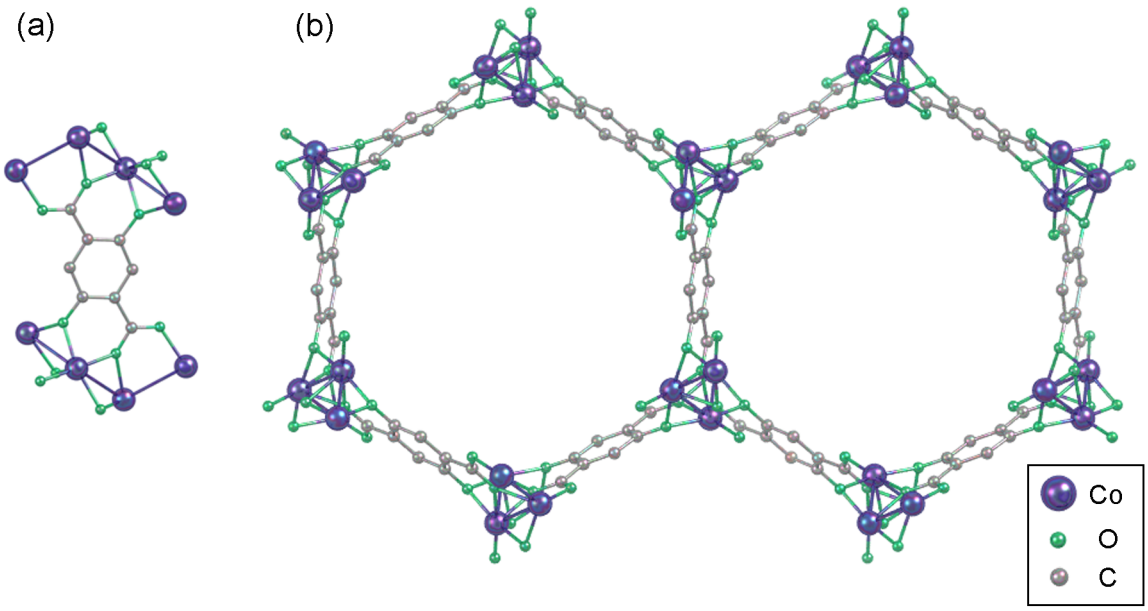

Figure 1.7: (a) Representative Fragment Structure of MOF-74 with Metal Cation Nodes Coordinated with Tetra-Deprotonated DOT Linkers. (b) Viewed Along C-Axis, Schematic Structure of MOF-74.

The applications of MOFs are not limited in pre- and post-combustion. Conventional hazardous chemicals, such as ammonia, sulfur dioxide, hydrogen sulfide, and carbon monoxide, to name a few, are responsible for environmental air pollution.

The use of toxic industrial chemicals (TICs) in warfare makes TICs hazardous to both environment and human beings.[81–84] As an outstanding sorbent, MOFs have been featured in remediation of TICs. Yaghi and co-workers studied and calculated the capacity of MOF-74's, (Figure 1.7), a series MOFs made by coordinated metal ions with dioxideterephthalate (DOT) linkers [M_2(DOT)], towards ammonia, cyanogen chloride, and sulfur dioxide uptake in the presence of humidity. Their results illustrate that MOF-74 represents much better uptakes than conventional sorbents like activated carbon.[85]

1.1.2.2 Catalysis

The ability to tune the pore/aperture sizes of MOFs allows for size control on the catalyst substrates. Substrates that are larger than the pore/aperture size cannot enter the MOF and undergo catalysis.[86] This allows for a mixture of compounds to undergo catalysis in such a way that some will react faster as they are able to access the catalyst in the framework while the others will be slower because they only have access to the external surface area-available catalyst.[30,48,87] Based on these points, researchers have put a significant amount of efforts toward MOF-based catalyst design and investigation.[48,88–90]

The chemical and/or thermal structural stability of MOFs made them an ideal catalyst in chemistry. The metal nodes play an important role and may show better stability compared to other catalytic systems, which may suffer aggregation and/or deactivation under certain conditions. To illustrate the efficacy of MOFs as heterogeneous catalysts *vs.* homogeneous catalysts, David Farrusseng and co-workers compared the Friedel-Crafts reaction between *tert*-butyl chloride and toluene/biphenyl.

In comparison with the typical Lewis-acid $AlCl_3$ catalyst, MOF-5 (Figure 1.3), the archetypal cubic MOF with a tetranuclear-zinc(II) oxo cluster Zn_4O as the node, demonstrated better catalytic activity than $AlCl_3$.[91]

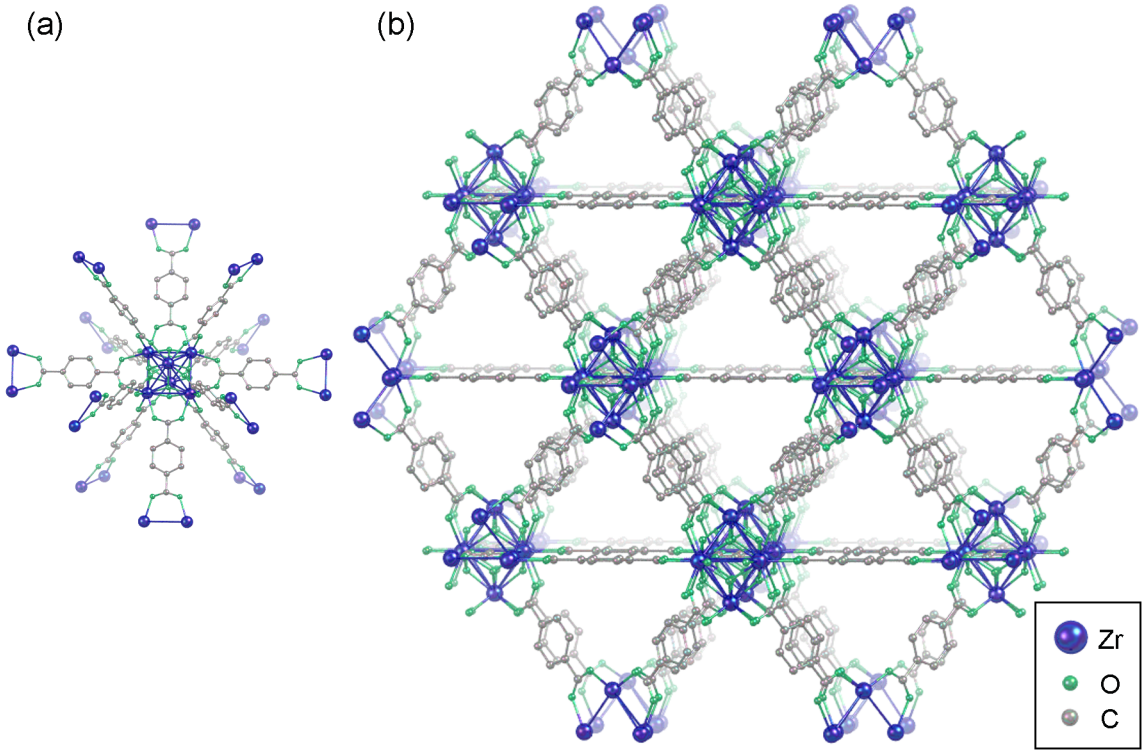

Figure 1.8: (a) Representative Fragment Structure of UiO-66 with Zr Cluster Nodes Coordinated with Terephthalate Linkers. (b) Schematic Structure of UiO-66.

The catalytic ability of the metal cation can be tuned by adjusting the pore chemistry *via* modifying the organic linkers to longer linkers, linkers with new functional groups (*e.g.*, -NH_2, -OH), or both. This has been well demonstrated with UiO-66 (Figure 1.8). UiO-66 is a Zr-containing MOF composed of $[Zr_6O_4(OH)_4]^{12+}$ clusters linked by BDC dianions. By substitution of BDC in UiO-66 with 2-aminoterephthalic acid (NH_2-BDC), a photocatalytic MOF, UiO-66-NH_2 was obtained.[22] UiO-66-NH_2

has been shown to be a photocatalyst for carbon dioxide reduction under visible-light irradiation.[92]

The concept of catalysis can be further extended to fuel sources. For example, the quality of diesel, a fuel largely used in heavy engineering machines and transportation vehicles, is a critical factor with regards to its combustion efficiency and gas emission. As sulfur compounds are the main impurities in diesel, desulfurization is a key step in diesel treatment. Balula and co-workers discovered that UiO-66 (Figure 1.8) can be applied to effectively remove sulfur compounds within diesel *via* oxidative desulfurization.[93] The MOF was robust enough to undergo three consecutive oxidative desulfurization cycles without any significant catalytic activity loss. Furthermore, the MOF was examined using commercial diesel sources and an 81 % desulfurization rate was achieved.

1.1.2.3 Sensing

The desire of a real-time monitoring for chemical components, pressure, or concentration has catalyzed the invention of chemical sensors. These devices were designed to transfer chemical information into useful signals in a short time without large instrumentation (*e.g.*, hand-held detectors *vs.* a GC-MS). As with so much of the early work in MOFs, HKUST-1 (Figure 1.6) was found to be an excellent pyridine sensor with a diffusion coefficient of 1.5×10^{-19} m^2s^{-1} and an activation energy for diffusion of 0.78 eV (compared to the theoretical binding energy between pyridine and MOF-lattice of 0.69 eV) at ambient temperature.[94] The field of sensing has expanded to examine more dangerous molecules, such as nitro-aromatics, by a series of fluorescence-based MOFs.[95] Ghosh and co-workers demonstrated that their

Cd-based MOF exhibited excellent selectivity towards 2,4,6-trinitrophenol over 2,4,6-trinitrotoluene and 2,4-dinitrotoluene.[96]

1.2 Motivation of This Thesis

1.2.1 Alternative Solvents

With the effort of scientists and engineers, there are near-limitless opportunities for researchers to design advanced porous materials by combining linkers and nodes. Most often, MOFs are synthesized under standard methods including solvothermal, hydrothermal, electrochemical, and mechanochemical synthesis.[97]

1.2.1.1 Prototypical Solvothermal Synthesis

Most MOFs were synthesized at elevated temperatures in a closed vessel under autogenous pressure with dimethylformamide (DMF) as the solvent, or with diethylformamide (DEF) to improve crystal growth.[98] These solvents were chosen due to their high boiling points as well as their beneficial acid-base chemistries, as illustrated in Figure 1.9. The by-product of MOF formation is 2-equivalent of acid (assuming a dicationic metal node such as Zn(II) or Cu(II)). As DMF is heated, it breaks down to form dimethylamine, a base that can be used to react with the produced acid. Without this reason, the formed highly acidic environment during MOF formation would break the M-linker bonds and reverse MOF formation. Thus, the reactivity of the solvent is critical in solvent choice. The advantage of high-boiling solvents is that the kinetics of crystal growth can be modulated over a wide temperature range (20 - 200 °C are typical temperatures for MOF formation).

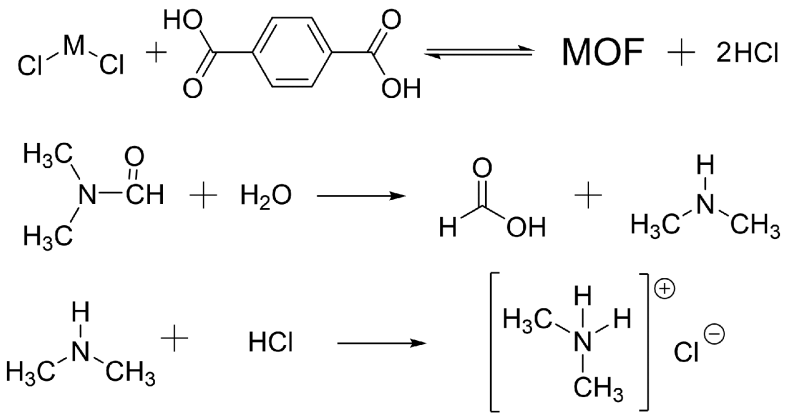

Figure 1.9: An Example of Acid-Base Chemistry in the Synthesis of MOFs.

The typical MOF synthesis is very capable of yielding sufficient material for lab-scale research (50 mg - 10 g scale). However, one of the challenges of MOF synthesis is scaling up the processes toward industrially-relevant yields (more than 10 kg at a time).[99] Temperature variations in large solvent containers, changes in head space pressures, and the quality of the DMF can play a critical role in producing MOFs with optimal yield and porosity. For example, MOF-74 (Figure 1.7), a MOF that has been featured in carbon dioxide adsorption application,[38,79,100–105] can be made using 30.0 mL of solvent ($V_{DMF}/V_{H_2O}/V_{MeOH}$=1/1/1), 217.0 mg of metal salt, and 43.0 mg of linker at 100 °C.[35] It has been observed that two seemingly identical reaction containers will exhibit yields ranging from 20.0 - 140.0 mg. It is very likely that these variations are due to small changes in temperature inside the reaction vessel.

1.2.1.2 Alternative Methods

With the challenges of MOF synthesis delineated above, many researchers have focused on unconventional synthesis. These routes allow for control of particle sizes

(*e.g.*, large crystals suitable for single crystal X-ray diffraction *vs.* microcrystalline powders which are better suited for filling a gas cylinder), oxidation states of metals, and even scale-up processes which may be otherwise challenging to achieve with traditional solvothermal conditions. To address these, alternative synthesis routes have been investigated.[97]

I. Electrochemical Synthesis

The first report of electrochemical synthesis of MOFs consist of the Cu- and Zn-carboxylates MOFs (HKUST-1 and MOF-5) synthesized by BASF.[106] The organic linker and conducting salt, not the same as the metal nodes, were dissolved in a reaction medium. The metal ions that formed the node are subsequently introduced continuously *via* anodic dissolution. Protic solvents were used to avoid the deposition of metals on the cathode. There has been a lot of work focused on examining the synthesis of MOFs *via* this method.[107–110] The use of electrochemical method to make MOFs allows for an advantage to conventional synthesis in which different oxidation states, or mixed oxidation states inside MOFs can be attained.[56,58]

II. Mechanochemical Synthesis

Ball milling was first described in material synthesis by Benjamin and his co-workers in the late 1960's. Since then, the method has expanded to numerous fields.[111] Recently, ball milling was applied to supramolecular chemistry and gained extraordinary success in mechanosynthesis and self-assembly.[112–114] Given the ball milling synthesis is solvent-free, or at least requires very little co-solvent in the synthesis, the issues associated with solvents are avoided (*e.g.*, poor solubility of metal salts and/or organic linkers, and the production of a large amount of waste).[115] The first MOF synthesized *via* mechanosynthesis was reported in 2006. James and co-workers

formed a robust 3-dimensional porous Cu-based MOF without any heating.[116] As an unconventional synthesis method, mechanosynthesis not only offers the possibility of making new MOFs, but also provides access to a new perspective in green chemistry.[117–123]

III. Microwave Assisted MOF Synthesis

One challenge associated with MOF synthesis is that many MOFs required a considerable amount of time to form at elevated temperatures. For example, MOF-808 requires 7 days of heating at 100 °C.[124,125] With the focus on crossing the academia-industry barrier, it is important to reduce the heating time but maintain the yield, topology, and properties of the MOF. One of the many methods that has been discovered to address this is microwave assisted synthesis. By tuning irradiation power and reaction time, the increased kinetic energy of the microwave will increase molecule collisions, and thus increase the rate of MOF formation.[126] The use of microwave assisted MOF synthesis such as in UiO-66, MIL-101-NH_2, and lanthanide-based MOFs have been documented.[127–129]

1.2.1.3 Green Solvent Cyrene Used in MOF Synthesis

Unconventional synthetic methods for MOF synthesis are, at times, centered around the idea of making MOFs with environmentally benign solvents instead of using conventional DMF or DEF. Unfortunately, these solvents can cause damage to the environment as well as mankind. To that end, it is crucial that chemists and chemical engineers consider the societal expectation that the design and applications of new technology be centered on greener and sustainable chemical processes in the first place.[130,131]

Given the versatility of MOFs towards applications in environmental remediation, and human protection, the environmental friendliness of the materials should be considered from cradle to grave and not just the environmental impact that the application holds. In other words, I believe that MOF synthesis should also be cognisant of the environment, human health risks, and, ultimately, green chemistry. If MOFs are going to be used in applications for toxic gas removal (*i.e.*, sulfur dioxide sequestration in Chapter 3), then it is important that they are not producing unnecessary waste at the synthetic step of MOF production (Chapter 2). To that end, the art of MOF synthesis not only depends on the design of organic linkers and metal nodes, but also on the influence of solvents on the acid-base chemistry as well as the necessity to either prevent pore collapse, or form a high density (*i.e.*, non-porous) material.

With that in mind, Chapter 2 of the thesis explores the synthesis of MOFs with the goal of finding an alternative solvent of forming MOFs. As mentioned above, the majority of MOFs are synthesized from either DMF or DEF.[132] The high boiling point, good solubility of metal salts and organic ligands, and beneficial acid-base chemistry make these organic solvents superior to others.[133] However, the problems brought by the chemicals used and the by-products produced in the synthetic process served as a wake-up call since it has been documented that these kinds of organic chemicals (*e.g.*, DMF and DEF) exhibit reprotoxicity and end-of-life issues. Furthermore, incineration of these solvents can produce NO_x, an environmental pollutant.[134–138]

Furthermore, legislative restrictions also narrow down the application of these undesirable solvents.[139] Based on this, Chapter 2 of this thesis aimed to design a greener method by which MOF can be formed with an alternative solvent to replace DMF.

Ultimately, water would be the ideal solvent for MOF synthesis as it is abundant

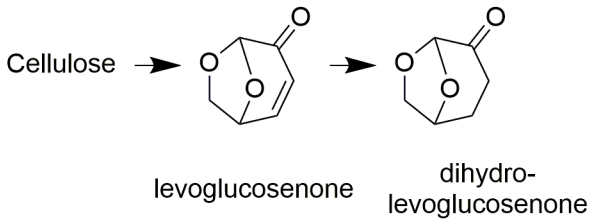

Figure 1.10: Scheme of the Production of Cyrene.

Table 1.1: Physical Properties of DMF and Cyrene.[a]

	DMF	Cyrene
δ_D/MPa$^{0.5}$	17.4	18.8
δ_P/MPa$^{0.5}$	13.7	10.6
δ_H/MPa$^{0.5}$	11.3	6.9
MP/°C	-60.5	-18.0
BP/°C	153	203
ρ/g cm^{-3}	0.94	1.25
V_m/cm^{3}mol^{-1}	77.0	102.5

[a] Calculated with HSPiP software. δ_D, δ_P, and δ_H represent the dispersion, polar and hydrogen bonding interaction parameters, respectively.

and yields zero threat to the environment. However, due to the limited solubility of organic linkers in water, the limited temperature range available for water (assuming no high-pressure equipment is used), there is a need to find alternative green sol-

vents which can be used to form MOFs. One such solvent is dihydrolevoglucosenone (Cyrene®) (Figure 1.10).[140] As an environmentally benign solvent, Cyrene has several advantages in MOF synthesis. Firstly, it is derived from waste biomass cellulose by two simple steps *via* dehydration of cellulose to levoglucosenone and subsequently hydrogenated to dihydrolevoglucosenone, as shown in Figure 1.10. Secondly, Cyrene has similar physical and chemical properties to DMF (Table 1.1). With these in mind, we proposed that Cyrene would be a good replacement of DMF or DEF in MOF synthesis (Chapter 2).

1.2.2 Toxic Chemical Adsorption

Fossil fuels, especially petroleum, natural gas, and coal, are, and may likely remain, the main energy sources for decades.[141] The waste gases that are released when fossil fuels undergo combustion present numerous environmental challenges with regards to air pollution (*e.g.*, acid rain and smog), global warming, water pollution, soil contamination, and radioactive contamination.[141–143] Most of these waste products are called TICs. TICs are industrial chemicals that are manufactured, stored, transported, and used throughout the world and they can be in the gas, liquid, or solid state.[144] TICs can be chemical hazards (*e.g.*, carcinogens, reproductive hazards, corrosives, or agents that affect the lungs or blood) or physical hazards (*e.g.*, flammable, combustible, or explosive, or otherwise reactive).

Sulfur dioxide is a by-product of fossil fuel burning. Under humid environments, sulfur dioxide rapidly reacts with water (*e.g.*, in the atmosphere or lungs) to form sulfuric acid. As such, together with ammonia, chlorine, and hydrogen sulfide, sulfur

dioxide is considered to be a TIC.[144] Unlike nerve agents,[145] TICs are often used in chemical warfare due to the ease in which they can be obtained for commercial applications. For example, sulfur dioxide is primarily used for production of sulfuric acid, as an oxidizing agent to reduce hydrogen sulfide to elemental sulfur, and even as a fruit preservative.[146] Considering the risks of sulfur dioxide to individuals, society (*e.g.*, destruction of architectures due to acid rain), and the environment, it is critical to find methods of reducing anthropogenic sulfur dioxide as well as developing methods to protect individuals from weaponized sulfur dioxide.[147]

As such, Chapter 3 of this thesis focuses on investigating the role that MOFs can play in the sequestration of sulfur dioxide. More specifically, we are investigating the role that chemisorption reactions (see Chapter 3) can play on tuning the adsorption/desorption of sulfur dioxide from a porous structure. The experiments were carried out by microporous breakthrough analysis with the help of our collaborator at the Edgewood Chemical Biological Center.

Chapter 2

The Use of an Alternative Solvent in the Synthesis of MOFs[†]

2.1 Introduction

With the introduction of the Registration, Evaluation and Authorisation of Chemicals (REACH) legislation in the European Union, there is a growing trend towards safer production and use of chemicals by industries.[139] Future legislative restrictions under REACH are likely for several traditional dipolar aprotic solvents including DMF, *N,N*-dimethylacetamide (DMAc), and *N*-methylpyrrolidinone (NMP) which have now found their way onto a list of "substances of very high concern" (SVHC).[148] With the

[†]Part of the work in this chapter is reproduced here with permission from Zhang, Jinfeng; White, Gabrielle B; Ryan, Michaela D; Hunt, Andrew J; and Katz, Michael J, Dihydrolevoglucosenone (Cyrene) as a green alternative to *N,N*-dimethylformamide (DMF) in MOF synthesis. ACS Sustainable Chemistry & Engineering 2016, 4 (12), 7186–7192. Copyright 2016 American Chemistry Society.

increased use of MOFs, it is of vital importance to find safer and preferably bio-derived solvents that can substitute these traditional dipolar aprotic solvents used in their manufacture.

Cyrene[140] is a dipolar aprotic solvent which can be derived from waste cellulose in two simple steps (Figure 1.10).[149] The Kamlet–Abboud–Taft (KAT) polarity scale π^*, corresponding to the dipolarity of a solvent molecule, is similar between Cyrene and DMF, with values of 0.93 and 0.88, respectively.[140] Hansen solubility parameters relating to dispersion (δ_D), polar (δ_P) and hydrogen bonding (δ_H) interactions, indicate that Cyrene is a close solvent match to DMF (Table 1.1).[149] Importantly, Cyrene demonstrates no mutagenicity (OECD No. 471 and 487), LD_{50}>2000 mg/kg (OECD No. 423, acute toxicity method) and is barely ecotoxic (OECD No. 201, 202 and 209).[††] Cyrene has been observed to have no mutagenicity. It is barely ecotoxic and has exhibits similar solubility and physical parameters to DMF. With that in mind, Cyrene, a bio-derived solvent, was investigated in the synthesis of archetypal MOFs with the hope of deriving a synthetic strategy by which new MOFs can be made with Cyrene.

[††]a) Data kindly provided by Circa Group Ltd., the manufacturer of Cyrene, by F. Hoffmann La Roche Ltd., hereby acknowledged as the source of the data and corresponding study; b) Safety Data Sheet of F.Hoffmann-La Roche Ltd.

2.2 Results and Discussion

2.2.1 Synthesis of HKUST-1

The initial investigation focused on the use of Cyrene in the synthesis of the paddlewheel MOF, HKUST-1 (Figure 1.6), due to its varied applications coupled with its availability through chemical retailers such as Sigma-Aldrich.[150–154] HKUST-1 is a MOF formed with copper(II) paddlewheel nodes (Figure 1.6) and 1,3,5-benzenetricarboxylate linkers. As a direct comparison to the published DMF synthesis,[155] HKUST-1 was initially synthesized from a solution of Cyrene/EtOH/H_2O (Table 2.1).

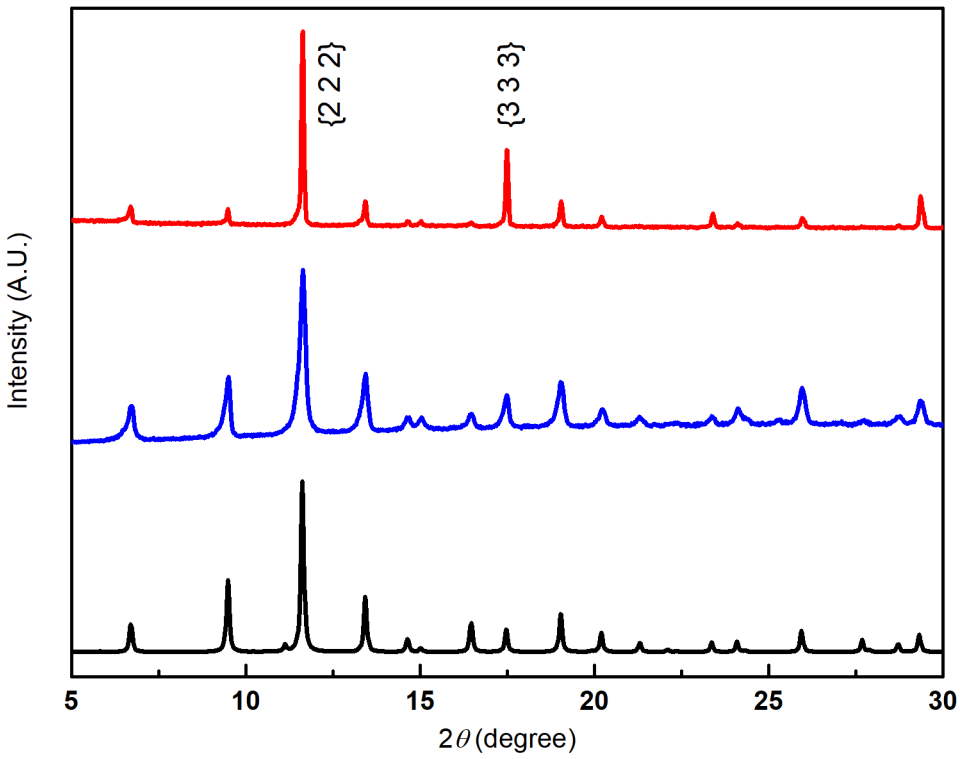

Figure 2.1: Simulated (Black) and Observed, As-Synthesized Using DMF (Blue) or Cyrene (Red), PXRD of HKUST-1.

Figure 2.1 shows the powder X-ray diffractogram (PXRD) of HKUST-1 made from both DMF and Cyrene (1:1:1 volume ratio of Cyrene/95 % EtOH/water). As can be seen, the peak positions between the simulated and observed PXRDs match the simulated diffractogram thereby indicating that the Cyrene-based synthesis is able to produce HKUST-1. Perhaps more interesting are the intensities and line widths. In the Cyrene-derived HKUST-1, the two most intense reflections are the {2 2 2} and {3 3 3} reflections indicating a high degree of preferred orientation along the {1 1 1} direction in comparison with DMF-synthesized HKUST-1. Furthermore, the peak widths of Cyrene-derived HKUST-1 are narrower indicating a larger average particle size in Cyrene-derived *vs.* DMF-derived HKUST-1.

Table 2.1: Synthesis Details of the Various Attempts Used to Make HKUST-1.[b]

		DMF (mL)	Cyrene (mL)	Ethanol (mL), purity	Deionized water (mL)	Observed BET SAs (m^2/g)
HKUST-1-DMF		2.0	…	2.0, 95 %	2.0	1400
HKUST-1-Cyrene	Trial 1	…	2.0	2.0, 95 %	2.0	1100
	Trial 2	…	2.0	2.0, 95 %	…	950
	Trial 3	…	2.0	0.2, 100 %	…	600
	Trial 4	…	2.0	0.4, 100 %	…	1400
	Trial 5	…	2.0	2.0, 100 %	…	1500

[b] All synthesis were carried out with 43.0 mg of $Co(NO_3)_2 \cdot 3H_2O$ and 25.0 mg of H_3BTC.

With the structural elucidation confirmed, we examined the nitrogen gas adsorption isotherms (77 K) of HKUST-1. As shown in Figure 2.2 and Table 2.1, when HKUST-1 was synthesized from DMF, a Brunauer–Emmett–Teller (BET) surface area (SA) of 1400 m^2/g was observed (blue colour trace Figure 2.2). With Cyrene under the identical conditions (Trial 1, Table 2.1), however, despite the promising PXRD observed in Figure 2.1, the BET surface area of HKUST-1 was observed to be a mere 600 m^2/g (white colour trace Figure 2.2).

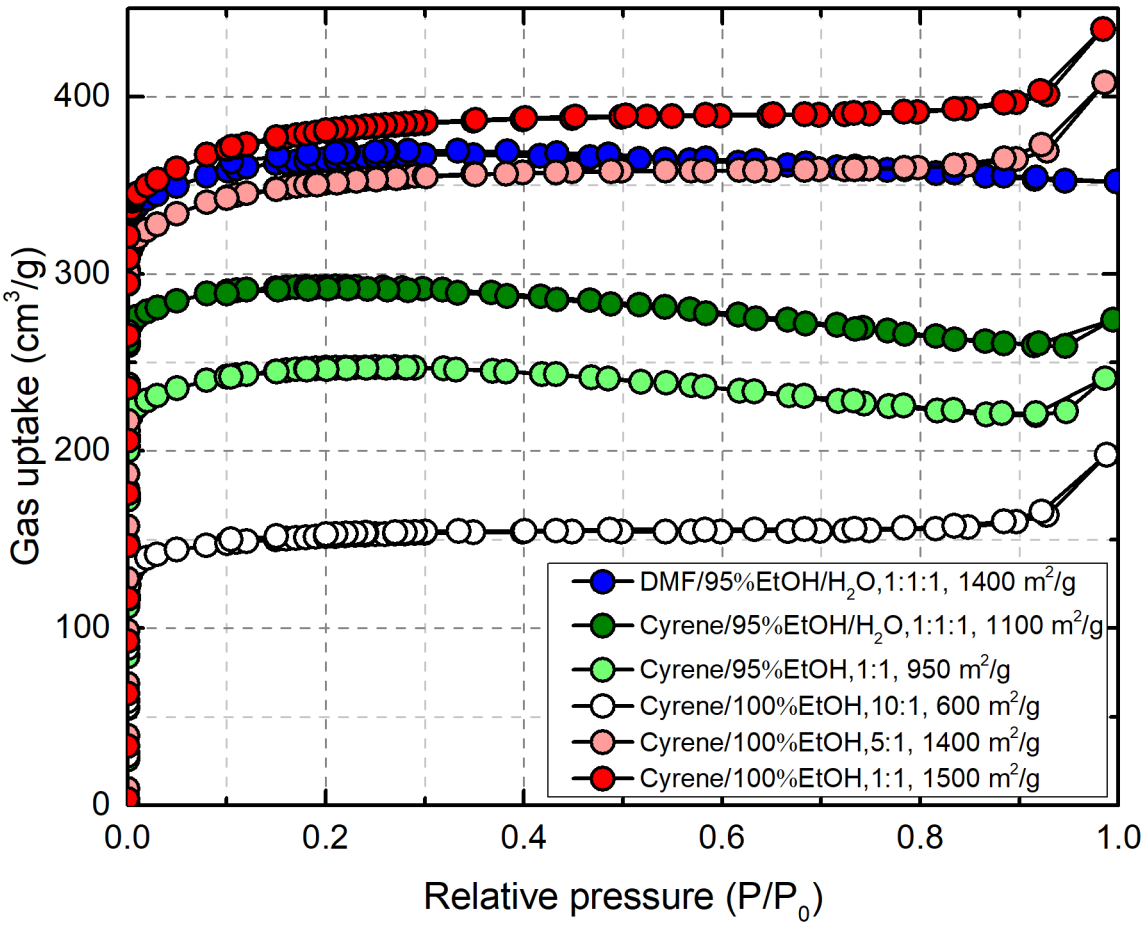

Figure 2.2: Nitrogen Gas Adsorption Isotherms of HKUST-1 Measured at 77 K Using Different Solvent Mixtures.

In order to determine the origin of the surface area drop between DMF and Cyrene, we investigated the role of ethanol as an additive. As shown in Figure 2.2 and Table 2.1, when nominally dry EtOH is used in a 5:1 ratio with Cyrene, then a surface area of 1400 m^2/g is observed (Trial 4, Table 2.1). However, when 95 % EtOH is used, then lower than ideal BET surface areas are observed. It is hypothesized that this behaviour is due to the formation of a geminal diol of Cyrene and potentially other products (*vide infra*) in the presence of water.[156] Therefore, control of the water/Cyrene ratio is necessary to optimize BET surface areas.

Table 2.2: Yield of HKUST-1 Made with Different Solvents.[c]

Solvents	Yield (%)
DMF/EtOH/H_2O	35
Cyrene/EtOH	33
DMSO/EtOH	0
H_2O	6.5
EtOH	20
EtOH/H_2O	3.0

[c] Yields are based on moles of Cu.

Given that synthesis of HKUST-1 can be performed in alternative solvents such as EtOH,[153,157] the importance of Cyrene in this synthesis was investigated. In both DMF and Cyrene, we observed a 35 % yield (Table 2.2). However, when DMSO/EtOH was substituted for Cyrene/EtOH, then no HKUST-1 was formed. Similarly, when

EtOH or an EtOH/H_2O mixture was used in the absence of Cyrene, a *ca.* 5 % yield was observed. These results indicate that Cyrene's role is crucial in MOF formation.

2.2.2 Synthesis of Other MOFs

With these results in mind, the use of Cyrene as a solvent was extended to other MOFs. In order to adequately survey the field, we choose four additional archetyped MOFs, UiO-66 (Figure 1.8), ZIF-8 (Figure 1.4), MOF-74 (Figure 1.7), and Zn_2(1,4-benzenedicarboxylate)$_2$(1,4-diazabicyclo[2.2.2]octane) [$Zn_2(BDC)_2(DABCO)$] (Figure 2.3), as representatives.

The aforementioned MOFs were chosen because they represent various families of MOFs that are currently being investigated for various applications in the literature citations. Zr MOFs are very popular due to their outstanding stability and wide applications.[29] UiO-66 was chosen because it is the prototypical Zr-containing MOF (Figure 1.8). This MOF contains a $[Zr_6O_4(OH)_4]^{12+}$ cluster node that is connected to 12 additional cluster nodes *via* BDC linkers. The advantage of UiO-66 is that BDC can be easily substituted for other linkers (*e.g.*, NH_2-BDC, NO_2-BDC, and NDC). Given the ease in which these derivatives of UiO-66 are formed, coupled with the stability of these MOFs, it is perhaps unsurprising that these materials are featured in several applications.[29,158,159]

Another class of MOFs widely examined is the family of zeolitic imidazolate frameworks known as ZIFs. In ZIFs, imidazolate linkers connect tetrahedral dications such as Zn(II) and Cd(II). Given the *ca.* 120° angle between the imidazole nitrogen lone pairs, the structures of these materials resemble those of zeolites. By judicious choice

of the imidazole, or combination of imidazoles, various ZIFs can be made *via* conventional methods.[28]

M-MOF-74 (M=Zn, Co, Fe, Mg, Mn, Ni) represents a series of MOFs, which are often featured in novel studies due to the ease in which an open-coordination site on the metal can be generated and modified.[160–162] The linker used here, DOT, contains two OH and two COOH groups, which are all deprotonated and coordinated to the node in the MOF. The large pore aperture inside MOF-74 (Figure 1.7) offers the possibility of large molecules to easily pass through.

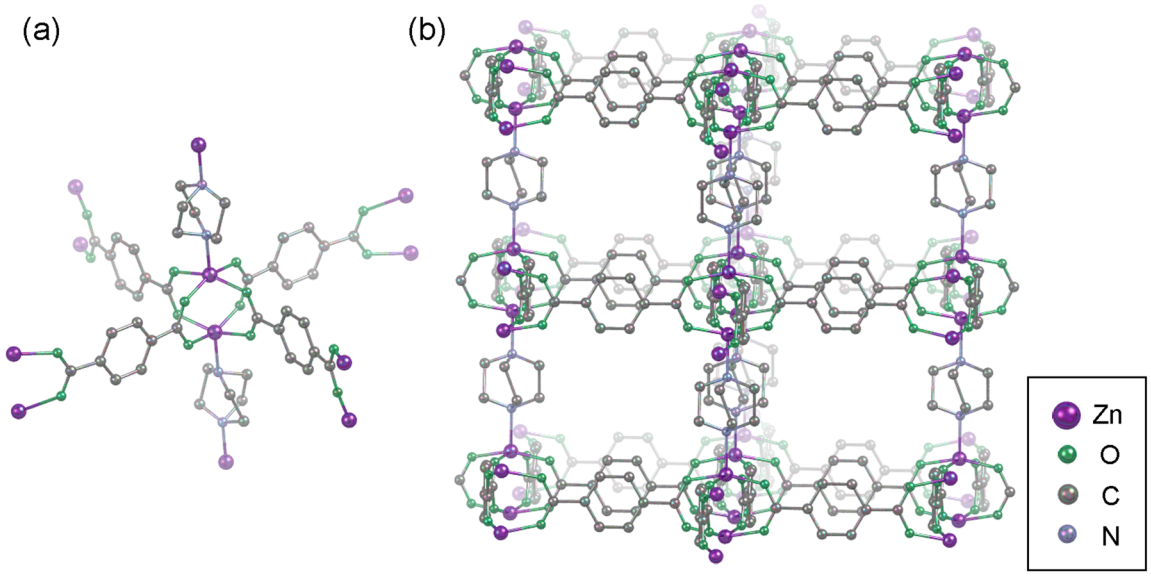

Figure 2.3: (a) Representative Fragment Structure of $Zn_2(BDC)_2(DABCO)$ Showing How Zn(II) Cation Nodes Coordinate with BDC and DABCO Linkers. (b) 3-Dimensional Pore Structure of $Zn_2(BDC)_2(DABCO)$.

The last MOF which was chosen, $Zn_2(BDC)_2(DABCO)$, uses a combination of two different linkers, BDC and DABCO. These pillared (DABCO) paddlewheel (BDC)

MOFs (Figure 2.3), have been studied for application in catalysis using SALEN-based pillars.[163,164]

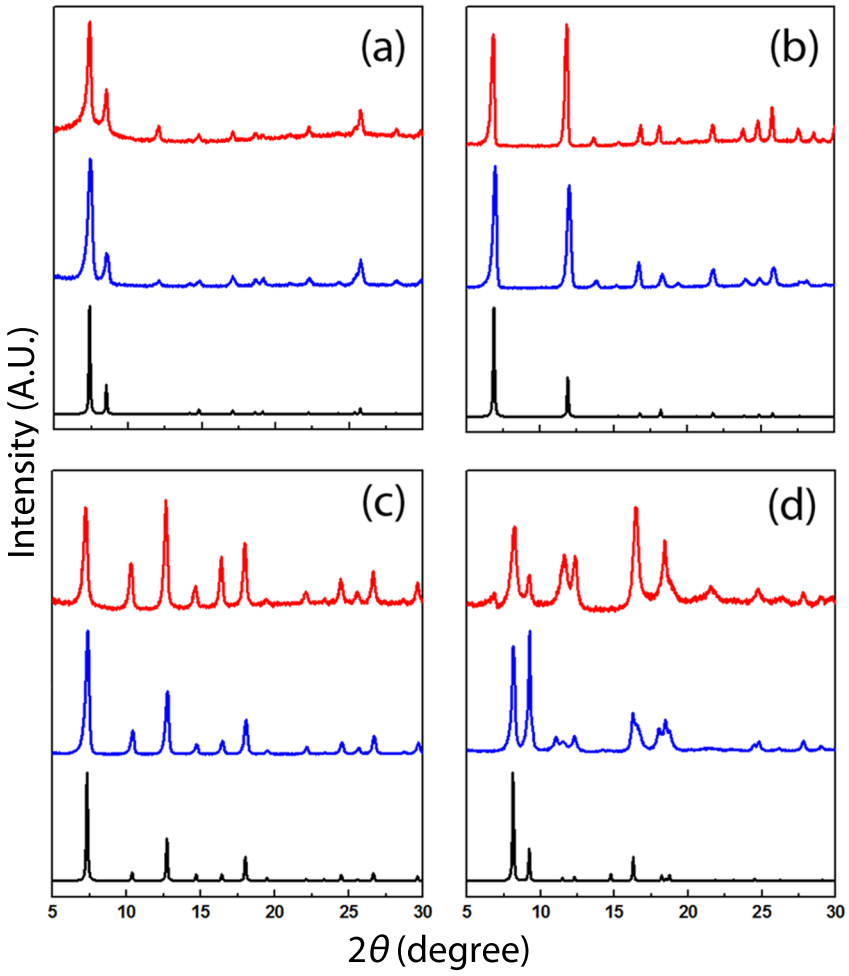

Figure 2.4: The PXRD Patterns of (a) UiO-66, (b) Co-MOF-74, (c) ZIF-8, and (d) $Zn_2(BDC)_2(DABCO)$. The Simulated Spectrum Are Observed in Black and the Measured Spectrum in DMF and Cyrene Are Observed in Blue and Red Respectively.

As shown in Figure 2.4, except for $Zn_2(BDC)_2(DABCO)$, the peak positions of the PXRDs between the DMF- and Cyrene-derived MOFs match the simulated PXRD.

These results indicate that the desired MOFs were formed. The differences in intensities are due to a combination of preferred orientation and differences from the presence of pore-bound solvents, which are not predicted from the simulated PXRD.[165] For $Zn_2(BDC)_2(DABCO)$, the flexibility of the MOF, due to the inclusion of various solvents, is evident by the multitude of $Zn_2(BDC)_2(DABCO)$ structures in the Cambridge-Crystallographic Data Center (CCDC), the peak positions do not match as well in comparison to the other MOFs.[165] Figure 2.5 readily illustrates this point. The guest free MOF crystallizes at room temperature with a tetragonal space group of *P 4/m m m*. However, when crystallizes with DMF in the pore, a different body centered tetragonal cell *I 4/m c m* is formed. There are many more such examples that change the bend angle in the BDC (Figure 2.5), or even the tilt angle between neighbouring sheets.[166]

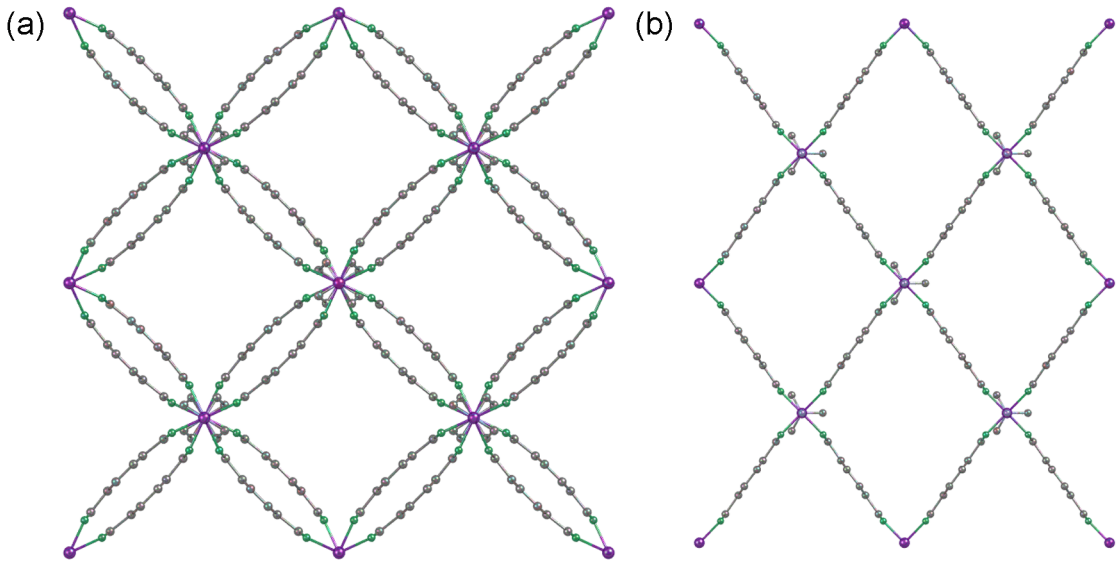

Figure 2.5: Schematic Structure of (a) Bent Linkers and (b) Linear Linkers of $Zn_2(BDC)_2(DABCO)$ Viewed Down the C-Axis.

To further examine $Zn_2(BDC)_2(DABCO)$, we disassembled both DMF- and Cyrene-derived $Zn_2(BDC)_2(DABCO)$ in D_2SO_4/DMSO-d_6 in order to examine the BDC/DABCO ratio. Given the ratio of 4 protons in BDC to 12 protons in DABCO, 8:12 ratio of BDC:DABCO protons is expected based on the formula of $Zn_2(BDC)_2(DABCO)$ and 8:12 ratios of BDC:DABCO protons for both Cyrene and DMF-derived $Zn_2(BDC)_2(DABCO)$ are shown in Figure 2.6.

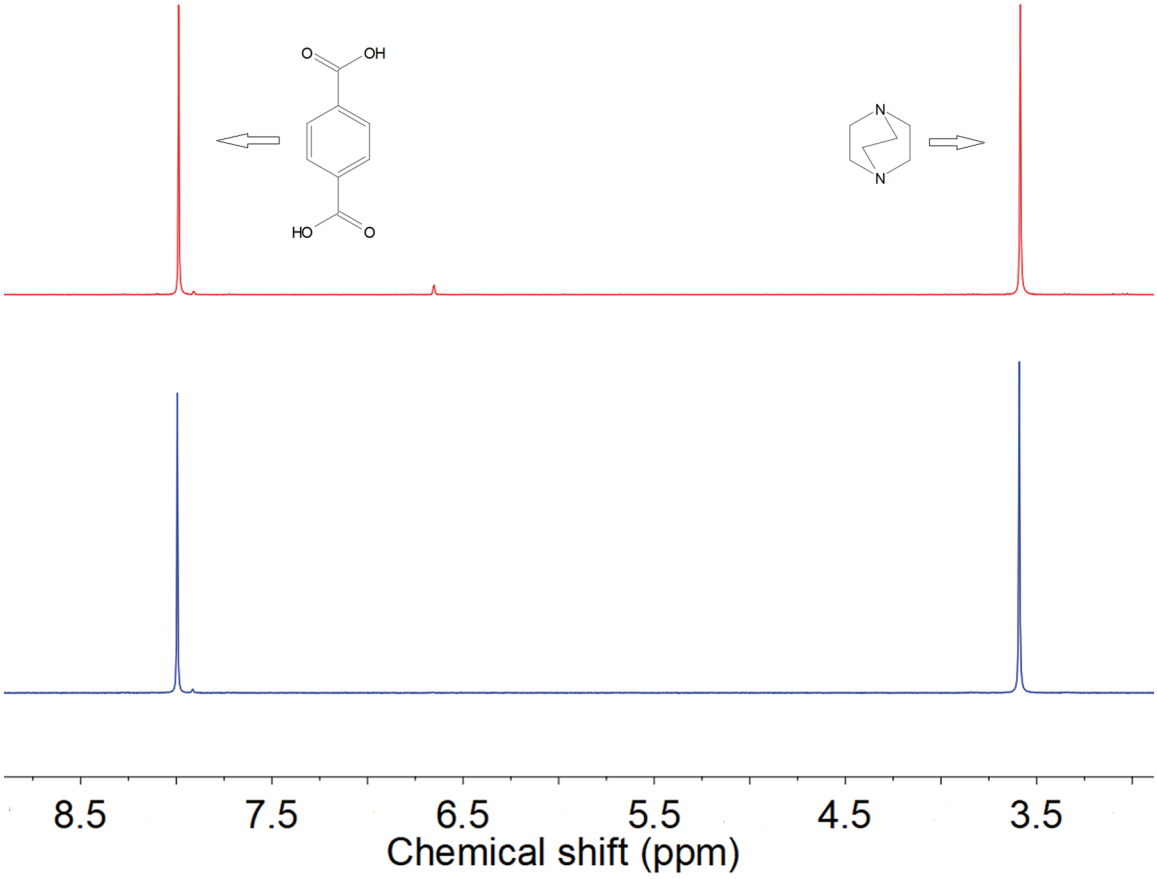

Figure 2.6: ^{1}H NMR Spectrum of $Zn_2(BDC)_2(DABCO)$, Cyrene (Red) *vs.* DMF (Blue), Digested in D_2SO_4/DMSO-d_6.

These results indicate that $Zn_2(BDC)_2(DABCO)$ has been successfully made in both DMF and Cyrene. All four MOFs match the expected PXRD thereby demonstrating the utility of Cyrene toward the synthesis of MOFs. Unfortunately, as shown in Figure 2.7 and Table 2.3, the Cyrene MOFs show lower-than ideal surface areas in comparison to their DMF counterparts.

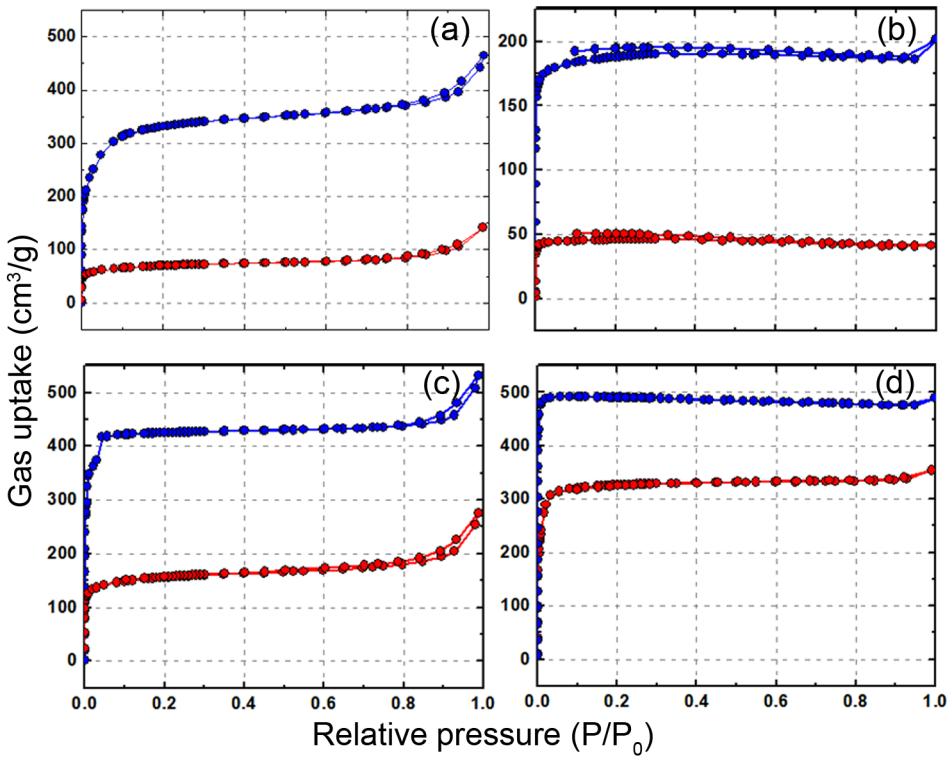

Figure 2.7: Nitrogen Gas Adsorption Isotherms of (a) UiO-66, (b) Co-MOF-74, (c) ZIF-8, and (d) $Zn_2(BDC)_2(DABCO)$ Synthesized Using DMF (Blue) or Cyrene (Red).

Table 2.3: Summary of BET Surface Areas.

MOFs	Expected BET SAs (m^2/g)	Observed BET SAs (m^2/g)	
		DMF-derived MOFs	Cyrene-derived MOFs
HKUST-1	1740[167]	1400	1500
UiO-66	1700[168]	1300	500
Co-MOF-74	1572[169]	800	200
ZIF-8	1950[28]	1700	600
$Zn_2(BDC)_2(DABCO)$	1750[170]	1950	1300

2.2.3 Investigation into the Low SAs of Cyrene-Derived MOFs

Given the importance of finding greener methods of forming MOFs, we wanted to investigate the origin of the lower surface areas, rather than simply optimize the system, to better understand the chemistry of Cyrene. To that end, we looked more closely at ZIF-8; similar results were observed for MOF-74 and $Zn_2(BDC)_2(DABCO)$. From the PXRD of all five MOFs (Figure 2.1, Figure 1.4), there is a general agreement between the simulated and observed diffractograms. However, over the course of this project, there were times when peaks that were inconsistent with the MOF simulations were observed.

As shown in Figure 2.8, compared with its DMF counterpart and the simulated PXRD, the PXRD of ZIF-8 often showed different peak intensities which could not be rationalized from preferred orientation and were not usually observed for pore-filled

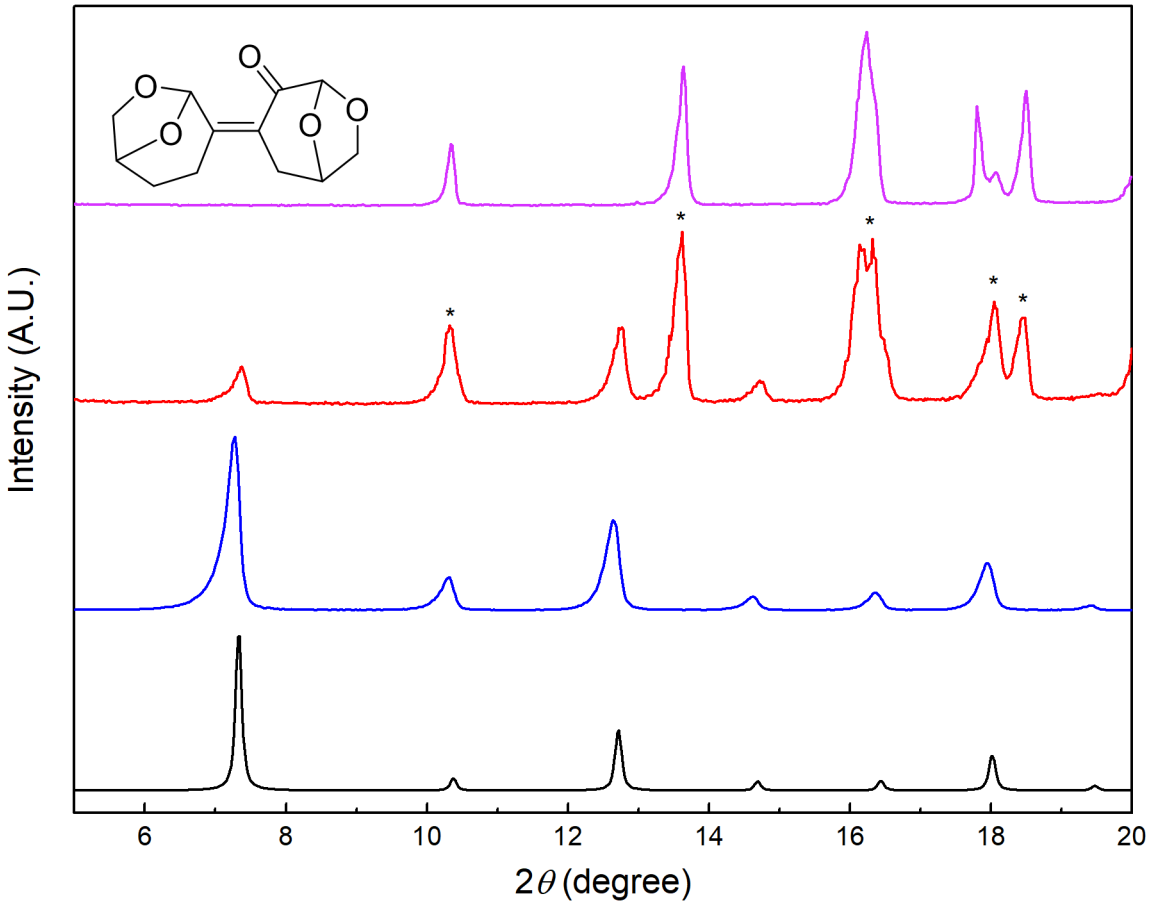

Figure 2.8: Simulated (Black) and Observed, As-Synthesized Using DMF (Blue) or Cyrene (Red), PXRD of ZIF-8. The Observed PXRD of the Cyrene Aldol-condensation Product Is Shown in Pink. Peaks Marked with ∗ Indicate the Presence of the Cyrene Aldol-Condensation Product Intermixed with ZIF-8.

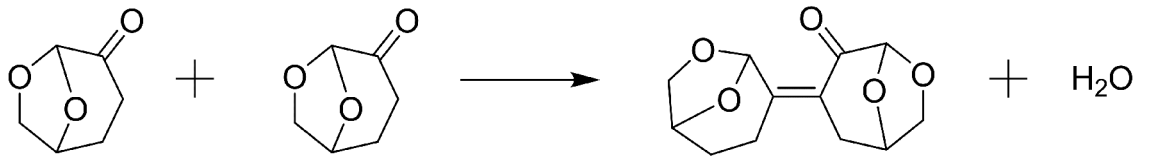

Figure 2.9: Scheme of the Production of the Cyrene Aldol-Condensation.

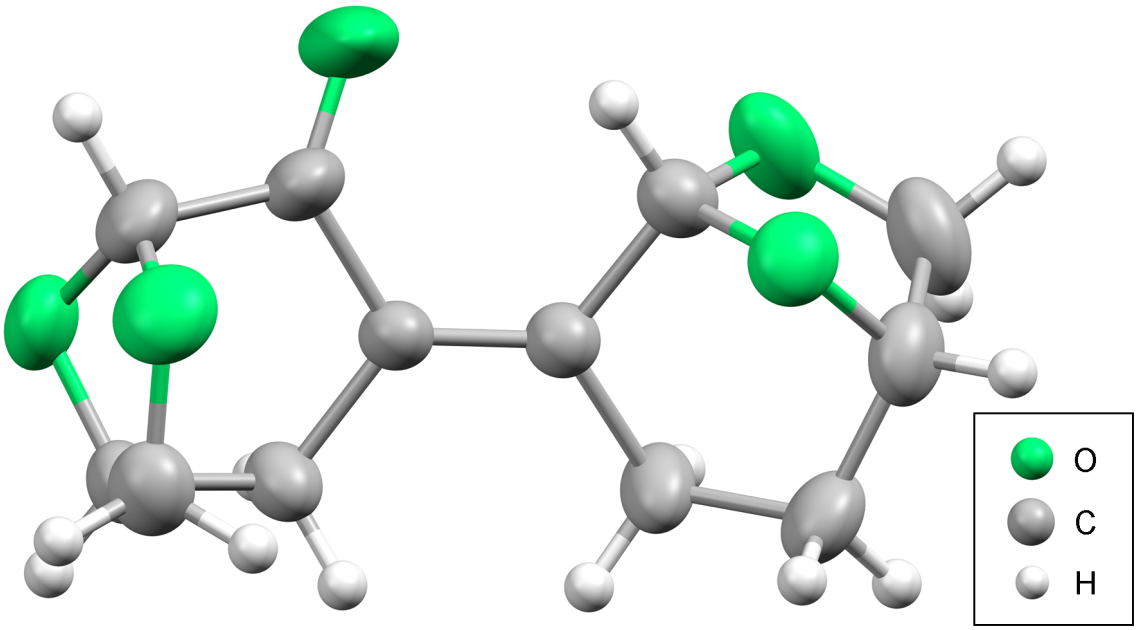

Figure 2.10: Crystal Structure Showing the Cyrene Aldol-Condensation Product.

ZIF-8. Additionally, new peaks inconsistent with any miller index of ZIF-8 were also observed. Fortunately, examination of ZIF-8 under a microscope revealed that a white crystalline material, inconsistent with the morphology of ZIF-8, was observed among the microcrystalline powder of ZIF-8 (Figure 2.8). Single-crystal X-ray analysis of these crystals indicate that, in the presence of the ZIF-8 starting materials, a double terminated, thin cuboid crystal of the aldol-condensation product of Cyrene was formed (Figure 2.9). The existence of this crystal adds a non-porous material to the batch of ZIF-8 thus decreasing the surface areas calculated by experimental data. Single crystals of the aldol-condensation product were extracted from a batch of ZIF-8 using CH_2Cl_2 and recrystallized from hot CH_2Cl_2 yielding large single crystals suitable for X-ray diffraction. The crystallographic data can be seen in Table 2.4 and the structure is shown in Figure 2.10.

Table 2.4: Crystallographic Data and Structure Refinement for the Product of the Aldol-Condensation.

Empirical formula	$C_{14}H_{15}O_5$	Formula weight (g/mole)	263.26
Temperature (K)	300	Radiation	MoKα (λ=0.71073)
Crystal system	monoclinic	Space group	P 2_1
a (Å)	6.53804(18)	α (°)	90
b (Å)	9.9588(3)	β (°)	96.590(3)
c (Å)	8.6752(2)	γ (°)	90
Volume (Å^3)	561.12(3)	Z	2
ρ_{calc} (g/cm^3)	1.558	μ (mm^{-1})	0.119
Goodness-of-fit on F^2	1.112	2θ range for data collection °	4.726 to 58.888
Index ranges	-8≤ h≤ 8	Reflections collected	7744
	-13≤ k≤ 13	Independent reflections	2752 [R_{int} = 0.0124]
	-11≤ l≤ 12	Data/restraints/parameters	2752/1/155
Flack parameter	-0.1(2)	Largest diff. peak/hole (e/Å^3)	0.25/-0.28
Final R indexes [I≥2σ(I)]	R_1 = 0.0400, wR_2 = 0.1138	Final R indexes [all data]	R_1 = 0.0411, wR_2 = 0.1155

The crystals of the aldol-condensation product can be washed out as shown in Figure 2.8. However, this does not necessary remove the pore-bound material. The pore-bound solvent inside the MOFs is thus believed to be one reason for the less than ideal surface areas of these MOFs. So, in order to see if the aldol condensation product is responsible for the lower SAs, we digested the MOF to check the pores. As shown in Figure 2.11, a detectable amount of Cyrene from the pores was observed in the D_2SO_4/DMSO-d_6 digested ZIF-8 even after several washings. However, the aldol-condensation product was not detected here by ^{1}H NMR. The data suggests that the aldol-condensation product is not trapped in pores, but simply co-crystallizes with the MOFs. Further study found that the aldol-condensation product was soluble in DMF, DCM and acetonitrile making it easy to wash away using our standard synthetic procedure. After several washings, the aldol-condensation product was washed away while Cyrene was still present. This suggests that the Cyrene is likely trapped in pores either due to a favorable interaction within the pore, or a ship-in-a-bottle situation in which the MOF grew around the solvent but the pore aperture is now too small to allow the solvent out.

Figure 2.12 indicates that the Cyrene and aldol-condensation product have different proton environments. In order to confirm that only the aldol-condensation product was formed, and not multiple products, we investigated the NMR spectra of the DCM-extracted materials post MOF synthesis. Herein with the utility of 2-dimensional NMR measurements, we successfully determined that only the aldol-condensation product was formed. Figure 2.13, HSQC (HSQC=heteronuclear single quantum correlation) provides correlation between the aliphatic carbon and its directly attached protons while Figure 2.14, COSY (COSY=correlation spectroscopy)

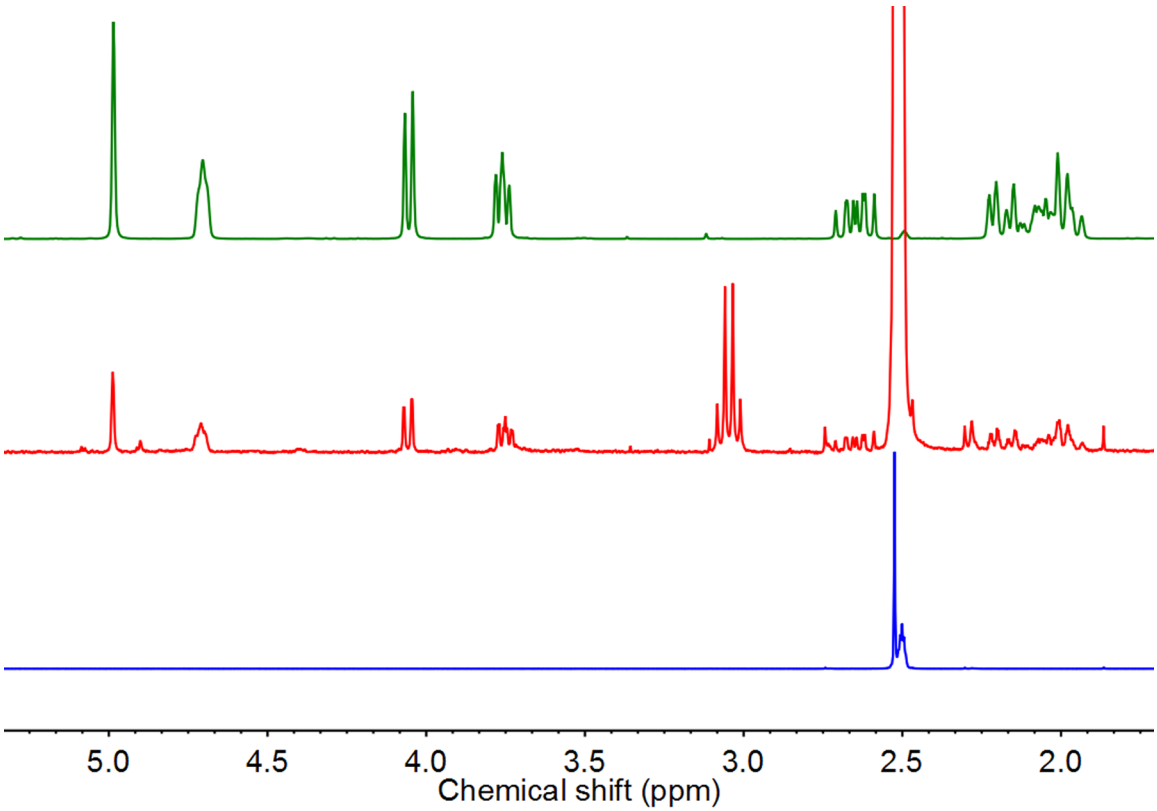

Figure 2.11: ^{1}H NMR of DMF-Derived ZIF-8 (Blue); Cyrene-Derived ZIF-8 (Red), and Cyrene (Green). MOFs Are Digested by Acid (D_2SO_4/DMSO-d_6).

spectrum shows how neighboring protons couple to each other. Combining these three results as well as the PXRD spectrum, the aldol-condensation crystal structure was confirmed.

Figure 2.12 illustrates that there are fourteen protons present when the MeOH peak at 3.47 ppm is ignored. This is consistent with the crystal structure of the aldol-condensation product. When we turned our attention to Figure 2.13, the HSQC NMR result provides more information on this product. It is clear that six -CH_2 (blue regions) and four -CH (red regions) regions exist; this is once again consistent with the crystal structure. Some protons belong to the same carbon atom. For example,

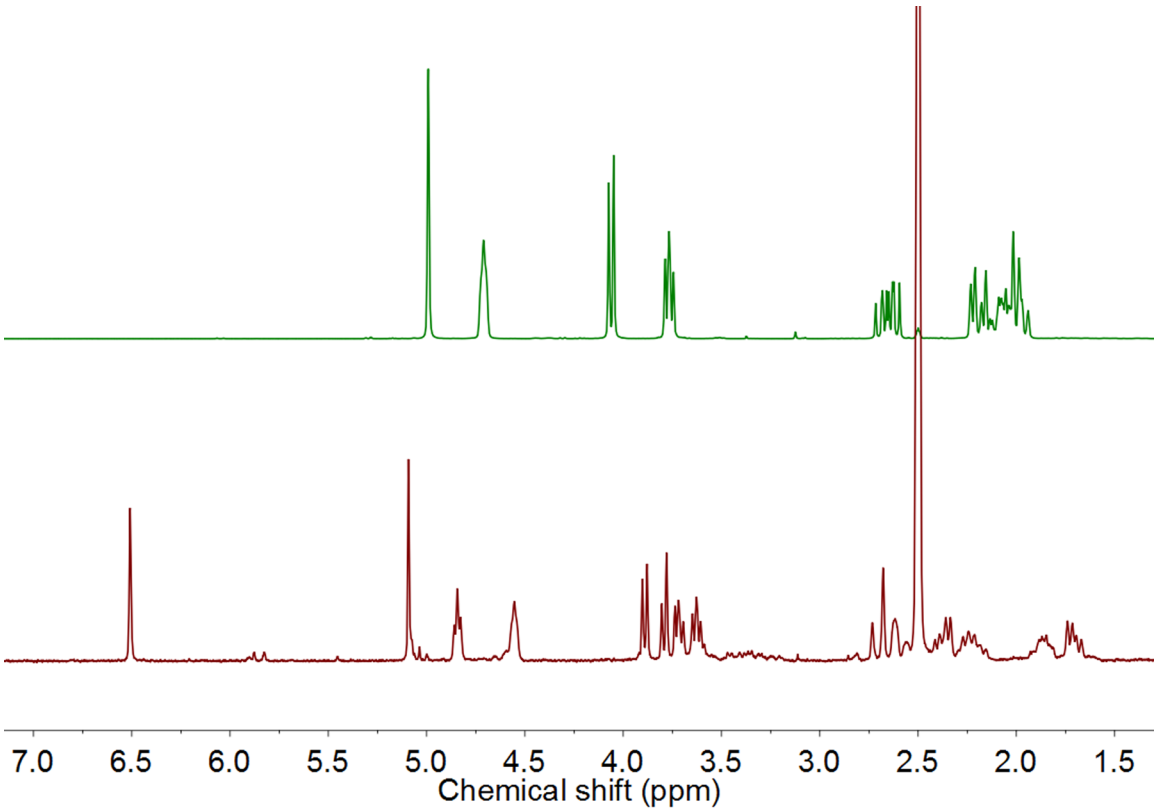

Figure 2.12: ^{1}H NMR of Cyrene (Green) and the Cyrene Aldol-Condensation Product (Maroon) Digested in D_2SO_4/DMSO-d_6.

the protons at 1.75 and 2.17 ppm, and protons at 2.55 and 2.80 ppm belong to the same carbon atom. While the protons at 4.60 and 4.80 ppm would appear to belong to the same carbon atom, the phase of the carbon atom indicates that the carbon atom must be a CH or a CH_3. As there are no CH_3 in the molecule, we propose that there are two separate CH protons that have chemically equivalent, or nearly equivalent carbon atoms. Additionally, there are two protons which belong to one carbon at 2.37 ppm also shown in this figure. The four protons at 3.90 ppm have very similar environments which makes them very hard to separate, but it is most likely due to two sets of CH_2 fragments.

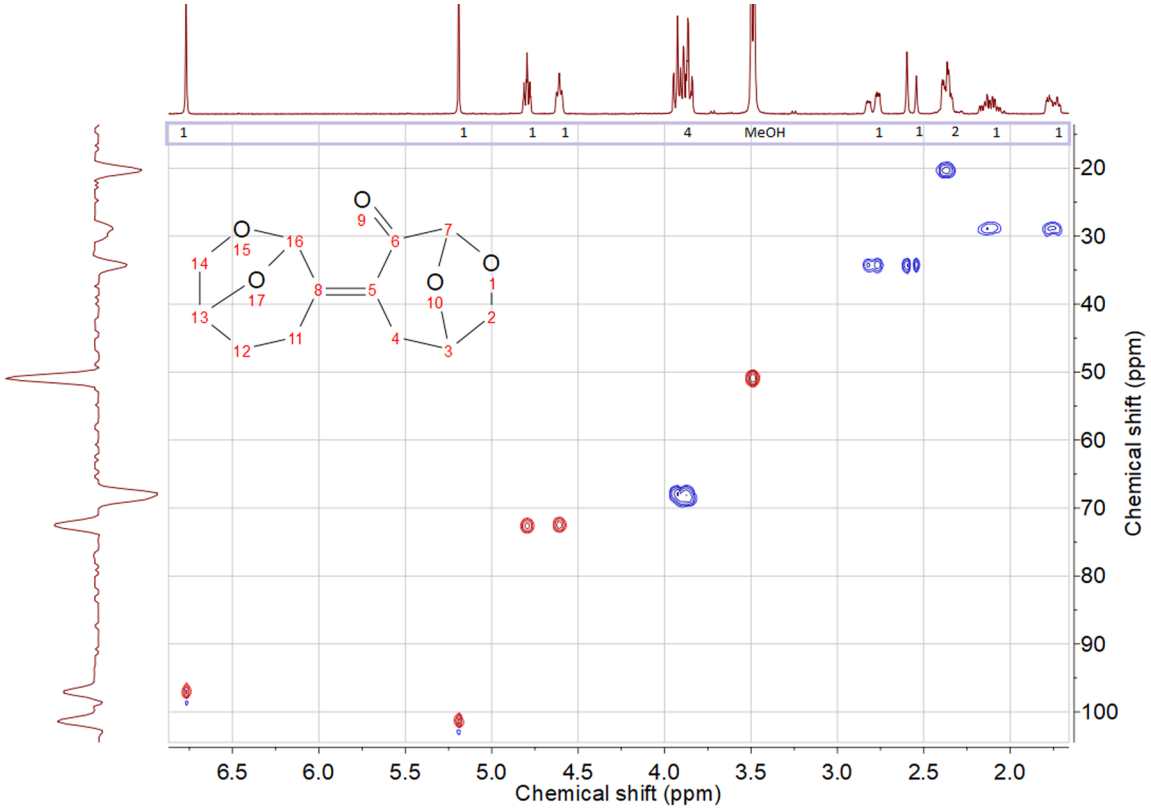

Figure 2.13: HSQC Spectrum of the Cyrene Aldol-Condensation Product (Maroon) Dissolved in $CDCl_3$, Blue (CH_2), Red (CH). The Number in Light Purple Box Indicates the Integrations of the Protons.

In order to gain more information about this product, a COSY NMR was carried out, and shown in Figure 2.14. The two peaks at 6.75 and 5.18 ppm in the left bottom region in the cyan box have no cross coupling peaks at all. These carbon atoms, and their respective proton atoms, are proposed to be C^7 and C^{16} as those protons are not expected to show any couplings. We cannot unambiguously determine which peak represents which carbon/proton atom with the present data; additional 2-dimensional NOESY (NOESY=nuclear overhauser effect spectroscopy) measurements would be necessary to identify these protons. Turning our attention to the far-right

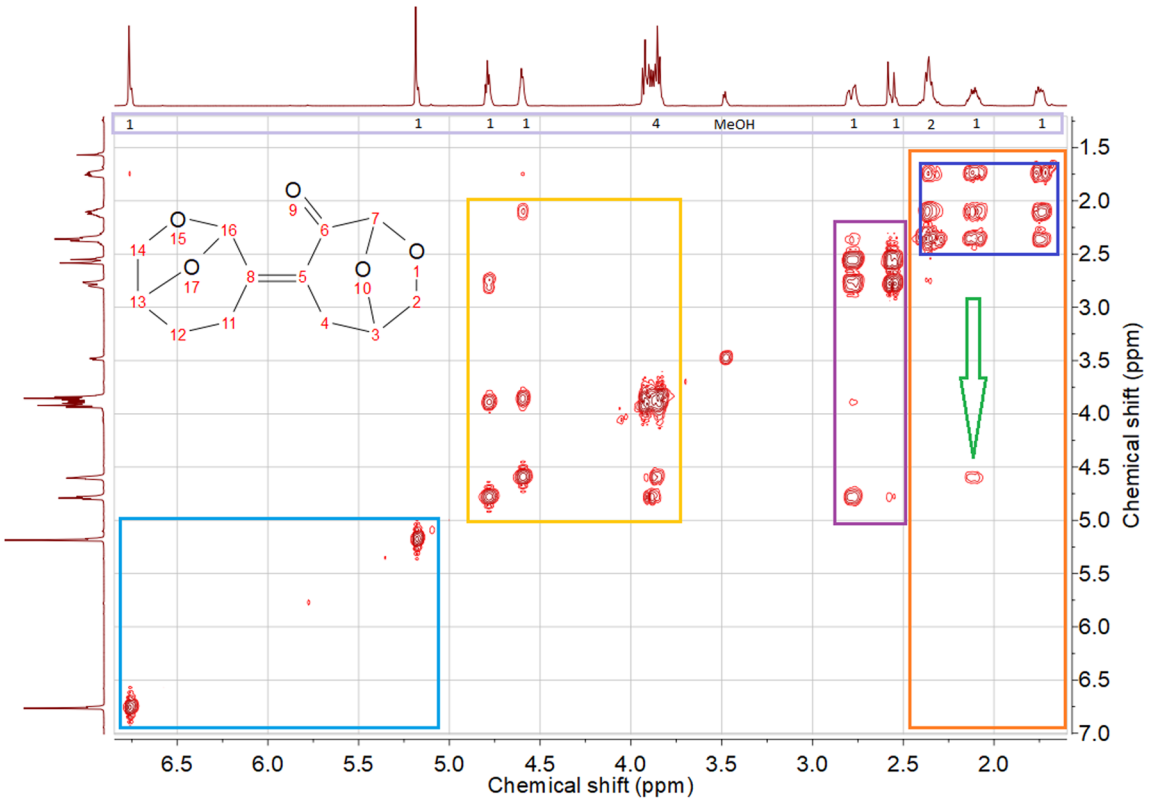

Figure 2.14: COSY Spectrum of the Cyrene Aldol-Condensation Product Dissolved in $CDCl_3$. The Numbers in the Top Light Purple Box Are the Integrations of the Peaks.

region in the blue box, we notice the protons located here are coupled to one another and belong to two sets of diastereotopic CH_2's. As such, this fragment must be a CH_2-CH_2 fragment. The only region with such a fragment is C^{11} and C^{12}. The green arrow under the blue box indicates that the proton at 2.10 ppm is also coupled to another proton at 4.60 ppm which is a CH fragment (HSQC). As such, the region in the red box must contain a $CH_{(4.60\ ppm)}$-$CH_{2(1.75\ \&\ 2.17\ ppm)}$-$CH_{2(2.37\ ppm)}$ fragment. The only portion of the molecule that fits these data is the carbons and associated protons of C^{13} (4.60 ppm), C^{12} (2.10 ppm) and C^{11} (2.37 ppm). Looking closely at

C^{13}'s cross coupling peaks in the COSY, we notice that C^{13} couples to some of the protons centered at 3.85 ppm. Given that C^{13} has been ambiguously assigned, 2 of the 4 protons at 3.85 ppm must belong to C^{14}. With this assignment, half of the molecule has been correctly identified based on the NMRs and the crystal structure.

Turning our attention to the purple box in Figure 2.14, we see diastereotopic CH_2's at 2.57 and 2.75 ppm. These protons show a strong coupling to the CH group proton at 4.80 ppm indicating that the fragment contains a CH_2-CH region. The CH group at 4.80 ppm is further coupled to the remaining 2 diastereotopic protons centered at 3.85 ppm. Thus, the remaining fragment consists of a CH_2-CH-CH_2 region with no further strong cross coupling. We thus propose that this fragment belongs to the carbon and associated protons of C^2-C^3-C^4. Given the similar chemical environments of C^{14} and C^2, we propose that these two sets of diastereotopic CH_2's are located in the region of 3.85 ppm. Meanwhile, C^4, having a similar chemical environment to C^{11}, is assigned to the protons at 2.57 and 2.75 ppm. C^3 is therefore assigned to the CH region at 4.80 ppm.

Given this, all protons have been identified based on the crystal structure obtained for the aldol-condensation product of Cyrene indicating that no other significant impurities is produced. A summary of the proton chemical shifts can be found in Table 2.5. Interestingly enough, the aldol-condensation of Cyrene occurs such that only one isomer is formed despite two isomers being possible.

With the aldol-condensation product uniquely identified as only one isomer and not a mixture of compounds, we returned our attention to the use of Cyrene as an alternative solvent for MOF synthesis. To further investigate our surface area results, thermogravimetric analysis (TGA) of the MOFs examined in this work were

Table 2.5: Chemical Shift List of Protons in Aldol-Condensation Molecule.

Left side of molecule		Right side of molecule	
Protons	Chemical shift (ppm)	Protons	Chemical shift (ppm)
$C^{11}H_2$	2.37	$C^{2}H_2$	3.85
$C^{12}H_2$	2.10	$C^{3}H$	4.80
$C^{13}H$	4.60	$C^{4}H_2$	2.57, 2.75
$C^{14}H_2$	3.85	$C^{7}H$	5.18/6.75[f]
$C^{16}H_2$	5.18/6.75[f]		

[f] The CH protons of C^{16} and C^{7} cannot be uniquely identified.

measured (Figure 2.15). Initially, DMF- and Cyrene-synthesized MOFs show similar thermal stability. However, as low as 100 °C, the Cyrene-synthesized MOFs begin to show mass loss while the DMF-synthesized MOFs do not (or do not lose as much as their Cyrene counterpart). Given that the MOFs are identical, the differences can only be rationalized by the presence of undesirable materials in the pore. The aldol-condensation product was observed to decompose around 250 °C, too high to explain the observations in the TGA. However, given the boiling point of Cyrene (203 °C), these mass losses, coupled with the observation that only Cyrene is left in the pore (Figure 2.11), are indicative of trapped pore-bound Cyrene.

Based on all the results presented herein, it is hypothesized that for MOFs with small pore-apertures, the notably larger kinetic diameter of Cyrene *vs.* DMF may require activation routines (more than conventional heating under vacuum used here), which we have not explored, in order for Cyrene to be beneficial in MOF synthe-

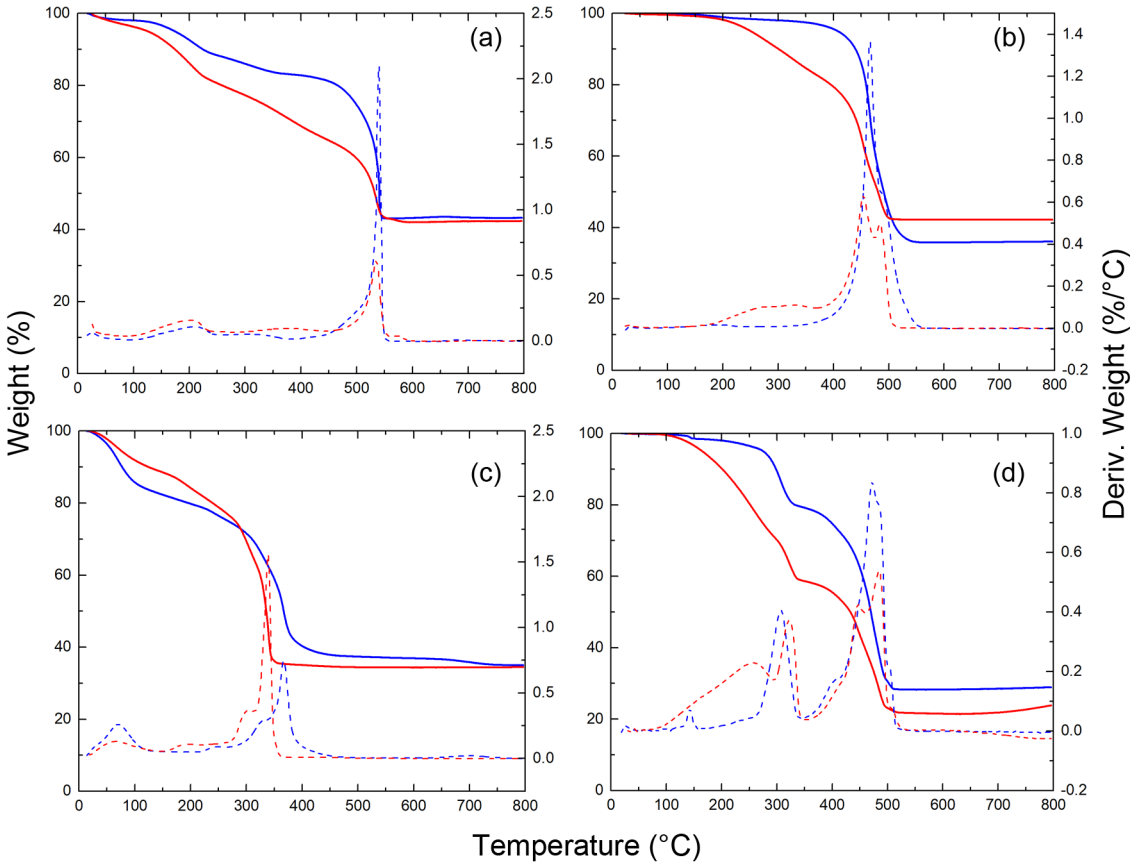

Figure 2.15: Weight Loss as a Function of Temperature (Solid Line) and Derivative of Weight Loss as a Function of Temperature (Dash Line), Blue (DMF), Red (Cyrene). TGA of (a) UiO-66, (b) ZIF-8, (c) Co-MOF-74, and (d) $Zn_2(BDC)_2(DABCO)$.

sis. These routines could be as simple as changing the solvent mixture used in the synthesis in order to remove the Cyrene before the ship-in-the-bottle is closed, as we showed with HKUST-1, or more dramatic acid-base treatments to remove the unwanted guests. However, for large-pore aperture MOFs, the inclusion of residual pore-bound Cyrene is not likely to be problematic as simply washing would be able to remove the Cyrene.[20,26,171,172]

2.3 Conclusions

In summary, an environmentally friendly dipolar aprotic solvent has been investigated for the synthesis of five distinct MOFs: HKUST-1, UiO-66, Co-MOF-74, ZIF-8, and $Zn_2(BDC)_2(DABCO)$. In all five cases, Cyrene could produce crystalline materials with PXRDs that match the expected PXRDs. As a set of design principles, we have discovered that keeping the water content of Cyrene low is critical. Additionally, decreasing the heating time is necessary to prevent the formation of the aldol-condensation product. With these points in mind, optimal BET surface areas can be easily obtained. Although an aldol-condensation product and residual Cyrene were observed in some of these MOFs, the presence of these species in or around the MOF is likely the origin of the observation that DMSO/EtOH is not an ideal alternative solvent for MOF synthesis (*i.e.*, we need to form these products in order for the beneficial acid-base chemistry associated with MOF synthesis to occur). The lessons learned herein can be extended to other MOFs which, at present, do not have non-DMF synthetic pathways. To that end, Cyrene is a suitable green replacement for DMF in MOF synthesis.

2.4 Experimental Details

2.4.1 General Procedures, Materials, and Instrumentation

Circa Group Ltd. provided Cyrene. All compounds and solvents were used as received unless otherwise noticed: 1,4-diazabicyclo[2.2.2]octane (DABCO) (Aldrich, 99 %), 2-methylimidazole (Aldrich, 99 %), 2,5-dihydroxyterephthalic acid (Aldrich, 98 %),

acetic acid (ACP, 99.7 %), cobalt(II) nitrate hexahydrate (BDH, 97 %), copper(II) nitrate trihydrate (BDH, 99.5 %), deuterated dimethyl sulfoxide (DMSO-d_6) (Cambridge, 99.5 %), deuterated sulfuric acid (D_2SO_4/D_2O; Aldrich, 99.5 atom % D), ethyl alcohol (Aldrich, denatured), ethyl alcohol (ACP, 95 %), methanol (ACP, 99.8 %), *N,N*-dimethylformamide (DMF) (Fisher, 99.9 %), terephthalic acid (Aldrich, 98 %), triethylamine (Aldrich, 99 %), trimesic acid (Aldrich, 95 %), zinc(II) nitrate hexahydrate (J.T. Baker, 99 %), and zinc(II) acetate dihydrate (J.T. Baker, 99 %).

Powder X-ray diffraction (PXRD) patterns were obtained using a Rigaku X-ray Ultima IV Diffractometer equipped with a copper X-ray source and a scintillation counter detector. Single crystal X-ray diffraction data were collected on a Rigaku diffractometer equipped with a Saturn 70 CCD detector, an AFC8 goniometer, and a molybdenum target X-ray source (Proto Manufacturing) running at 50 kV and 30 mA (1.5 kW). Crystals were glued on a glass fiber. All data were collected at ambient temperature using 5 s exposure and processed using CrysAlis Pro. Structure solutions were performed in Olex 2.

Nitrogen gas adsorption isotherm data were collected at 77 K on a TriStar II PLUS surface area and porosity analyzer. All the samples were activated before each isotherm by heating the samples in a vacuum oven.

^{1}H NMR measurements were performed on a Bruker Avance III 300 instrument. Samples were digested in D_2SO_4/DMSO-d_6 mix solution and filtered before measuring by Bruker Avance III. DMSO-d_6 was used as the lock solvent.

2-dimensional NMR measurements were carried out on a Bruker Avance 500 instrument. Samples were dissolved in $CDCl_3$ before measuring.

Thermogravimetric analysis (TGA) experiments were performed on a TA Instru-

ments Q500 interfaced with a PC using TA Instruments software (version 4.7A). Samples were placed in a platinum pan and heated at a rate of 10 °C/min from 25 to 800 °C under a nitrogen atmosphere.

2.4.2 Synthesis of MOFs Using DMF

UiO-66 (DMF),[23] Co-MOF-74 (DMF),[35] and $Zn_2(BDC)_2(DABCO)$[173] were synthesized from DMF as previously reported. For consistency, the synthetic methods used are outlined below.

a) HKUST-1: A 2-dram vial was charged with trimesic acid (H_3BTC, 25.0 mg, 0.120 mmol), copper(II) nitrate trihydrate (43.0 mg, 0.175 mmol) and a mixture of solvents of DMF–ethanol–deionized water (see Table 2.1). Once the reagents were dissolved by agitation, the mixture was heated at 80 °C overnight. The resulting solid was washed with 3 × 10.0 mL of DMF. Subsequently, the DMF was exchanged daily with ethanol for 3 days. After filtration, the sample was dried under a vacuum at 150 °C, yielding a purple-blue crystalline solid.

b) UiO-66: A 25 mL vial was charged with zirconium(IV) chloride (123.3 mg, 0.529 mmol), DMF (5.0 mL), and hydrochloric acid (1.0 mL). Once dissolved after 15 min sonication, terephthalic acid (123.8 mg, 0.745 mmol) and 10 mL DMF were added to the previous mixture and sonicated for an additional 15 mins. The mix solution was placed in an oven at 80 °C for 12 h. The resulting white solid was washed with 3 × 10.0 mL of DMF and subsequently 3 × 10.0 mL of ethanol. After filtration, the sample was dried under a vacuum for 12 h at 80 °C.

c) ZIF-8: A 25 mL vial was charged with zinc(II) acetate dihydrate (500.0 mg,

2.278 mmol), 2-methylimidazole (400.0 mg, 4.872 mmol), and 20.0 mL of DMF. Once dissolved, the solution was heated at 110 °C for 24 h. The resulting white precipitate was washed with 3 × 10.0 mL DMF and subsequently 3 × 10.0 mL methanol. The solvent was filtered and dried under vacuum at 80 °C overnight yielding a white solid.

d) Co-MOF-74: A 25-mL vial was charged with 2,5-dihydroxyterephthalic acid (43 mg, 0.217 mmol), ethanol (10.0 mL), DMF (10.0 mL) and water (10.0 mL). Once dissolved by sonication, cobalt(II) nitrate hexahydrate (217.0 mg, 0.746 mmol) was added to the previous solution and an additional 15 min of sonication was applied. A dark pink solution was formed after completely dissolution. The solution was subsequently placed in an oven at 100 °C for 24 h. The resulting brown crystalline material was washed with 3 × 10.0 mL methanol. Subsequently, the remaining solvent was exchanged daily with methanol for 3 days. At this point, the sample was filtered and dried under a vacuum for 12 h at ambient temperature, and subsequently for an additional 12 h at 150 °C, yielding a dark-red crystalline product.

e) $Zn_2(BDC)_2(DABCO)$: A mixture of DABCO (93.5 mg, 0.835 mmol), zinc(II) nitrate hexahydrate (500.0 mg, 1.180 mmol), and terephthalic acid (H_2BDC, 280.0 mg, 1.180 mmol) was suspended in DMF (20.0 mL) in a 25-mL vial before being heated in an oven at 120 °C for 48 h. The solvent was replaced daily for 3 days. Afterwards, the sample was filtered and dried under a vacuum at 110 °C overnight, yielding a white powder.

2.4.3 Synthesis of MOFs Using Cyrene

As demonstrated below, even when Cyrene was used as a solvent, DMF was used as the wash solvent in order to prevent the SA results from Cyrene to be complicated by reagents/products, which would be soluble in DMF but may not be soluble in Cyrene.

a) HKUST-1: A 2-dram vial was charged with trimesic acid (H_3BTC, 25.0 mg, 0.120 mmol), copper(II) nitrate trihydrate (43.0 mg, 0.175 mmol) and a mixture of solvents of Cyrene–ethanol–deionized water (see Table 2.1). Once the reagents were dissolved by agitation, the mixture was heated at 80 °C overnight. The resulting solid was washed with 3 × 10.0 mL of DMF. Subsequently, the DMF was exchanged daily with ethanol for 3 days. After filtration, the sample was dried under a vacuum at 150 °C, yielding a purple-blue crystalline solid.

b) UiO-66: A 2-dram vial was charged with zirconium(IV) oxychloride octahydrate (34.8 mg, 0.108 mmol), DMF (100 μL), acetic acid (135 μL), deionized water (100 μL) and Cyrene (1000 μL). Once dissolved, terephthalic acid (24.6 mg, 0.149 mmol) as well as Cyrene (1000 μL) were added to the previous mixture. The mixture was placed in an oven at 80 °C for 12 h. The resulting off-white solid was washed with 3 × 10.0 mL of DMF and subsequently 3 × 10.0 mL of methanol. After filtration, the sample was dried under vacuum at 80 °C for 12 h.

c) ZIF-8: 2-methylimidazole (40.0 mg, 0.487 mmol), zinc(II) nitrate hexahydrate (67.8 mg, 0.228 mmol) and 3.0 mL of Cyrene were loaded in a 2-dram vial. Once dissolved, 2-equivalent (relative to 2-methylimidazole) of triethylamine was added before being heated at 110 °C for 10 h. The resulting white precipitate was washed

with 3 × 10.0 mL of DMF and subsequently 3 × 10.0 mL of methanol. The solvent was filtered and dried under a vacuum at 80 °C overnight, yielding a white solid.

It is worth noting that the shorter heating time of Cyrene (10 h) *vs.* DMF (24 h) was chosen in order to prevent the formation of the aldol-condensation product. Furthermore, zinc(II) nitrate hexahydrate was used in the synthesis of ZIF-8 from Cyrene due to the increased solubility of the nitrate salt *vs.* the acetate salt.

d) Co-MOF-74/Co-CPO-27: A 25 mL vial was charged with 2,5-dihydroxyterephthalic acid (43.0 mg, 0.217 mmol) and an 18.0 mL mixture of solvent (Cyrene/100 % ethanol, v/v=1:1), the sample was subsequently agitated for 10 min before cobalt(II) nitrate hexahydrate (217.0 mg, 0.746 mmol) was added. Once dissolved, it was heated in a 100 °C oven overnight. The resulting solid was washed first with 3 × 10.0 mL of DMF. The solvent was then decanted and replaced with methanol daily for 3 days. After filtration, the sample was dried under a vacuum for 12 h at ambient temperature, and subsequently for an additional 12 h at 150 °C, yielding a dark-red crystalline product.

e) $Zn_2(BDC)_2(DABCO)$: A mixture of zinc(II) nitrate hexahydrate (50.0 mg, 0.168 mmol), terephthalic acid (H_2BDC, 27.9 mg, 0.168 mmol) and DABCO (9.4 mg, 0.084 mmol) were suspended in Cyrene (2.0 mL) in a 2-dram vial before being heated in an oven at 100 °C for 12 h. The solvent was decanted and replaced with DMF daily for 3 days. After filtration, the sample was dried under a vacuum at 110 °C overnight, yielding a white powder product.

Chapter 3

MOFs for Sulfur Dioxide Sequestration[‡]

3.1 Introduction

Given that sulfur dioxide is a major air pollutant which has significant impacts upon human health, as described in Chapter 1, the present chapter aims to investigate the gas adsorption of sulfur dioxide into MOFs. Adsorption can be classified into two major categories, chemical adsorption and physical adsorption.[174] Physical adsorption (physisorption) primarily occurs through van der Waals interactions. In this case, the adsorbent is non-specific to the analyte being adsorbed. Regeneration of the adsorbent is often accomplished *via* mild heating, vacuum, or even flowing another

[‡]Part of the work in this chapter is reproduced here with permission from Zhang, Jinfeng; DeCoste, Jared B; and Katz, Michael J, Investigating the cheletropic reaction between sulfur dioxide and butadiene-containing linkers in UiO-66. Can. J. Chem. 2017. Copyright 2017 Canadian Science Publishing.

gas through the material to remove the previously adsorbed molecules. In chemical adsorption (chemisorption), the adsorbent reacts with the analyte such that it is chemically bound to the adsorbent.[63] Depending on the applications, chemical or physical adsorption may be preferred. For chemical separation in industrial processes, physical adsorption may be preferred so that the adsorbent can be easily regenerated rather than replaced, and the gas can be subsequently utilized as a value-added product to industry. However, when it comes to human health protection (*e.g.*, civilians and soldiers), chemisorption is typically a better option as the risk of a toxic gas being released by the adsorbent is significantly lower in comparison to physisorption.

Another key requirement of a good adsorbent is the available surface area for the adsorbent to adsorb onto. The larger the surface area of the adsorbent, the shorter the geometric path length needs to be for efficient removal of any analyte. For this reason, high surface area architectures such as nanoparticles,[175–178] opal/inverse opal arrays,[179] fibrous materials such as aerogels,[180–183] activated carbons,[184–188] and zeolites[189–192] have all been featured in chemical separations. MOFs, however, provide a scaffold which can be more easily tuned towards sulfur dioxide. By adjusting the functionality of the linker, the pore size *via* the length of the linker, and the geometry of the node or the chemistry of the node *via* the metal node, an iterative process can be used to optimize sulfur dioxide binding. Thus, this chapter focuses on developing a criterion for the features that necessitate efficient sulfur dioxide binding in MOFs.

Considering this chapter focuses on the ability to rapidly sequester sulfur dioxide from the air, it is critical to introduce an alternative method by which the efficiency of gas adsorption can be determined. The most conventional method of describing the ability of MOFs to sequester gases is an adsorption isotherm, which describes the

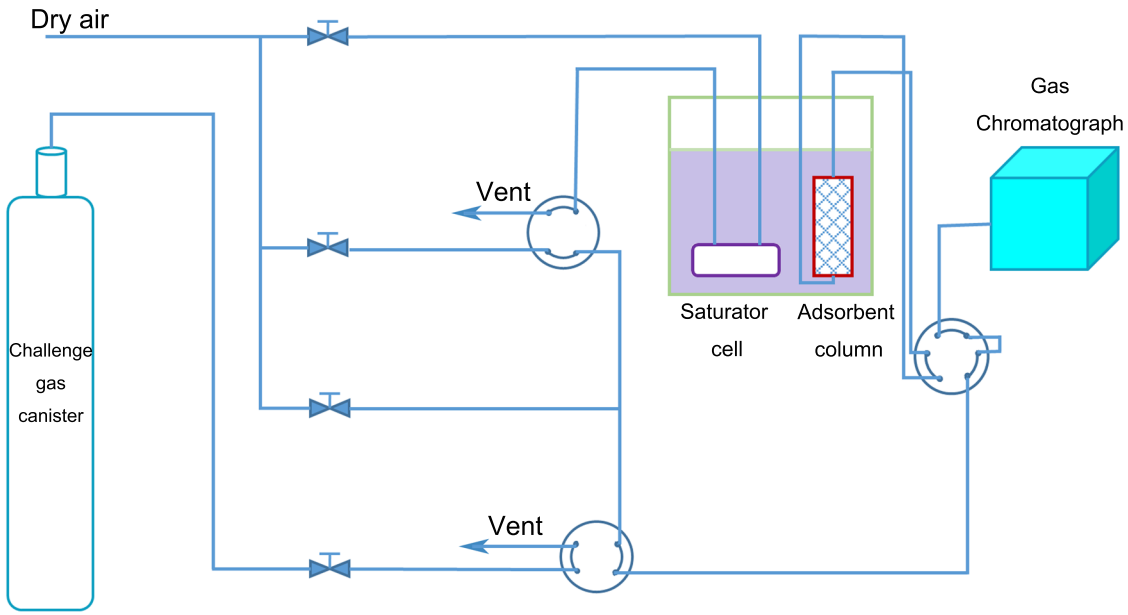

Figure 3.1: Schematic Picture of Micro-Breakthrough Experiments.

equilibrium relationship between a probe molecule in the gas phase (*e.g.*, nitrogen in Chapter 2) and the molecule adsorbed on the surface (internal and external) of an adsorbent (*e.g.*, a MOF).[193] The challenge with an adsorption isotherm is that it represents the best case scenario that the gas molecules have time to reach equilibrium before the amount of gas adsorbed is determined. However, when used in a gas mask, the kinetics of gas adsorption are also important. For example, if we have an adsorbent that has a high adsorption capacity but slow adsorption kinetics, then it will take very little time for a gas to pass through a gas mask. However, an adsorbent that has a lower adsorption capacity but high adsorption kinetics will take longer to pass through a gas mask. The time it takes for an adsorbing species to pass through a material is determined *via* its breakthrough kinetics. A schematic of the micro-breakthrough analysis apparatus is shown in Figure 3.1.

In a breakthrough analysis, an instrument monitors the concentration of a gas downstream from an adsorbent as a function of time. An idealized breakthrough curve[194] of a fixed bed adsorbent is shown in Figure 3.2. The breakthrough point occurs when the concentration of the gas leaving the adsorbent has starts to rise in concentration (i.e., unadsorbed solute begins to emerge). The quantity of adsorbed amount of solute or impurities at a constant flow (*i.e.*, the dynamic loading) can be calculated from the area above the curve between t = 0 and the breakthrough time ($C/C_0 = 1$).

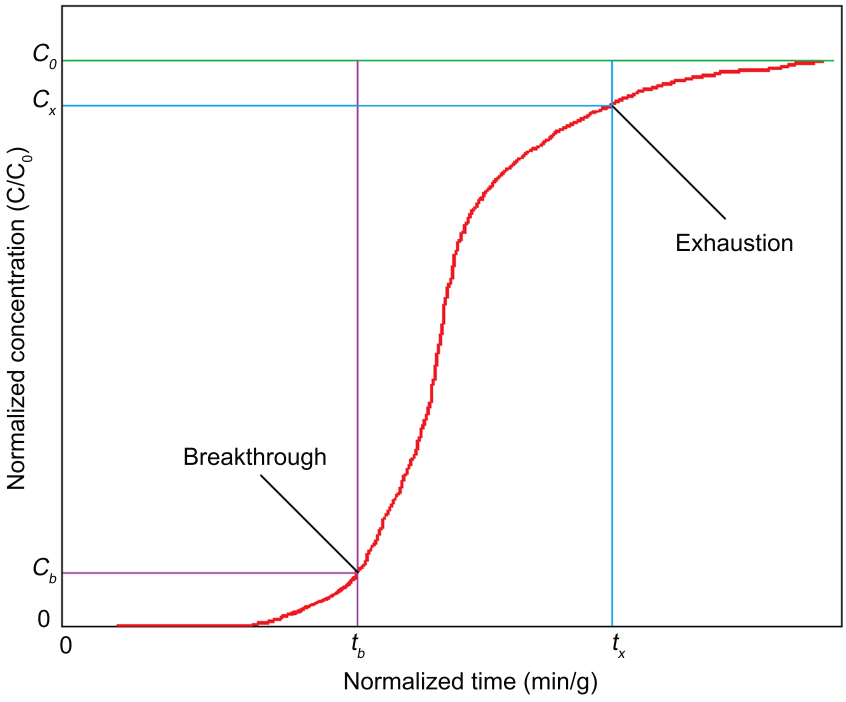

Figure 3.2: Idealized Breakthrough Curve of a Fixed Bed Adsorbent. C_b and C_x Represent the Concentration of Effluent at Breakpoint and Exhaustion, Respectively; C_0 Is the Initial Concentration of Influent. t_b and t_x Are the Time Spend by the Effluent at Breakpoint and Exhaustion, Respectively.

Turning our attention back to sulfur dioxide removal in MOFs, the aim of this portion of the thesis is to introduce functional groups, which are capable of reacting with sulfur dioxide into MOFs. As shown in Figure 3.3, 1,3-Butadiene, and its derivatives, have been shown to chemically react with sulfur dioxide to form a butadiene sulfone (sulfolene).[195–197] This reaction, called a cheletropic reaction, is known to be reversible under elevated temperature.[195,198,199] Thus, we hypothesize that incorporation of 1,3-Butadiene into a MOF will improve the removal of sulfur dioxide.

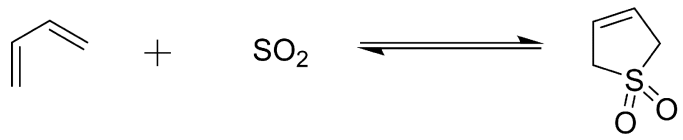

Figure 3.3: Scheme of Reaction Between 1,3-Butadiene and Sulfur Dioxide.

The following sections illustrate two different methods by which sulfur dioxide adsorption will be investigated in MOFs. The methods include installing functionalized organic linkers to MOFs by replacing original linkers and incorporating organic ligands onto MOFs.

3.1.1 Post-Synthesis Installation of Potentially Reactive Sulfur Dioxide Linkers

The role of the linker in the MOF is two-fold. Firstly, it links nodes to one another. Secondly, it can also be synthetically tuned in order to improve a chemical process in the pore (*e.g.*, sulfur dioxide sequestration). To illustrate the efficacy of this method, Katz *et al.*[200] demonstrated that when the terephthalic acid linker in UiO-66 (Fig-

ure 1.8) was exchanged for 2-aminoterephthalic acid, forming UiO-66-NH_2, then the hydrolysis rate of a phosphate ester nerve agent simulant was enhanced 20-fold. Similarly, we have investigated the modification of the linker in order to introduce sulfur dioxide reactive materials.

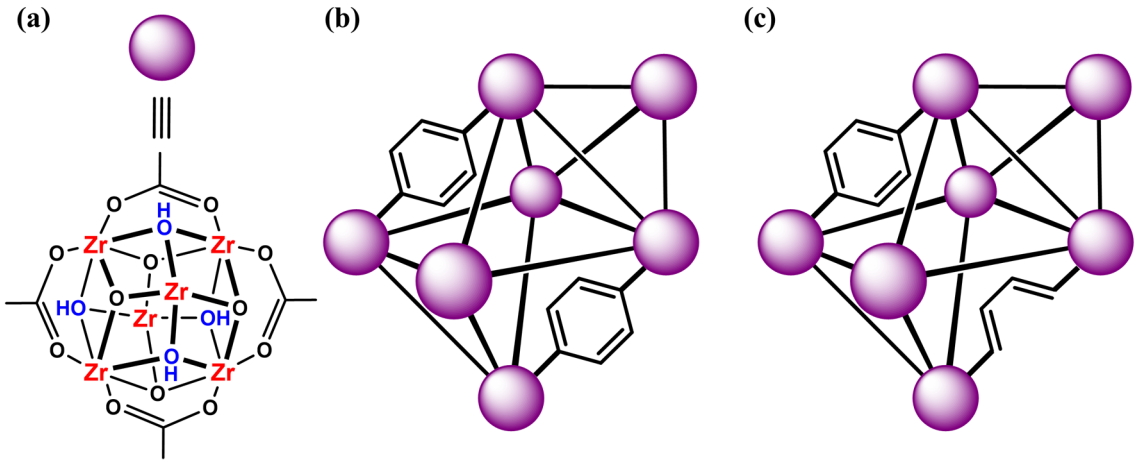

Figure 3.4: (a) A $[Zr_6O_4(OH)_4]^{12+}$ Cluster Showing 4 of 12 μ-BDC Units. (b) Schematic Drawing of UiO-66. (c) Schematic Drawing of UiO-66-MA Illustrating How the Organic Linkers Were Partly Replaced by Muconic Acid.

One potential linker that would allow us to investigate this chemistry is *trans,trans*-muconic acid, a commercially available chemical which contains two carboxylic acids and the desirable butadiene functional group (Figure 3.23, **6**). With this linker, a highly stable Zr-containing MOF (UiO-66; Figure 3.4) was selected to incorporate *trans,trans*-muconic acid into its structure *via* post-synthetic exchange (PSE). The resulting MOF (UiO-66-MA (muconic acid)) was characterized to illustrate the role this MOF has on sulfur dioxide sequestration.

Another attempt we investigated was trying to incorporate a butadiene group

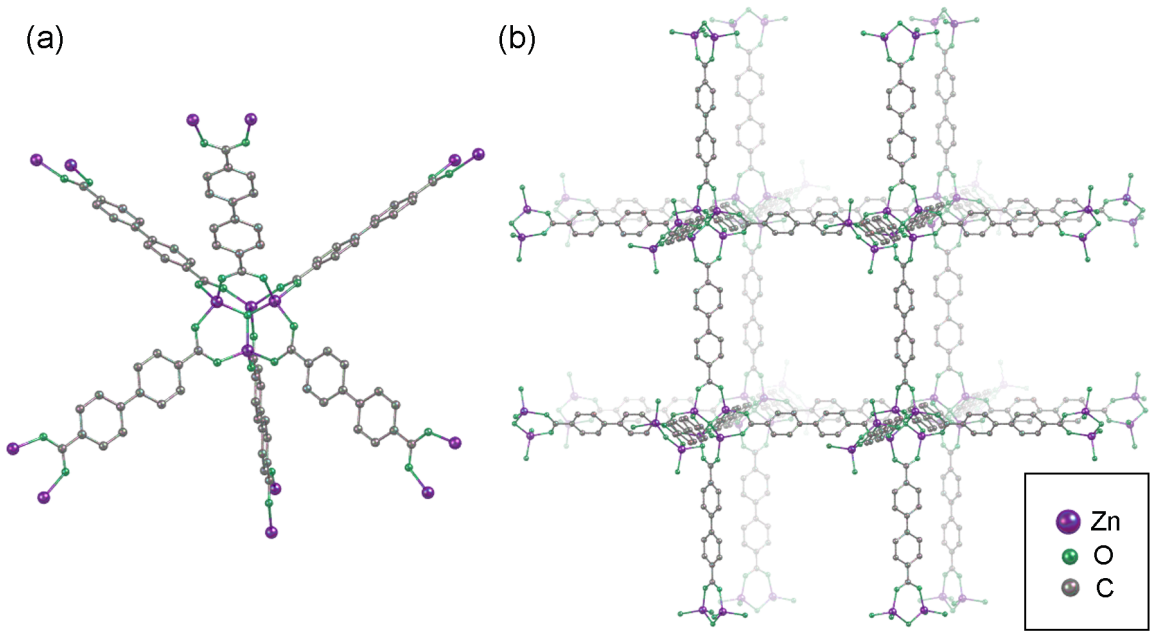

Figure 3.5: (a) Schematic Fragment Showing How Zn(II) Cation Nodes Coordinated with BPDC Linkers Surrounded. (b) Schematic Pore Structure of IRMOF-10.

into a MOF using a biphenyldicarboxylate linker which possessed a butadiene sulfone (Figure 3.22, **21**). With the linker in hand, our hopes were to be able to thermally remove the sulfur dioxide to form the butadiene linker (BPDC-BD) either before forming the MOF, or post-synthesis (*i.e.*, after the MOF is formed). For this linker, IRMOF-10 (Figure 3.5) was selected as the target parent MOF and synthesized as a comparison to the BPDC-BD-based IRMOF-10 in order to test our hypothesis in this system.

3.1.2 Post-Synthesis Installation of Monodentate Ligands That Are Potentially Reactive Toward Sulfur Dioxide onto MOF Nodes

Another post-synthesis method that can be used to introduce functional groups onto the surface of the MOF framework is solvent assistant ligand incorporation (SALI).

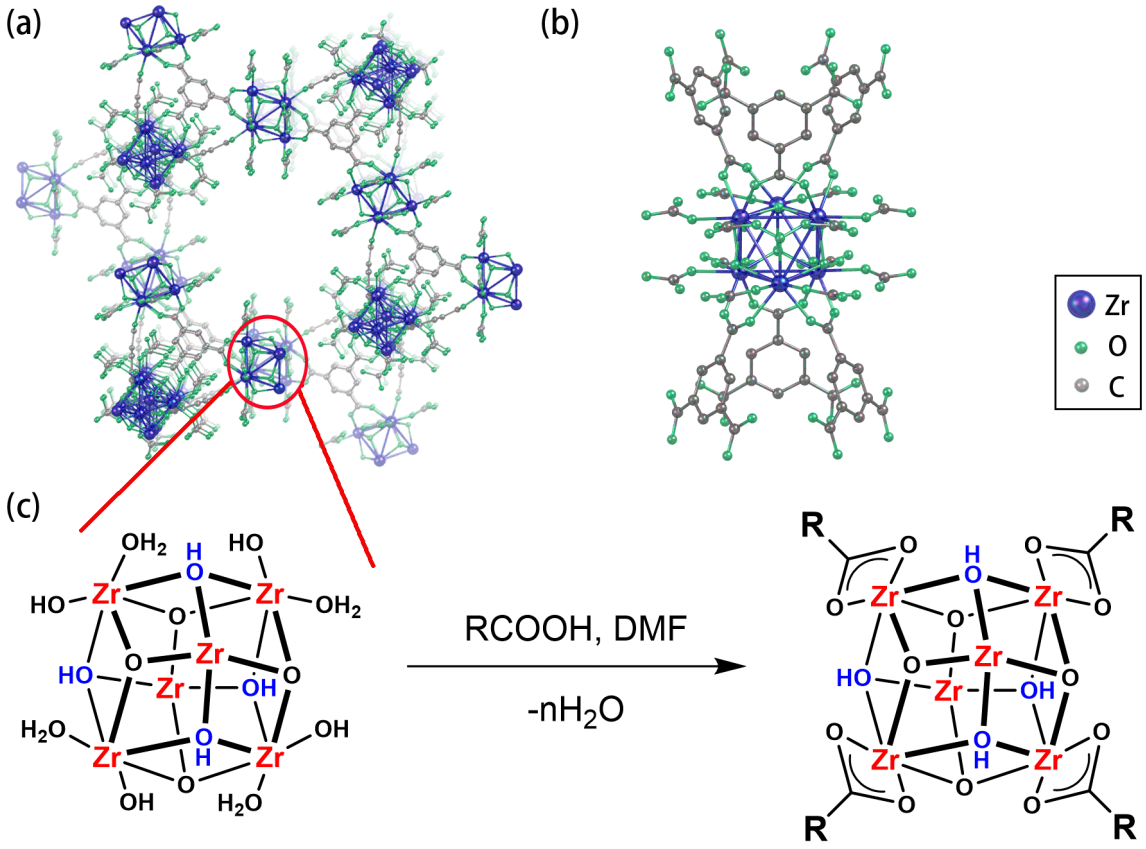

Figure 3.6: (a) 3-Dimensional Structure of MOF-808 Illustrating the Adamantane Pore; (b) Schematic Fragment Showing How $[Zr_6O_4(OH)_4]^{12+}$ Cluster Nodes Coordinated with BTC Linkers; (c) Schematic Representation of the SALI in the MOF-808 Platform.

Like post-synthetic exchange, the parent MOF is synthesized in the absence of the desired functional groups. Instead of replacing linkers or nodes, functionalized ligands are incorporated onto the node of the framework.

For this to work, the node must have some open coordination sites or a coordination site that can be easily substituted. Due to its unsaturated nodes, MOF-808 (Figure 3.6) is a perfect example of a MOF in which SALI can be performed. As shown in Figure 3.6, the node of MOF-808 consists of a $[Zr_6O_4(OH)_4]^{12+}$ cluster with a combination of one terminal water and one terminal hydroxide per Zr centre. If the MOF is subsequently soaked in a solution containing a carboxylic acid, then the terminal water and hydroxide can be replaced by a carboxylate moiety (Figure 3.6). In the present work, a butadiene-containing carboxylic acid will be employed (Figure 3.19). To compare the role of the butadiene-containing MOF (MOF-808-BD), unfunctionalized MOF-808, and MOF-808 with butadiene sulfone (MOF-808-BS) were synthesized for comparison.

3.2 Results and Discussion

3.2.1 UiO-66 and UiO-66-MA: Post-Synthesis Installation of Potentially Reactive Sulfur Dioxide Linkers

To start, we began our investigation with UiO-66 and UiO-66-MA. Both MOFs were made according to literature methods (see experimental section). To ensure that the MOF remained intact after linker incorporation, the PXRD of UiO-66 and UiO-66-MA were measured and compared to the simulated spectrum of UiO-66. The

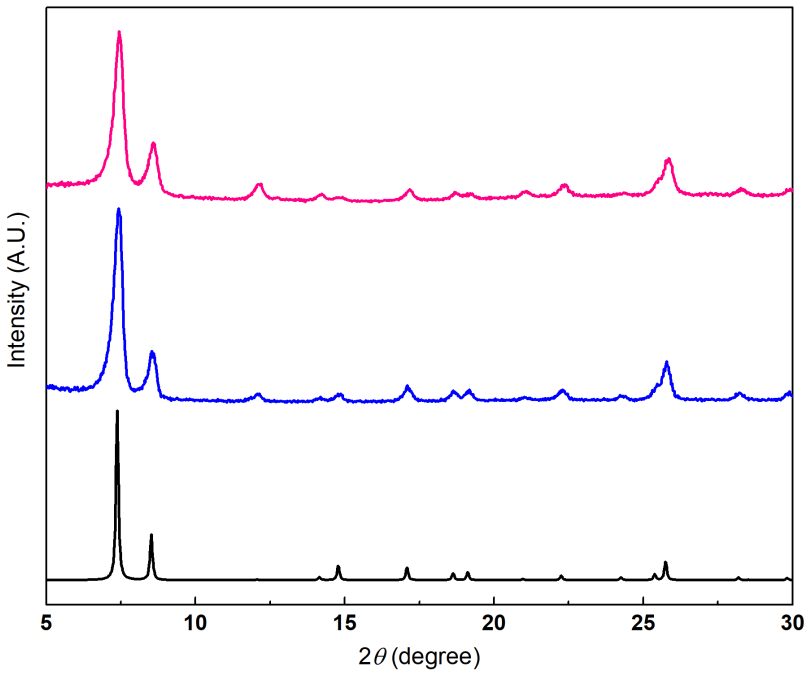

Figure 3.7: Simulated UiO-66 (Black Bottom) and Observed, UiO-66 (Blue Middle), UiO-66-MA (Pink Top), Powder X-ray Diffraction Patterns.

diffractograms of both UiO-66 and UiO-66-MA (Figure 3.7) are identical indicating that the structure of the crystalline material is consistent with the structure of UiO-66. Given the strong similarities between the diffractograms in Figure 3.7 and by Guillerm *et al.*,[201] the *trans,trans*-muconic acid likely undergoes a *cis/trans* isomerization.

To confirm the formation of UiO-66-MA from UiO-66, the ^{1}H NMR of an acid-digested sample of UiO-66-MA was measured. As seen in Figure 3.8, UiO-66-MA not only showed the terephthalic acid peak at 7.95 ppm, but also the muconic acid peaks at 6.27 and 7.27 ppm with an integration ratio of 1.00:0.34 BDC:muconic acid; the combined integration of both muconic acid peaks equaled 0.34 ppm. This indicates that there is a 1 to 3 ratio of muconic acid to terephthalate linkers. Alternatively,

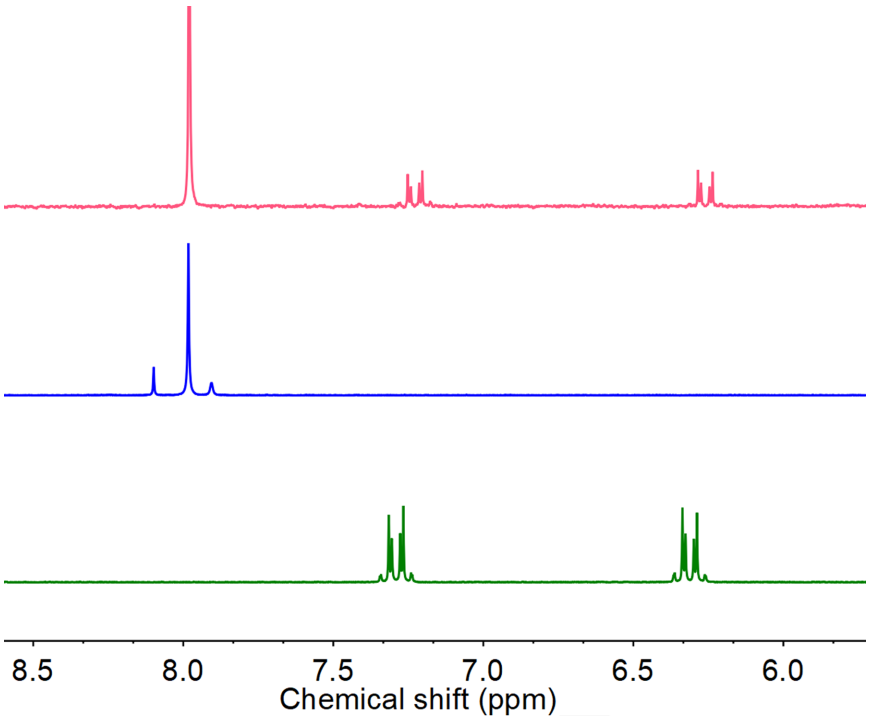

Figure 3.8: ^{1}H NMR Spectrum of UiO-66-MA (Pink Top), UiO-66 (Blue Middle) and *trans,trans*-Muconic Acid (Green Bottom).

of the total number of linkers, roughly 25 % of the linkers are muconic acid. Lastly, we further measured the gas adsorption isotherms to confirm that the muconic acid linker was incorporated into the MOF instead of simply being trapped in the pore. To that end, the nitrogen gas-adsorption isotherms of UiO-66 and UiO-66-MA were measured at 77 K. As shown in Figure 3.9, the isotherms for the MOFs are similar; the BET surface areas of UiO-66 and UiO-66-MA are 1200 and 1000 m^2/g, respectively.

With UiO-66-MA in hand, the micro-breakthrough measurement was carried out using a 1000 mg/m^3 sulfur dioxide challenge concentration. Each MOF was exposed to the challenge concentration *via* a 20 mL/min flow rate using dry nitrogen as the carrier gas. A 9.3 mg sample of UiO-66 and 11.5 mg sample of UiO-66-MA were

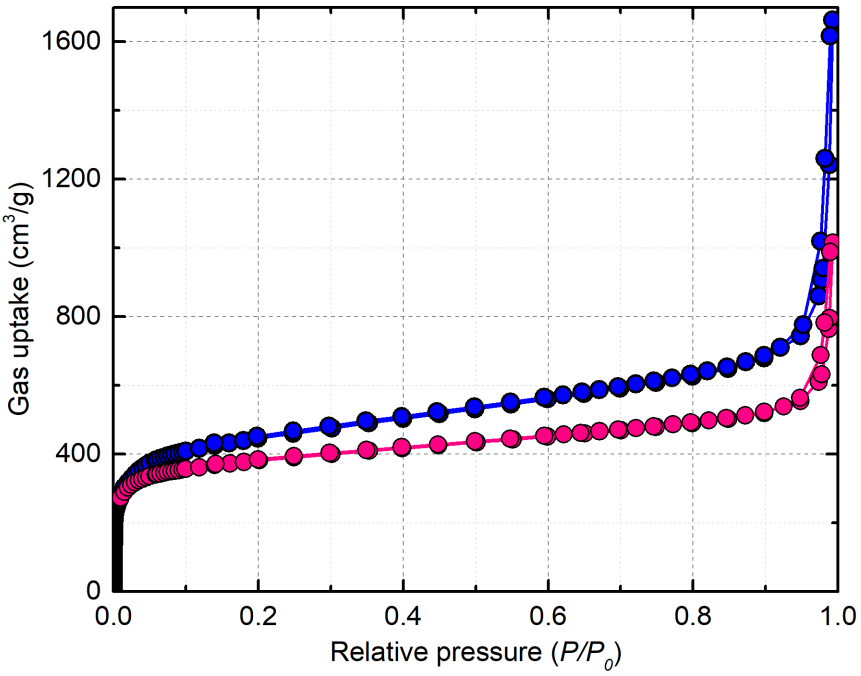

Figure 3.9: Nitrogen Gas Adsorption Isotherms (77 K) of UiO-66 (Blue) and UiO-66-MA (Pink).

packed into a 4 mm long tube having a 4 mm internal diameter. The downstream gas concentration was measured using a GC equipped with a flame photometric detector.

Sulfur dioxide micro-breakthrough and desorption curves are shown in Figure 3.10 and summarized in Table 3.1. The quantity of adsorbed sulfur dioxide at constant flow (*i.e.*, the dynamic loading) can be calculated from the area above the curve between t = 0 and the breakthrough time ($C/C_0 = 1$). From this data, UiO-66 and UiO-66-MA exhibited an effective loading of 0.18 and 0.58 mol/kg, respectively. UiO-66-MA showed a nearly 3 times increase in sulfur dioxide adsorption when compared to the parent MOF UiO-66. Considering the maximum loading is 0.9 mol/kg for UiO-66-MA, assuming no linker defects[202–209] exist in the MOF and every muconic acid reacts with one sulfur dioxide, then sulfur dioxide is able to interact with 64 %

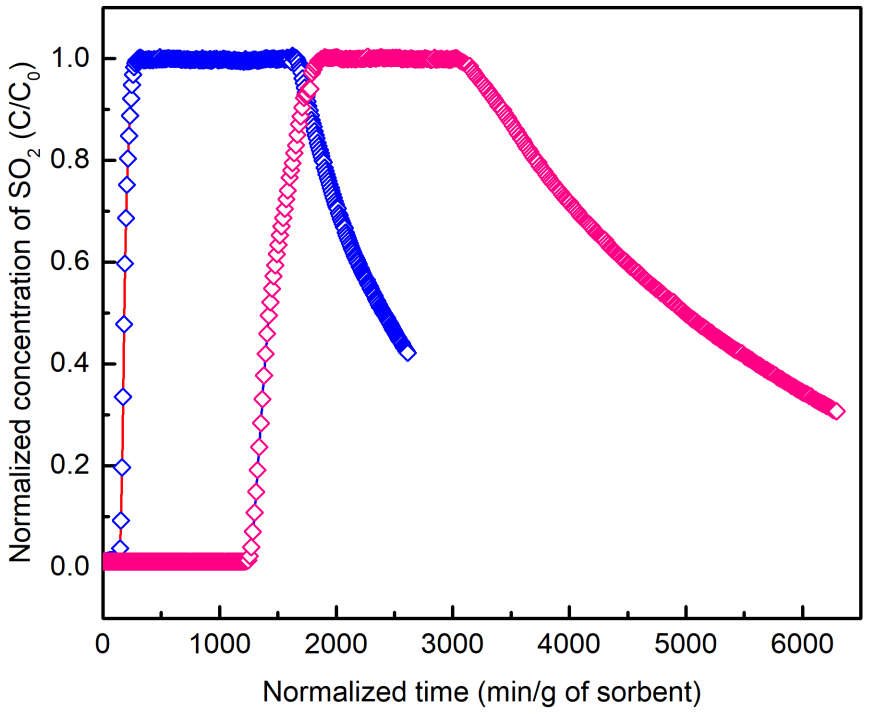

Figure 3.10: Sulfur Dioxide Micro-Breakthrough and Desorption Curves Under Dry Condition for UiO-66 (Blue) and UiO-66-MA (Pink).

of the active sites before breakthrough.

Table 3.1: Dynamic Loading of Sulfur Dioxide on UiO-66 and UiO-66-MA.

	Sorbent mass (mg)	Effective loading (mol/kg)
UiO-66	9.3	0.18
UiO-66-MA	11.5	0.58

To probe the chemistry of how sulfur dioxide is incorporated into UiO-66 *vs.* UiO-66-MA, we measured the IR of the MOFs before and after gas adsorption. As shown in Figure 3.11, there is no significant change in the spectrum before or after the

breakthrough measurement. If chemisorption was to occur, then it would be expected that new peaks at *ca.* 1100-1300 cm^{-1} would be observed for UiO-66-MA.[210]

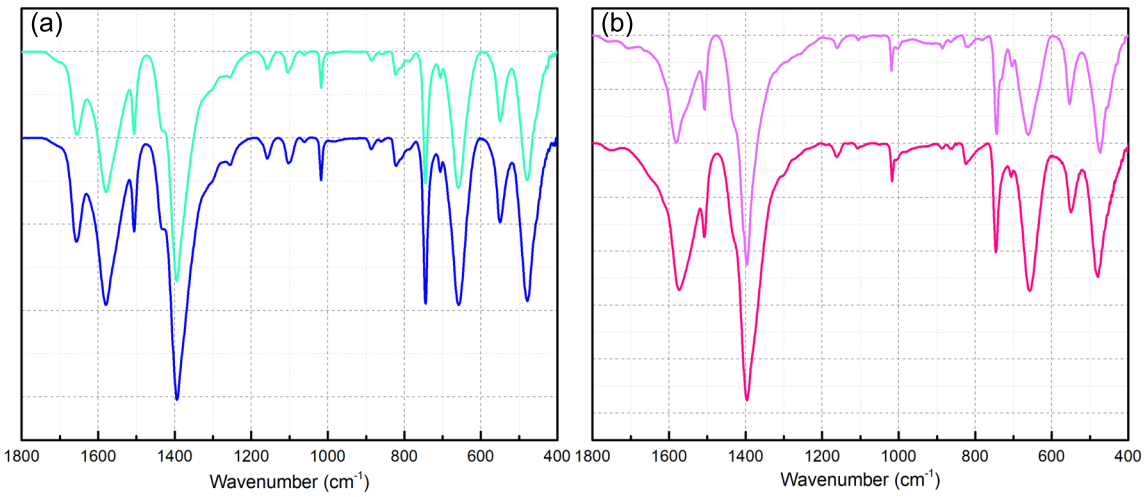

Figure 3.11: FT-IR of MOFs Before and After Sulfur Dioxide Adsorption. (a) UiO-66 Before (Blue Bottom), After (Cyan Top); (b) UiO-66-MA Before (Pink Bottom), After (Mauve Top).

To further examine the reaction between sulfur dioxide and UiO-66-MA, UiO-66-MA was digested in D_2SO_4/DMSO-d_6 to investigate any change to the muconic acid *via* ^{1}H NMR. As shown in Figure 3.12, the spectrum of UiO-66-MA before and after sulfur dioxide exposure remain unchanged indicating that sulfur dioxide is most-likely physically adsorbed and not chemically reacted with the muconic acid.

Given the data presented herein, under these reaction conditions, UiO-66-MA does not undergo a cheletropic reaction with sulfur dioxide. However, the muconic acid does participate in sulfur dioxide adsorption. In the presence of the muconic acid-containing MOF, there is a 3-fold increase in dynamic sulfur dioxide adsorption. With

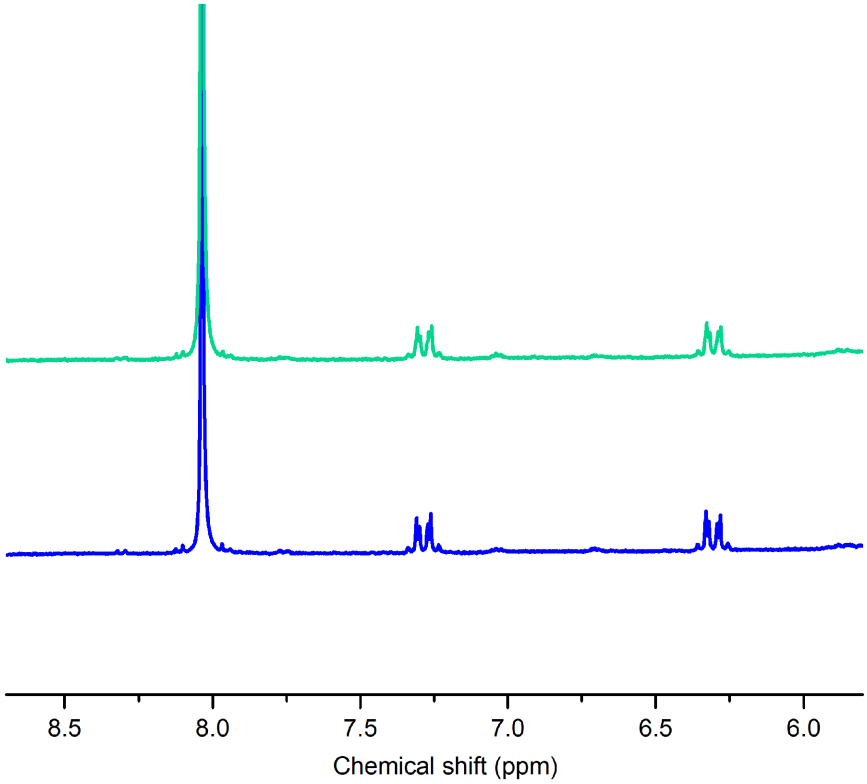

Figure 3.12: ^{1}H NMR Spectrum of UiO-66-MA, Before (Blue Bottom), and After (Green Top) Sulfur Dioxide Sequestration.

that in mind, we propose that the rate of reaction for the cheletropic reaction is too slow to form a sulfolene. Instead, we propose that an interaction, rather than a bond, between sulfur dioxide and muconic acid is formed, at best. Alternatively, DeCoste and co-workers have demonstrated that oxalic acid modified UiO-66 is capable of increasing the sulfur dioxide adsorption.[211] In our system, we do not observe any changes in the IR spectrum of UiO-66-MA before/after sulfur dioxide adsorption, as was observed for the oxalic acid-modified UiO-66.[211] This may be due to the complete desorption of sulfur dioxide prior to IR measurements. However, we cannot rule out that residual terminal carboxylate units, left behind by incomplete muconic

acid incorporation (*i.e.*, the attachment of only one of the two carboxylate groups), are able to interact sulfur dioxide in order to increase adsorption.

3.2.2 MOF-808 and Derivatives: Post-Synthesis Installation of Monodentate Ligands Potentially Reactive Toward Sulfur Dioxide onto MOF Nodes Applied in Sulfur Dioxide Sequestration.

Although UiO-66-MA was not able to undergo a cheletropic reaction, the observa-

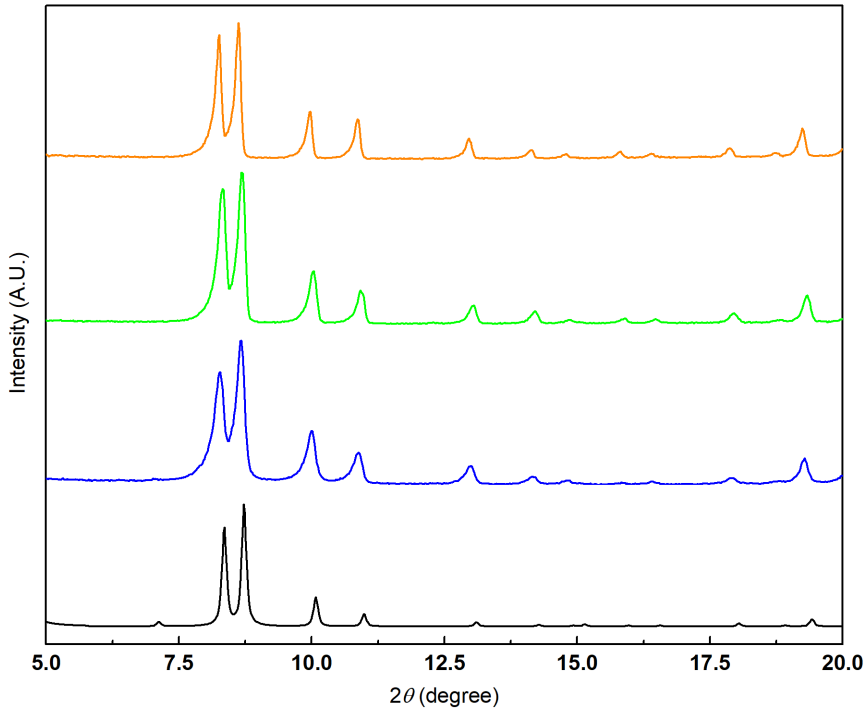

Figure 3.13: Simulated MOF-808 (Black) and Observed, MOF-808 (Blue), MOF-808-BS (Green), and MOF-808-BD (Orange), Powder X-ray Diffraction Patterns.

tion that an increase in sulfur dioxide uptake encouraged us to continue investigating our other systems. To that end, we turned our attention to more synthetically cumbersome methods to incorporate sulfur dioxide adsorbing groups. Herein, SALI-modified MOF-808 were investigated here. Specifically, three MOFs were synthesized, MOF-808, the parent MOF necessary to give us a baseline for sulfur dioxide uptake, MOF-808-BS, a MOF that contained the sulfolene and thus was unable to react, and MOF-808-BD, a MOF contained butadiene which, in theory, would be able to react with sulfur dioxide.

MOF-808 and its derivatives were synthesized by conventional methods.[124] The PXRDs of the MOFs are shown in Figure 3.13. All the diffraction peaks can be well indexed to simulated crystalline MOF-808 and no major diffraction peaks from any other impurities were detected thereby suggesting that the SALI process did not modify the MOF-808 framework topology.

As illustrated by the ^{1}H NMR results in Figure 3.14, MOF-808 only showed chemical shifts associated with the BTC linker (8.45 ppm) and DMF peaks. When SALI is applied to form MOF-808-BS, three new singlet peaks related to butadiene sulfone group (4.00, 4.14, and 6.97 ppm) appear in the NMR spectrum of MOF-808-BD. Meanwhile, if only butadiene-containing ligand was installed in MOF-808 to form MOF-808-BD, then three new multi-peaks were detected at 5.00, 5.77 and 6.71 ppm. In addition, the ratio of the BTC to SALI ligand integrations indicate that the SALI-formed MOFs contain 6 SALI ligand molecules per node. It is worth noting that there is a slight chemical shift difference between the various specta in Figure 3.14. This is primarily due to the slight differences in acid concentration used in the MOF digestion leading to a different dielectric environment in the NMR tube.

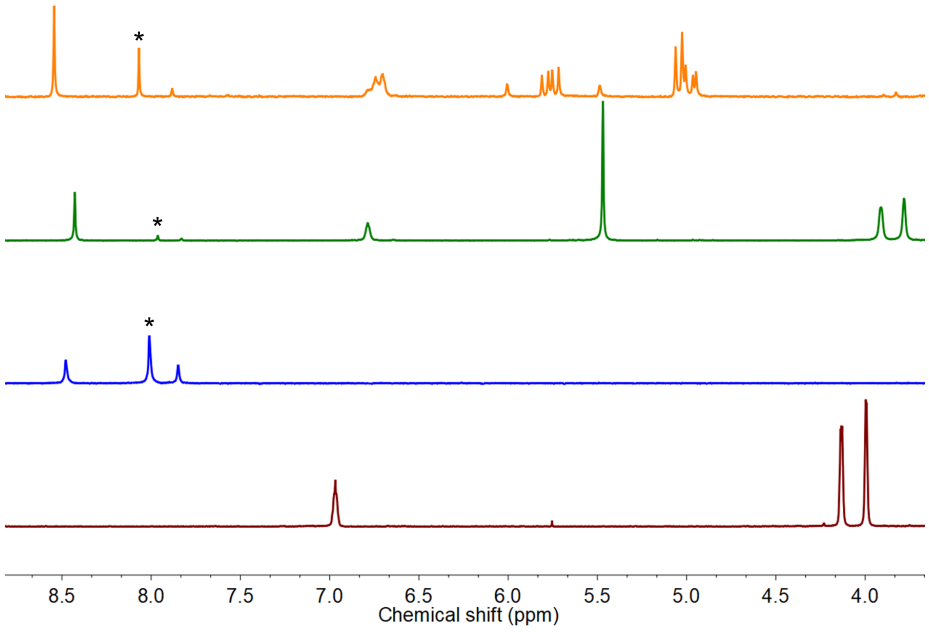

Figure 3.14: ^{1}H NMR Spectrum of MOF-808 (Blue), MOF-808-BS (Green), MOF-808-BD (Orange) and 3-Sulfolene-3-Carboxylic Acid (Wine). DMF Peaks Were Indicated with * on Top.

BET surface areas of MOF-808 and its derivatives were also measured by a Tri-Star II PLUS surface area and porosity analyzer. The results are shown in Figure 3.15. MOF-808 has a gas uptake of 440 cm^3/g and a BET SA of 1700 m^2/g. For the SALI derivatives, we expect to see a lower gas uptake as the incorporated ligand will deprive some space within the pore, which also increasing the molecular weight of the MOF. MOF-808-BS and MOF-808-BD (Figure 3.15) yield a total gas uptake of 285 and 197 cm^3/g, respectively. The BET SA of MOF-808-BS and MOF-808-BD are 750 and 1100 m^2/g, respectively. The trend is consistent with the size of ligands; a larger ligand leads to a lower total gas uptake.

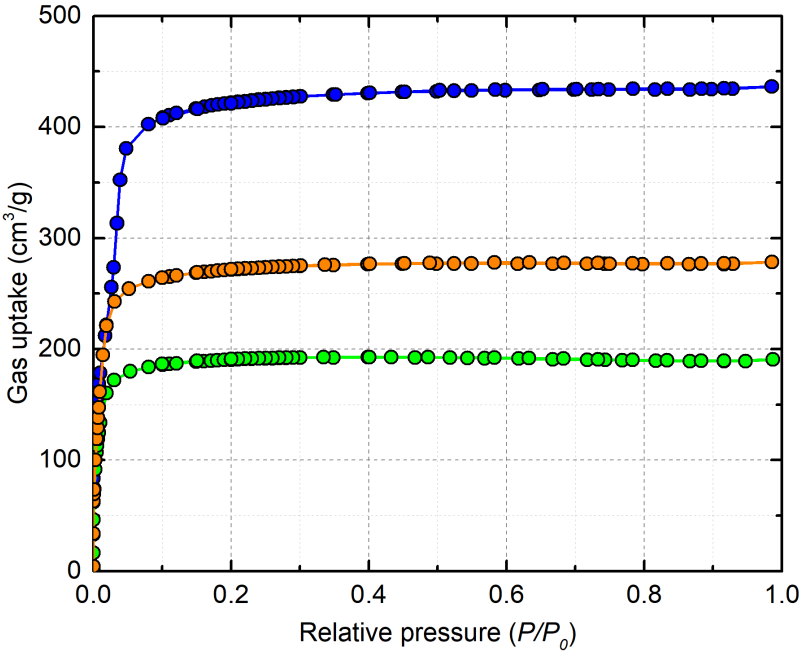

Figure 3.15: Nitrogen Gas Adsorption Isotherms of MOF-808 (Blue), MOF-808-BS (Green) and MOF-808-BD (Orange) Measured at 77 K.

With the structure and ligand incorporation confirmed for MOF-808 and its derivatives, we measured the sulfur dioxide micro-breakthrough of these MOFs. The sulfur dioxide microporous breakthrough and desorption results are illustrated in Figure 3.16 and Table 3.2. To our surprise, based on the dynamic loading calculated from the data, MOF-808, had the highest loading of sulfur dioxide (0.53 mol/kg). This value is nearly twice as high as the butadiene-containing MOF-808-BD, and more than five times higher than the sulfolene-containing MOF-808-BS.

The difference among these three MOFs can be explained by the hypothesis of node reactivity. With SALI-unfunctionalized MOF-808, sulfur dioxide will likely react/interact with the terminal waters and hydroxides on the node (Figure 3.17) to form sulfuric acid groups coordinated to the node. If the terminal water was replaced

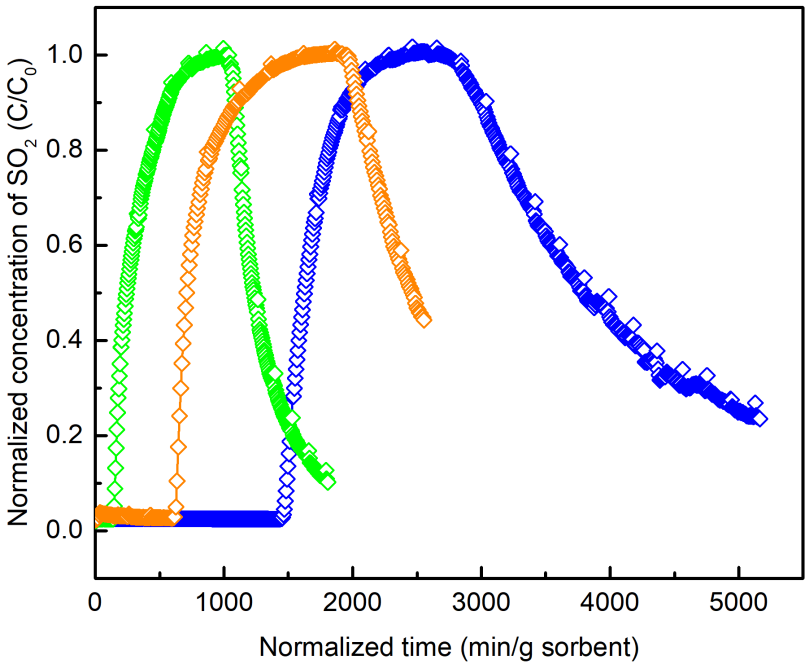

Figure 3.16: Sulfur Dioxide Micro-Breakthrough and Desorption Curves Under Dry Condition for MOF-808 (Blue), MOF-808-BS (Green), and MOF-808-BD (Orange).

Table 3.2: Dynamic Loading of Sulfur Dioxide on MOF-808, MOF-808-BS and MOF-808-BD.

	Sorbent mass (mg)	Effective loading (mol/kg)
MOF-808	15.1	0.53
MOF-808-BS	21.6	0.10
MOF-808-BD	11.4	0.25

by butadiene-carboxylate, then sulfur dioxide will react with butadiene to potentially form a butadiene sulfone; alternatively, it may only interact with the butadiene in a way similar to that seen with UiO-66-MA. However, when butadiene sulfone is installed into MOF-808, then there is no reactivity. We hypothesize that this occurs

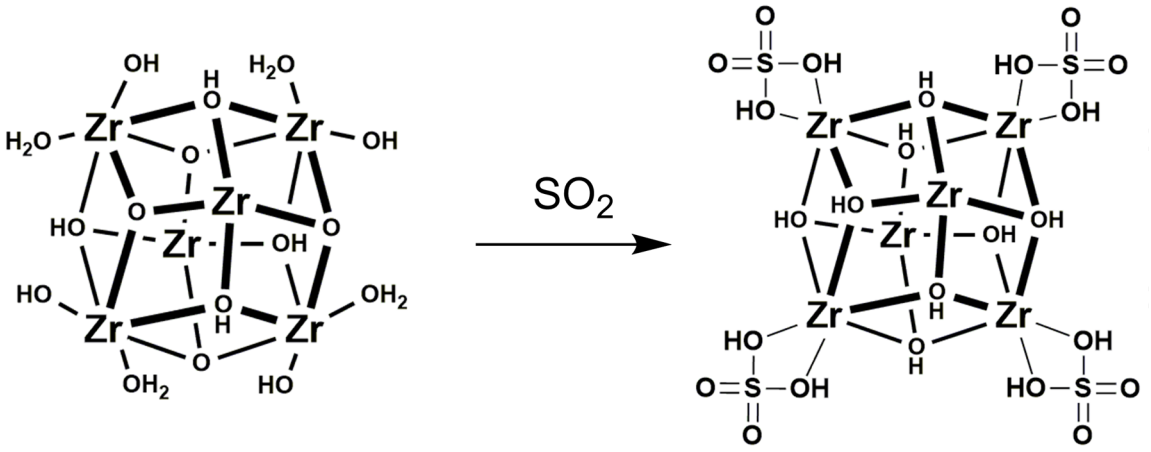

Figure 3.17: Hypothesis Showing How MOF-808 May Interact with Sulfur Dioxide.

because neither a diene-containing linker nor an unfunctionalized node (Figure 3.17 left) is present to interact/react with sulfur dioxide.

Unfortunately, the above mode of action is merely a hypothesis. In order to better understand how sulfur dioxide interacts with these MOF-808 derivatives, FT-IR and NMR studies are required, as had been done for UiO-66 and UiO-66-MA. However, as the measurements were performed at the United States Army test lab, we were unable to get the necessary NMR and IR data of these samples from them and they were unable to send the samples back (see Chapter 4 for future directions) in time for the completion of this thesis.

3.2.3 Other Attempted: *De Novo* Synthesis of MOFs Toward Sulfur Dioxide Sequestration.

Along the way, a few other linkers were also made which we did not feel were good candidates for sulfur dioxide sequestration. For example, IRMOF-10 (Figure 3.5)

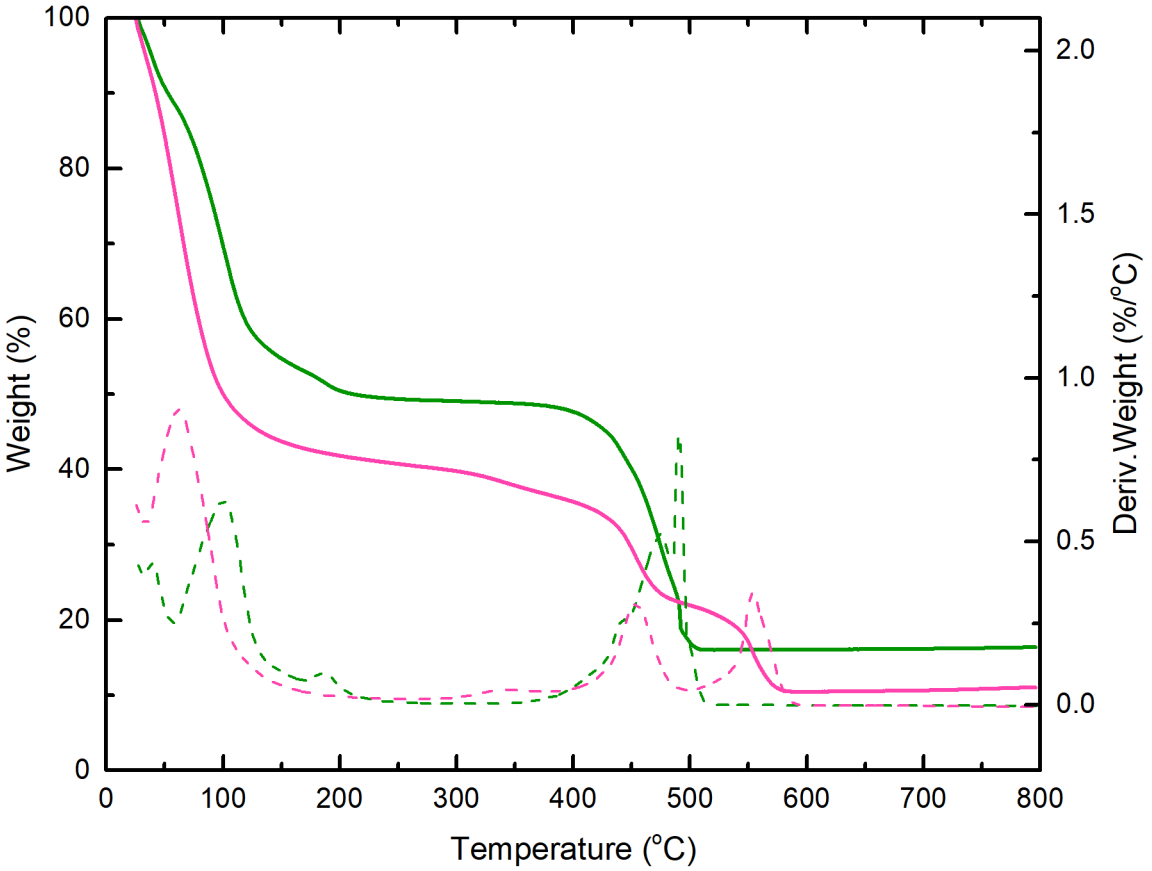

Figure 3.18: Weight Loss (Solid Line) and Derivative Weight Loss (Dash Line), TGA of IRMOF-10 (Green) and IRMOF-10-BS (Pink).

could be easily formed and we were trying to synthesize IRMOF-10-BD (butadiene) via the thermal decomposition of the parent IRMOF-10-BS (butadiene sulfone). However, as shown in Figure 3.18, the thermal stability of IRMOF-10-BS was such that the whole MOF decomposed around the same temperature as the sulfur dioxide was released from the linker to form the desired butadiene. The calculated mass loss for sulfur dioxide release is 2.16 %, which is similar to the percentage of 2.30 % measured by TGA between 300 and 400 °C. Given this, sulfur dioxide adsorption and breakthrough experiments were not performed.

3.3 Conclusions

Two series of metal-organic frameworks, named UiO-66 series and MOF-808 series, respectively, were synthesized and applied as adsorbents for sulfur dioxide adsorption *via* fixed bed micro-breakthrough measurements. For UiO-66 and UiO-66-MA, we compared the ability of these MOFs to adsorb sulfur dioxide under dynamic conditions to determine if a cheletropic reaction between sulfur dioxide and muconic acid was possible. A nearly 3-fold increase in sulfur dioxide adsorption was observed for the MOF possessing muconic acid over the muconic acid-free MOF. Despite the improved uptake, however, there was no indication of a chemical reaction happened between the two species. Instead, sulfur dioxide preferred to interact with the MOF *via* physisorption. The underlying mechanism of adsorption will need to be further examined.

As for the MOF-808 series, surprisingly, MOF-808 was able to absorb more than two times the sulfur dioxide when compared to the butadiene-containing MOF, and five times higher than the butadiene sulfone MOF. Given the fact that traditional activated carbon has even lower effective loading relative to UiO-66, UiO-66-MA, and MOF-808, these adsorbents are promising for sulfur dioxide removal. Additionally, all the experiments were carried out at ambient temperature, only physical adsorption was observed in UiO-66-MA (and possibly some of the MOF-808 derivatives). If variable temperature breakthrough measurements could be applied here, we may be able to observe a transition between physical and chemical adsorptions.

3.4 Experimental Details

3.4.1 General Procedures, Materials, and Instrumentation

All compounds and solvents were used as received unless otherwise noticed: 1,8-diazabicyclo(5.4.0)undec-7-ene (Aldrich, 98 %), 2,3-dibromopropionic acid (Aldrich, 98 %), acetic acid (ACP, 99.7 %), acetone (ACP, 99.5 %), acetonitrile (ACP, 99.5 %), biphenyl-4,4'-dicarboxylic acid (Aldrich, 97 %), butadiene sulfone (Aldrich, 98 %), chloroform (ACP, 99.8 %), dichloromethane (ACP, 99 %), dimethyl biphenyl-4,4'-dicarboxylate (Aldrich, 99 %), deuterated dimethyl sulfoxide (DMSO-d_6) (Cambridge, 99.5 %), deuterated sulfuric acid (D_2SO_4/D_2O) (Aldrich, 99.5 atom % D), ethyl acetate (Fisher, 99 %), ethyl alcohol (Aldrich, denatured), ethyl alcohol (ACP, 95 %), formic acid (BDH, 90 %), hexanes (Fisher, 99.9 %), hydrochloride acid (Caledon, 37 %), magnesium sulfate (ACP, 98 %), methanol (ACP, 99.8 %), *N,N*-dimethylformamide (DMF; Fisher, 99.9 %), nitric acid (Anachemia, 70 %), palladium(II) acetate (Aldrich, 97 %), palladium on activated carbon (Aldrich, 10 wt %), piperazine (Aldrich, 99 %), potassium hydroxide (ACP, 85 %), sodium nitrite (Aldrich, 99.5 %), sodium chloride (ACP, 99 %), sodium tetrafluoroborate (Aldrich, 98 %), sulfuric acid (Caledon, 98 %), terephthalic acid (Aldrich, 98 %), toluene (Fisher, 99.9 %), *trans,trans*-muconic acid (Aldrich, 98 %), triethylamine (Aldrich, 99 %), trimesic acid (Aldrich, 95 %), zinc(II) nitrate hexahydrate (J.T. Baker, 99 %), zirconium(IV) chloride (Aldrich, 99.5 %), zirconium(IV) oxychloride octahydrate (Aldrich, 99.5 %).

Powder X-ray diffraction (PXRD) patterns were obtained using a Rigaku X-ray Ultima IV Diffractometer equipped with a copper X-ray source and a scintillation

counter detector.

Nitrogen gas adsorption isotherm data were collected at 77 K on a TriStar II PLUS surface area and porosity analyzer. All the samples were activated before each isotherm by heating the samples in a vacuum oven at 80 °C.

^{1}H NMR experiments were performed on a 300 MHz Bruker Avance III 300 instrument. Samples were digested in D_2SO_4/DMSO-d_6 mix solution and filtered before measured by Bruker Avance III.

Thermogravimetric analysis (TGA) experiments were performed on a TA Instruments Q500 interfaced with a PC using TA Instruments software (version 4.7A). Samples were placed in a platinum pan and heated at a rate of 10 °C/min from 25 to 800 °C under a nitrogen atmosphere.

Attenuated total reflection Fourier-transform infrared spectroscopy (ATR-FT-IR) experiments were carried out by a Bruker Tensor 27 FT-IR with a Bruker Platinum ATR accessory equipped with a single reflection diamond crystal. Samples were measured between 4000 and 400 cm^{-1} with a resolution of 4 cm^{-1}. The final spectra was the average of 16 scans.

3.4.2 Microporous Breakthrough Reaction System

All the microporous breakthrough testing apparatus and the theory used here were previously reported.[85] Our collaborator Dr. Jared DeCoste of the Edgewood Chemical Biological Center performed all the measurements under the conditions shown in Table 3.3.

The custom-built instrument has a testing bed with an approximately 4 mm height

Table 3.3: Parameters for Micro-Breakthrough Experiments.

Parameters	Values
Gas	Sulfur dioxide
Challenge concentration (mg/m^3)	1000
Temperature (°C)	20
Relative humidity (%)	0
Bed height (mm)	4
Bed volume (mm^3)	50
Flow rate (mL/min) at 20 °C	20
Residence time (s)	0.15
Detector	GC/FPD

and 4 mm internal diameter. The gas flow rate was kept at 20 mL/min and the final gas mixture was analyzed by gas chromatography with flame photometric detection.

3.4.3 Synthesis of MOFs

Both UiO-66[23] and MOF-808[124] were synthesized following the literature routes with only minor changes (see below).[67]

(a) IRMOF-10: 57.7 mg (0.194 mmol) zinc(II) nitrate hexahydrate and 16.7 mg (0.069 mmol) biphenyl-4,4'-dicarboxylic acid were dissolved in 5.0 mL DMF in a 2 dram vial by sonication, a colourless solution was formed before being heated at 100 °C for 24 h. The reaction produced colourless crystals were collected by filtration and washed with anhydrous DMF (3 × 10.0 mL) and anhydrous DCM (3 × 10.0 mL),

respectively. The sample was dried in a fume-hood at ambient temperature.

(b) UiO-66: A 25 mL vial was charged with zirconium(IV) chloride (123.3 mg, 0.529 mmol), DMF (5.0 mL), hydrochloric acid (1.0 mL). Once dissolved, with 15 mins sonication, terephthalic acid (123.8 mg, 0.745 mmol) as well as extra 10.0 mL DMF was added to the previous mixture and sonicated for an additional 15 mins. The solution was placed in an oven at 80 °C for 12 h. The resulting off-white solid was washed with 3 × 10.0 mL of DMF and subsequently 3 × 10.0 mL of ethanol. After filtration, the sample was dried under a vacuum for 12 h at 80 °C.

(c) MOF-808: A 50 mL vial was charged with trimesic acid (110.0 mg, 0.500 mmol), zirconium oxychloride octahydrate (160.0 mg, 0.500 mmol), DMF (20.0 mL) and formic acid (20.0 mL). Once dissolved by sonication, the solution was put in an oven at 100 °C for 7 days. The resulting white crystalline material was washed with 3 × 10.0 mL DMF. After filtration, the sample was dried under a vacuum for 17 h at 100 °C.

3.4.4 Ligand Synthesis

3.4.4.1 1,3-Butadiene-2-Carboxylic Acid

The synthesis was carried out according to literature precedence that was first published by Collard and co-workers in 2003.[199] Herein, with minor changes from the original work, 1,3-Butadiene-2-carboxylic acid was synthesized using the following steps (Figure 3.19). Butadiene sulfone (1.196 g, 0.010 mol) was dissolved in a nominally dry DMSO (4.0 mL) solution *via* stirring in a 50 mL, 3-neck, round bottom flask before carbon dioxide gas was bubbled into the system. DBU (3.0 mL) was added

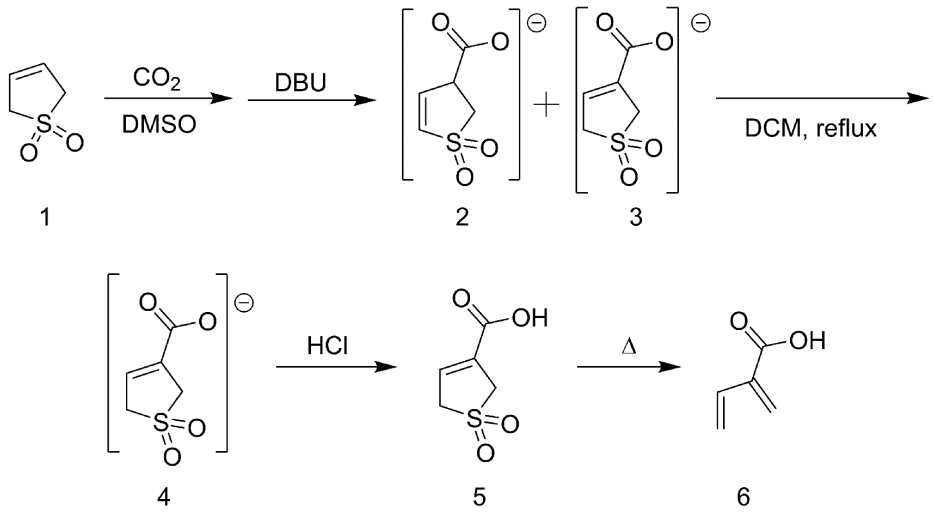

Figure 3.19: Scheme of 1,3-Butadiene-2-Carboxylic Acid Synthesis.

dropwisely to the previous solution. The reaction flask was allowed to react for 2 days while stirring. Afterwards, the reaction was diluted with acetone and an off-white precipitate was formed. The solid was filtered and then dissolved in dichloromethane (100.0 mL) in a 150 mL, 2-neck, round bottom flask at ambient temperature. Subsequently, dry HCl gas was bubbled in, the yellowish white precipitate **5** (0.500 g, 0.003 mol) was formed with a yield of 45 % and collected by filtration.

^{1}H NMR (300 MHz, DMSO-d_6) δ 6.97 (td, J = 3.2, 1.6 Hz, 1H), 4.14 (dt, J = 3.2, 1.6 Hz, 2H), 4.00 (d, J = 5.2 Hz, 2H).

Dry HCl gas was formed by dripping concentrated sulfuric acid into the solution of sodium chloride and hydrochloric acid. The liberated, wet HCl gas was then bubbled through a smaller quantity of sulfuric acid to remove any trace of water vapor.

6 was not synthesized directly from **5**. It was formed by thermally treatment of MOF-808-BS at 160 °C for 1 h, then MOF-808-BD was formed.

3.4.4.2 2-Butadiene Sulfone-Biphenyl-4,4'-Dicarboxylic Acid

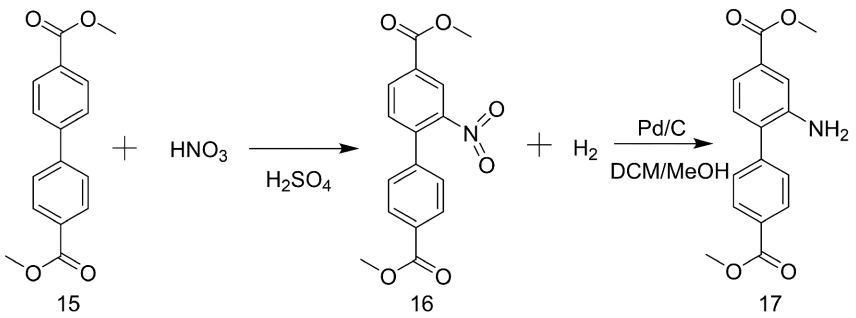

Figure 3.20: Scheme of 2-Amino-Dimethyl Biphenyl-4,4'-Dicarboxylate Synthesis.

The organic ligand was synthesized with the route reported by the literature with minor changes.[212–214] 5.0 mL concentrated sulfuric acid was charged in a 15 mL round bottom flask while stirring and cooled down to 0–5 °C. Afterwards, 0.501 g (1.850 mmol) dimethyl biphenyl-4,4'-dicarboxylate was added. Once dissolved, a solution of nitric acid:sulfuric acid (125 μL:1000 μL) was added dropwisely. The solution was stirred for 40 min before being poured onto an ice/water mixture. The solid was filtered to collect the product **16**, with a 92 % yield (0.537 g).

^{1}H NMR (300 MHz, Chloroform-*d*) δ 8.56 (d, J = 1.7 Hz, 1H), 8.30 (dd, J = 8.0, 1.7 Hz, 1H), 8.18 – 8.07 (m, 2H), 7.54 (d, J = 8.0 Hz, 1H), 7.46 – 7.35 (m, 2H), 3.98 (d, J = 15.5 Hz, 6H).

0.500 g (1.586 mmol) **16** was hydrogenated by hydrogen balloons with the help of 0.200 g 10 wt % Pd/C catalyst dispersed in DCM/MeOH (v/v=8.5 mL/8.5 mL) to form 0.258 g (0.904 mmol) 2-amino-dimethyl biphenyl-4,4'-dicarboxylate (**17**) after 18 h stirring at ambient temperature, as shown in Figure 3.20, with a yield of 57 %.

^{1}H NMR (300 MHz, Chloroform-*d*) δ 8.17 – 8.10 (m, 2H), 7.58 – 7.53 (m, 2H),

7.52 – 7.43 (m, 2H), 7.18 (d, J = 7.8 Hz, 1H), 3.94 (d, J = 10.1 Hz, 6H).

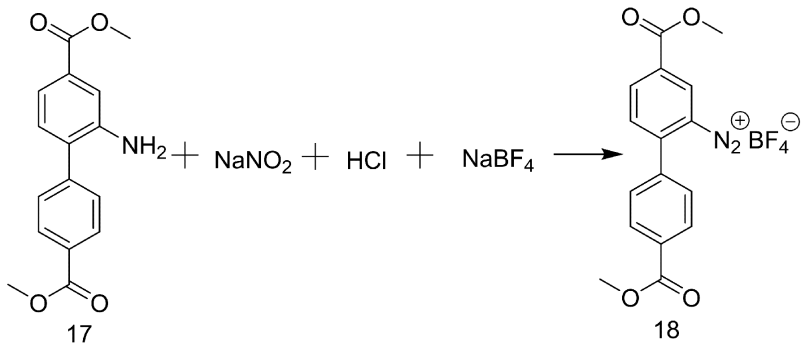

Figure 3.21: Scheme of Dimethyl Biphenyl-4,4'-Dicarboxylate, 2-Diazonium Tetrafluoroborate Synthesis.

Compound **18** was synthesized following the literature reported route with minor changes.[212] As shown in Figure 3.21, 0.485 g (1.698 mmol) 2-amino-dimethyl biphenyl-4,4'-dicarboxylate was dissolved in 3.0 mL 15 % HCl solution at 0–4 °C and a solution of 0.782 g (11.335 mmol) sodium nitrite in 1.0 mL water was added dropwisely with vigorous stirring for 10 min. Then 2.272 g (20.694 mmol) sodium tetrafluoroborate in 5.0 mL water was added dropwisely to the previous mixture. The solution was stirred for an additional 60 min. The solution was filtered and washed with 20.0 mL of water and ethanol, respectively. The diazonium salt, **18**, was collected and characterized by ^{1}H NMR, with a yield of 82 % (0.534 g).

^{1}H NMR (300 MHz, DMSO-d_6) δ 9.59 (d, J = 1.7 Hz, 1H), 8.76 (dd, J = 8.2, 1.8 Hz, 1H), 8.29 – 8.20 (m, 3H), 8.10 – 8.04 (m, 2H), 3.97 (d, J = 22.1 Hz, 6H).

Compound **21**, 2-Butadiene sulfone-dimethyl biphenyl-4,4'-dicarboxylic acid, was synthesized by the reported method with minor changes (Figure 3.22).[213] 1.030 g (2.682 mmol) as-synthesized compound **18**, 1.020 g (8.633 mmol) butadiene sulfone

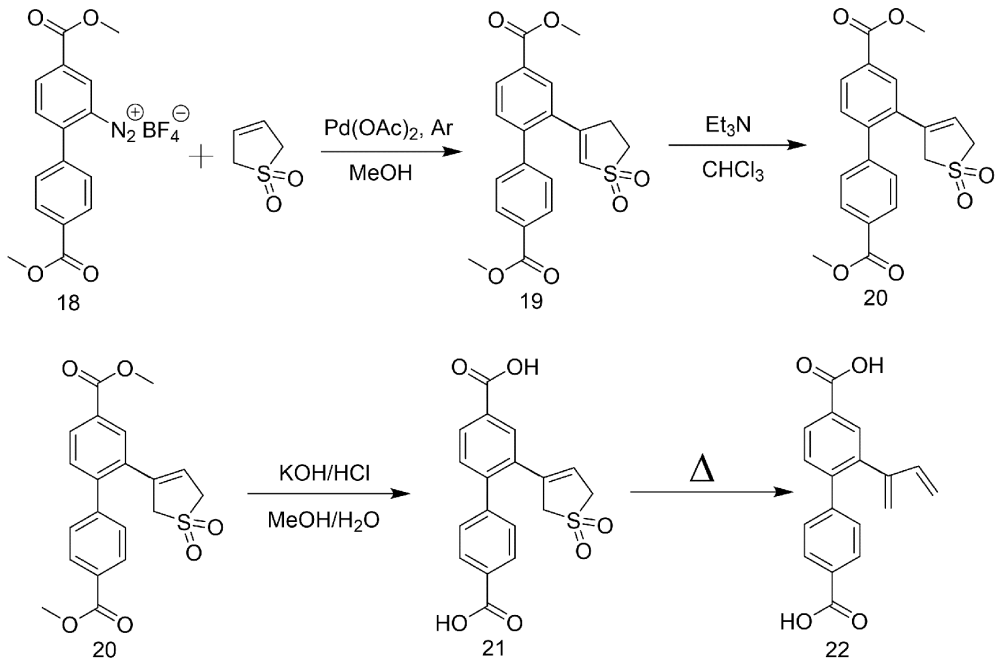

Figure 3.22: Scheme of 2-Butadiene-Dimethyl Biphenyl-4,4'-Dicarboxylic Acid Synthesis.

and 0.170 g (4.454 mmol) palladium(II) acetate were charged in a 50 mL round bottom flask with 40.0 mL methanol under argon atmosphere. Yellow precipitate was formed while stirring. The reaction was maintained at 50 °C for 1 h. At this time, the release of nitrogen gas from the reaction mixture had greatly decreased. After filtration, the precipitate was subsequently dissolved in a mixture of 50.0 mL chloroform and 6.0 mL triethylamine in a 100 mL round bottom flask. The reaction was maintained at 60 °C overnight, filtered and the solution was removed by rotary evaporation. The residue was purified by a silica gel column using hexane/ethyl acetate (v/v=1/2). 0.220 g colourless crystalline **20** was collected and characterized by ^{1}H NMR with a yield of 20 %.

^{1}H NMR (300 MHz, Chloroform-d) δ 8.20 – 8.02 (m, 4H), 7.44 (ddt, J = 8.4, 3.8,

1.1 Hz, 3H), 6.15 – 6.05 (m, 1H), 3.96 (d, J = 3.8 Hz, 6H), 3.88 (dt, J = 3.1, 1.5 Hz, 2H), 3.44 (q, J = 1.6 Hz, 2H).

To form **21**, 0.200 g (0.498 mmol) **20** and 7.5 mL of 2 M potassium hydroxide were dissolved in a mixture of methanol/water (20.0 mL/20.0 mL) at 70 °C while stirring. After 24 h, the mixture was cooled to ambient temperature before concentrated hydrochloric acid was added. Light yellow precipitate was formed immediately. The solid was filtered yielding 0.130 g (0.349 mmol) of compound **21** with a 70 % yield.

^{1}H NMR (300 MHz, DMSO-d_6) δ 8.11 – 7.96 (m, 4H), 7.63 – 7.47 (m, 3H), 6.10 (dd, J = 5.1, 4.6 Hz, 1H), 3.97 – 3.91 (m, 2H), 3.63 (d, J = 1.9 Hz, 2H).

Compound **21** was heated at about 220 °C to form compound **22**, the temperature was determined by thermogravimetric analysis of compound **21**.

3.4.5 Ligands Incorporation into MOFs

As demonstrated above, there are three identical ways to incorporate the ligand with unique functional groups into MOFs, as listed below.

3.4.5.1 *De Novo* Synthesis

Ligand **21** was incorporated into parent MOF, IRMOF-10,[27] *via* the *de novo* method.

IRMOF-10-BS (butadiene sulfone): 22.3 mg (0.060 mmol) 2-Butadiene sulfone-dimethyl biphenyl-4,4'-dicarboxylic acid (**21**) and 53.4 mg (0.181 mmol) zinc(II) nitrate hexahydrate were dissolved in 5.0 mL DMF in a 2-dram vial *via* sonication to form a colourless solution. After being heated in a 100 °C oven for 24 h, large cubic yellow crystals were collected after washing with anhydrous DMF (3 × 10.0 mL) and anhydrous DCM (3 × 10.0 mL), respectively.

3.4.5.2 Post Synthetic Exchange

UiO-66-MA[201] was synthesized as previous reported with minor changes.

UiO-66-MA: 106.6 mg (0.750 mmol) *trans,trans*-muconic acid was dissolved in 8.0 mL, 4 % KOH *via* sonication before being neutralized by a small amount of 1 M HCl. Subsequently, 150.0 mg (0.750 mmol) UiO-66 was added to the previous solution, and stirred until mixed evenly. The mixture was heated to 85 °C in an oven for 5 days. The resulting solid was washed first with 3 × 10.0 mL of methanol. The solvent was then decanted and replaced with methanol daily for 3 days. After filtration, the sample was dried under vacuum for 8 h at 60 °C, yielding a light earthy yellow solid product.

3.4.5.3 Solvent Assistant Ligand Incorporation (SALI)

MOF-808-SALI series were made by solvent assistant ligand incorporation (SALI), with different ligands incorporated into the parent MOF, MOF-808. The ligands are shown below in Figure 3.23.

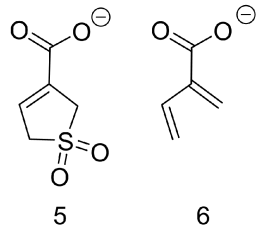

Figure 3.23: Ligands Incorporated into MOF-808

The as-synthesized MOF-808 was treated to disconnect terminal water molecules initially occupying six coordination sites by heating in vaccum oven first at ambient

temperature for 24 h then 150 °C for another 24 h.

(a) MOF-808-BS: 85.3 mg 3-butadiene sulfone-3-carboxylic acid (**5**) was dissolved in 5.0 mL methanol in a 2-dram vial by sonication before 46.3 mg MOF-808 was added. The mixture was allowed to form a heterogeneous mixture before being transferred to a 60 °C oven for 36 h. The material was subsequently washed with 3 × 15.0 mL of acetone and soaked for one day. Afterwards, the acetone was replaced with acetonitrile for the following two days then dichloromethane for an additional two days. The sample was filtered and dried at ambient temperature overnight. The product was subsequently observed to be a white crystalline powder.

(b) MOF-808-BD: MOF-808-BS was heated at 160 °C in the solid state for 1 h, yielding a yellow powder product.

Chapter 4

Future Work

A project is never done. The ideas which started me off on my thesis have grown to more than what I could achieve in the limited time that my degree has allowed me. Due to this, I believe that there are several future avenues for incoming students to work on.

4.1 Future Work for MOF Synthesis *via* Alternative Solvents

As shown before, Cyrene can be successfully used for MOF synthesis. The MOF structures made with Cyrene are identical to the ones made with DMF. Perhaps even more impressive was the observation that the gas adsorption isotherm for HKUST-1 was better when Cyrene was used to form the MOF *vs.* DMF. However, the surface areas of the other four MOFs were less than ideal. Although we were able to learn a lot about what was occurring during the formation of the MOF, I believe that there

would be real progress if the surface areas of these four MOFs could be optimized to match, or exceed, their DMF counterparts by eliminating the influence of trapped Cyrene and related chemicals in the pores.

4.2 Future Work of MOFs Used for Sulfur Dioxide Gas Adsorption

As demonstrated in this thesis as well as the primary literature, MOFs are porous materials that have applications in the field of gas adsorption and separation. In Chapter 3, we present how three families of MOFs and their derivatives can be used for sulfur dioxide adsorption and sequestration. The data and results uncovered that, at ambient temperature, butadiene may not be able to react with sulfur dioxide through a cheletropic reaction. However, this work has yielded some future directions which I feel could yield a deeper understanding of how sulfur dioxide reacts within MOFs.

4.2.1 MOF-808 and Its Derivatives in Sulfur Dioxide Removal

As a 6-coordinated MOF, MOF-808 has at most 6 terminal water and 6 terminal hydroxide groups coordinated to zirconium cluster when zero BTC linker is missing. It has been shown in Chapter 3 that the node interacts with sulfur dioxide, potentially forming a coordinated sulfate group. However, this is not well explored. To that end, I believe that a reasonable avenue of research would be to probe the adsorption

and desorption of the water/hydroxyl-terminated zirconium cluster in comparison with a benzoic acid-capped zirconium cluster, which can be installed *via* SALI. This will determine the nature of the interaction (*i.e.*, chemisorption *vs.* physisorption), which, in tern, will uncover whether MOF-808 can be widely applied as a sulfur dioxide adsorbent. A combination of IR, ideally in-situ under gas-loading/unloading conditions, solid-state NMR, and TGA analysis will help determine how sulfur dioxide is interacting with the MOF. Additionally, one area where this system could be very interesting is in proton conduction systems. If a sulfate/sulfuric acid moiety is formed during the reaction of sulfur dioxide with MOF-808, then the proton mobility of the MOF will greatly change. As such, the MOF may have features as a conductivity sensor for sulfur dioxide.

In addition to this work, I believe that there are some additional ligands that can be installed *via* SALI which could lead to some new avenues for sulfur dioxide sequestration. For example, as shown in Figure 4.1, sulfur dioxide can react with DABCO to form a stable white powder product DABSO.[215] If DABCO could be synthesized in reasonable yield with a carboxylic acid tether, then incorporation of the linker into MOF-808 *via* SALI would be an interesting avenue to explore.

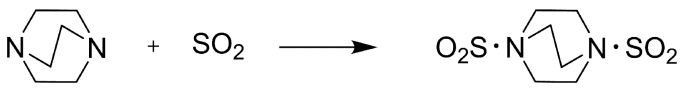

Figure 4.1: Scheme of Reaction Between DABCO and Sulfur Dioxide.

To that end, towards the end of my degree, I was able to synthesize a series of four MOF-808 derivatives. These MOFs have the following linkers incorporated

on the node, namely MOF-808-BA (**22**), MOF-808-BS (**5**), MOF-808-BD (**6**), and MOF-808-DABCO (**14**) shown in Figure 4.2. Due to time constraint, these MOFs, as well as their sulfur dioxide adsorption, were not well examined.

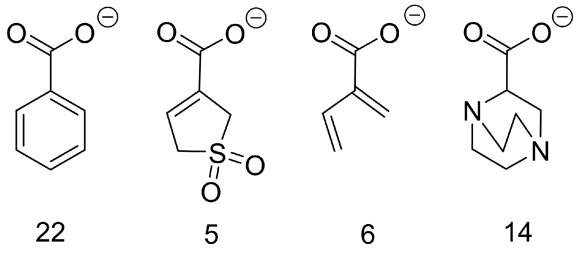

Figure 4.2: Variable Ligands Incorporated into MOF-808.

MOF-808 and its derivatives were synthesized by the methods used in Chapter 3 except MOF-808-BA, which was synthesized by soaking MOF-808 in saturated sodium benzoate solution for three days. The PXRD of these MOFs were shown in Figure 4.3; all the diffraction peaks can be well indexed to the simulated crystalline MOF-808. There is an additional peak in MOF-808-BS (green trace) at low-angle which cannot be identified at this stage. However, neglecting this anomaly, the data suggests that the MOF-808 framework topology was not modified by the SALI process.

With the synthesis of these MOFs already determined, I believe that future work should focus more on characterization of the sulfur dioxide adsorption kinetics.

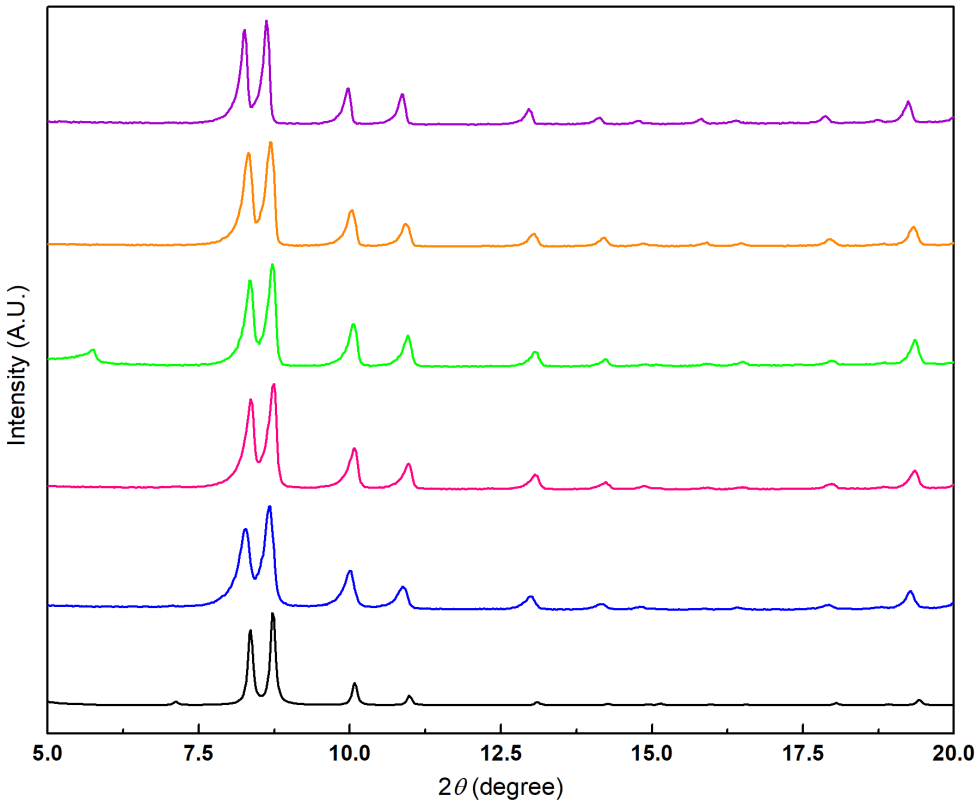

Figure 4.3: The PXRD Patterns of Simulated MOF-808 (Black), Unfunctionalized MOF-808 (Blue), MOF-808-BA (Pink), MOF-808-BS (Green), MOF-808-BD (Orange), and MOF-808-DABCO (Purple).

4.2.2 IRMOF-10 and Butadiene-Functionalized IRMOF-10 Investigated for Sulfur Dioxide Removal

IRMOF-10 and IRMOF-10-BS were synthesized *via* the *de novo* solvothermal method in Chapter 3. However, further work needs to be done on synthesis of IRMOF-10-BD. From a gravimetric standpoint, if IRMOF-10-BD could be formed, then this MOF would offer an increased amount of sulfur dioxide adsorbed based on the fact that zinc(II) cation nodes were applied instead of $[Zr_6O_4(OH)_4]^{12+}$ clusters.

4.2.3 VT Microporous Breakthrough Measurements

As demonstrated, UiO-66-MA only shows physical adsorption at ambient temperature. If variable temperature (VT) microporous breakthrough measurements were carried out, chemical adsorption would yield an increase in sulfur dioxide adsorption. Although this did not occur for UiO-66-MA, it is possible that at a higher temperature, the kinetic barrier to undergoing the cheletropic reaction could be overcome. As such, I believe that future work should focus on understanding the role that temperature has on these reactions.

4.2.4 Other Toxic Gases

In chapter 3, MOFs acted as the sorbent for sulfur dioxide removal and much better results were gained for MOFs than conventional porous materials such as activated carbon. With this success in mind, I believe that the scope of the tested analytes should be increased. Preliminary data from our colleague in the United States Army examined UiO-66, UiO-66-MA, MOF-808, MOF-808-BS, and MOF-808-BD to ammonia, chlorine, cyanogen chloride and hydrogen sulfide. With variable challenge concentrations, the series measurements were carried out under the conditions shown in Table 4.1.

The ability for UiO-66 and UiO-66-MA to absorb other TICs such as ammonia, chlorine, cyanogen chloride, and hydrogen sulfide are illustrated below in Figure 4.4. As we see here, the sorption behaviors of chlorine, cyanogen chloride and hydrogen sulfide are mostly the same for these two MOFs. There are some notable differences between the adsorption curve of cyanogen chloride and the desorption of hydrogen

Table 4.1: Parameters of the Fixed Bed Micro-Breakthrough Measurement

Parameters	Values			
Gas	Ammonia	Chlorine	Cyanogen chloride	Hydrogen sulfide
Challenge concentration (mg/m^3)	1000	2000	4000	1000
Temperature (°C)	20			
Relative humidity (%)	0			
Bed height (mm)	4			
Bed volume (mm^3)	50			
Flow rate (mL/min) at 20 °C	20			
Residence time (s)	20			
Detector	GC/PID	GC/PID	GC/FID	GC/FID

sulfide. Furthermore, with regard to the total gas uptake, only ammonia shows a moderate storage under dynamic conditions. Given this, however, these MOFs could be featured in separation of sulfur dioxide from these gases *via* pressure swing adsorption.

Thus, future work should focus on studying the selectivity between sulfur dioxide and these other TICs behaves.

Moreover, the chlorine microporous breakthrough and desorption for MOF-808, MOF-808-BS and MOF-808-BD are shown in Figure 4.5. The curves here have an opposite trend to sulfur dioxide shown in Chapter 3. The chlorine concentration detected by GC reached the challenge concentration quickly in MOF-808 while for

MOF-808-BD, there was a nearly 1000 min/g of MOF before the onsent of breakthrough occurred. Perhaps even more interesting is that the desorption curves look nearly identical for all 3 MOFs suggesting that the amount of gas that could desorb from the MOFs are similar despite the significant amount of gas that was absorbed prior to breakthrough for MOM-808-BD. Future work should focus on studying how the chlorine gas interacts with the MOF. It is likely, but unproven that the chlorine

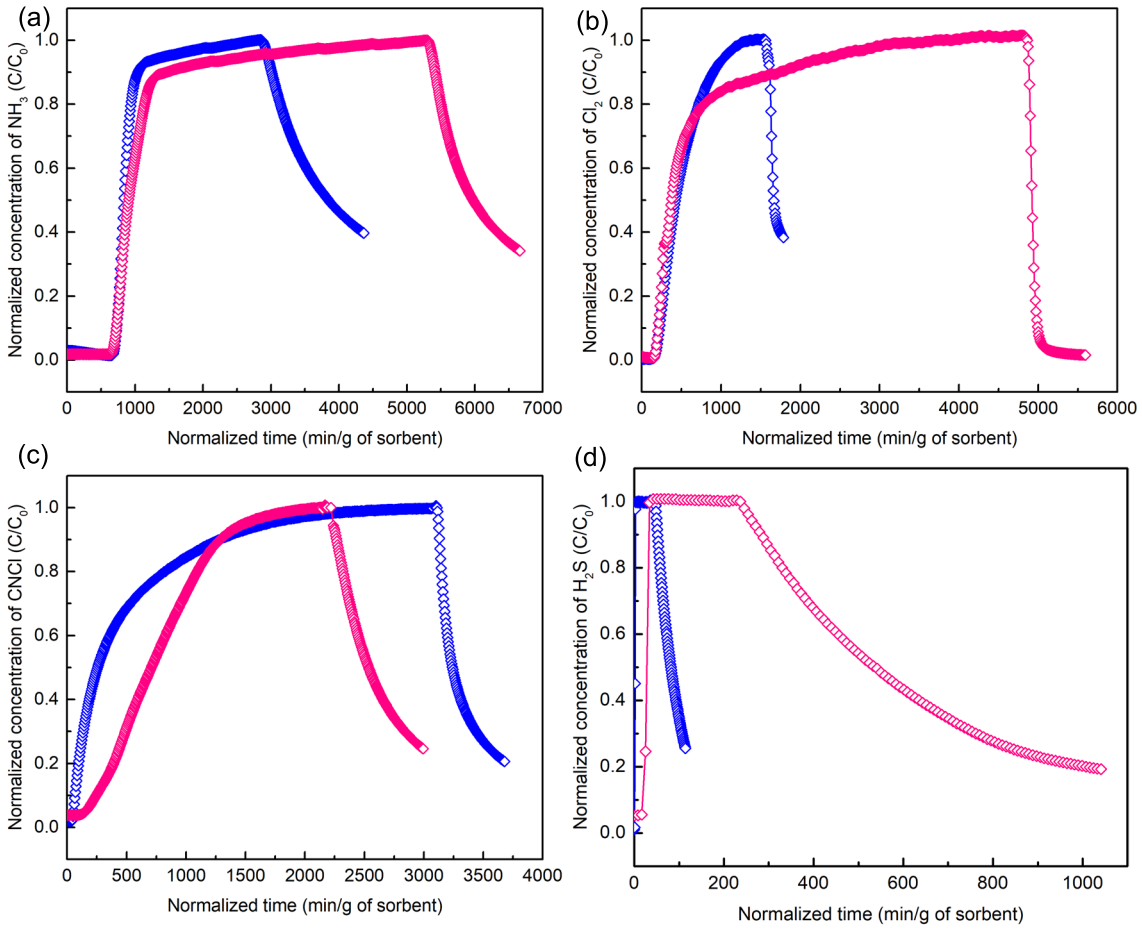

Figure 4.4: (a) Ammonia, (b) Chlorine, (c) Cyanogen Chloride, and (d) Hydrogen Sulfide Micro-Breakthrough and Desorption Curves Under Dry Condition for UiO-66 (Blue) and UiO-66-MA (Pink).

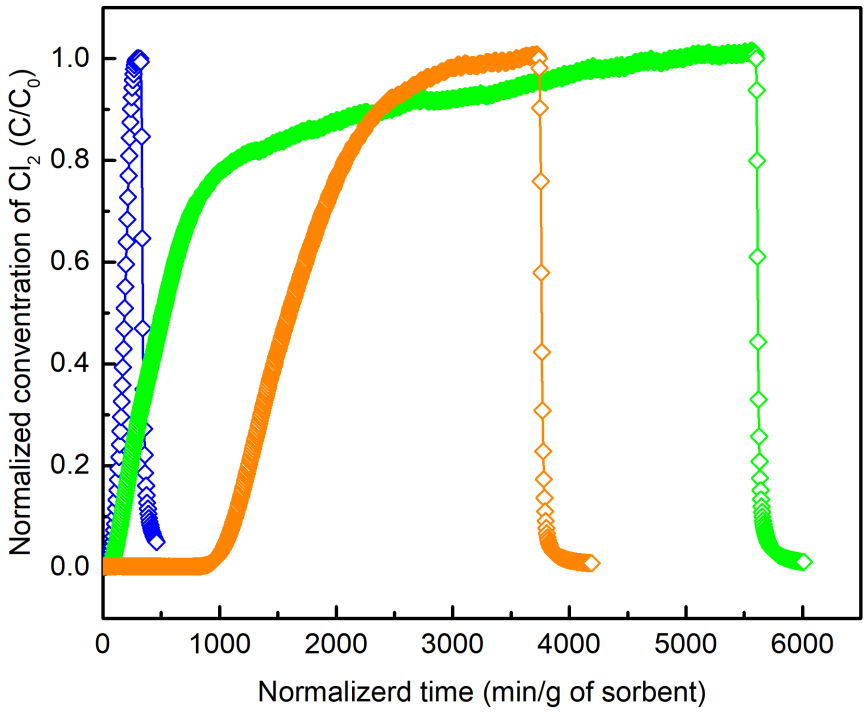

Figure 4.5: Chlorine Micro-Breakthrough and Desorption Curves Under Dry Condition for MOF-808 (Blue), MOF-808-BS (Green) and MOF-808-BD (Orange).

reacts with the double bond of the butadiene.

4.3 Experimental Details

4.3.1 General Procedures, Materials, and Instrumentation

All compounds and solvents were used as received unless otherwise noticed: 1,8-diazabicyclo(5.4.0)undec-7-ene (Aldrich, 98 %), 2,3-dibromopropionic acid (Aldrich, 98 %), acetic acid (ACP, 99.7 %), acetone (ACP, 99.5 %), acetonitrile (ACP, 99.5 %), dichloromethane (ACP, 99 %), deuterated dimethyl sulfoxide (DMSO-d_6) (Cambridge, 99.5 %), deuterated sulfuric acid (D_2SO_4/D_2O) (Aldrich, 99.5 atom % D),

ethyl alcohol (Aldrich, denatured), ethyl alcohol (ACP, 95 %), formic acid (BDH, 90 %), methanol (ACP, 99.8 %), *N,N*-dimethylformamide (DMF; Fisher, 99.9 %), piperazine (Aldrich, 99 %), sodium benzoate (Aldrich, 99 %), toluene (Fisher, 99.9 %), triethylamine (Aldrich, 99 %), trimesic acid (Aldrich, 95 %), zirconium(IV) oxychloride octahydrate (Aldrich, 99.5 %).

Powder X-ray diffraction (PXRD) patterns were obtained using a Rigaku X-ray Ultima IV Diffractometer equipped with a copper X-ray source and a scintillation counter detector.

^{1}H NMR experiments were performed on a 300 MHz Bruker Avance III 300 instrument. MOF samples were digested in D_2SO_4/DMSO-d_6 mix solution and filtered before measured by Bruker Avance III.

4.3.2 Microporous Breakthrough Reaction System

All the microporous breakthrough testing apparatus and the theory used here were previously reported.[85] The measurements were carried out under the conditions shown in Table 3.3 by our collaborator Dr. Jared DeCoste of the Edgewood Chemical Biological Center.

4.3.3 Synthesis of Ligands

4.3.3.1 1,4-Diazabicyclo[2.2.2]octane-2-Carboxylic Acid

The esterification of 2,3-dibromopropionic acid was carried out by the routine shown in Figure 4.6. 3.058 g (0.013 mol) 2,3-dibromopropionic acid was dissolved in 80.0 mL 100 % ethanol in a 100 mL round bottom flask before 2.0 mL of sulfuric acid and

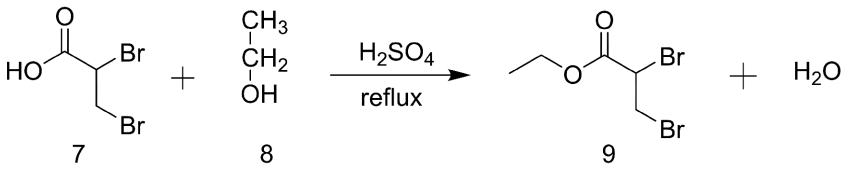

Figure 4.6: Scheme of Ethyl 2,3-Dibromopropionate Synthesis.

magnesium sulfate, as a drying agent (2.500 g), were added. The mixture was stirred and heated to 80–90 °C for 24 h. The filtrate was collected *via* gravity filtration and the solvent was removed by rotary evaporation. An orange-red oil was formed and characterized by ^{1}H NMR, which turned to be the desired product **9**, ethyl 2,3-dibromopropionate, with minor water impurity.

^{1}H NMR (300 MHz, Chloroform-*d*) δ 4.44 (t, J = 4.9 Hz, 1H), 4.30 (qd, J = 7.1 Hz, 2H), 3.98 – 3.88 (m, 1H), 3.69 (d, J = 4.9 Hz, 1H), 1.33 (t, J = 7.1 Hz, 3H).

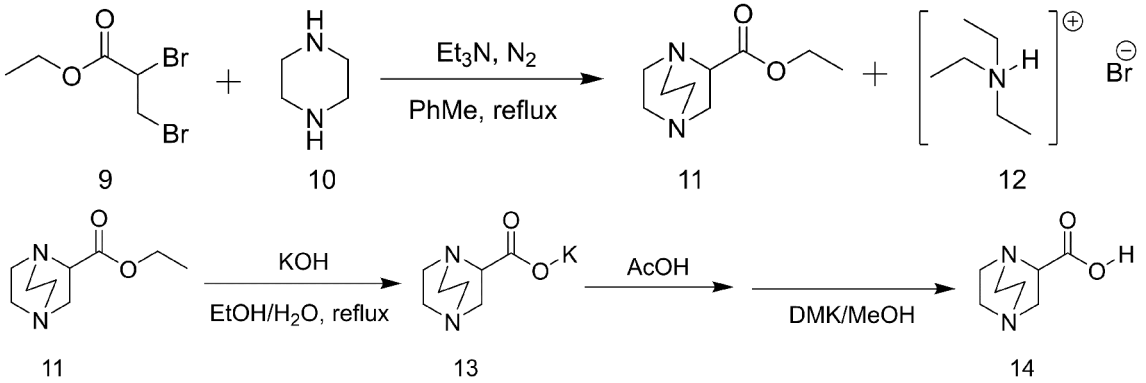

Figure 4.7: Scheme of 1,4-Diazabicyclo[2.2.2]octane-2-Carboxylic Acid Synthesis.

The synthesis of **14**, 1,4-diazabicyclo[2.2.2]octane-2-carboxylic acid, was carried out according to Hongling Li *et al.*'s work published in 2013 with minor changes (Figure 4.7).[216] Piperazine (1.840 g, 0.021 mol) and triethylamine (9.0 mL, 0.065 mol)

were dissolved in toluene (30.0 mL) in a 100 mL, 3-neck, round bottom flask under a nitrogen atmosphere. The solution was heated to 80-90 °C while stirring. Meanwhile, 2.4 mL (0.018 mol) ethyl 2,3-dibromopropionate was dissolved in 40.0 mL toluene before being added dropwisely to the previous mixture. A white solid formed immediately and the colourless solution became yellow. The reaction lasts for 30 h before being cooled down to ambient temperature. The solid was filtered and washed with two portions of 15.0 mL ethyl acetate. The solution was collected and rotary evaporated until an orange oil of **11** remained.

^{1}H NMR (300 MHz, Chloroform-*d*) δ 4.25 (q, J = 7.1 Hz, 2H), 3.47 (dd, J =8.1, 3.8 Hz, 1H), 3.11 – 2.64 (m, 10H), 1.29 (t, J = 7.1 Hz, 3H).

To form **14**, **11** (3.0 mL) and potassium hydroxide (5 M, 10.0 mL) were dissolved in mixture of ethanol/deionized water (30.0 mL/30.0 mL) and refluxed for 24 h at 85-90 °C. The mixture was subsequently rotary evaporated and the filtrate was adjusted to pH = 5–7 by glacial acetic acid; a small amount of white precipitate formed. After filtration, the solvent was removed by rotary evaporation to yield a brownish oil. The oil was dissolved in a minimal amount of methanol before acetone being added. A large amount of yellow precipitate formed after the acetone addition. The sample was filtered, dried in a vacuum oven at 80 °C for 24 h, yielding a white powder product of **14**.

^{1}H NMR (300 MHz, Deuterium Oxide) δ 3.53 – 3.10 (m). Due to the low symmetry of 11 protons having a similar chemical environment, no information regarding the purity of the sample was obtainable.

4.3.4 Synthesis of MOFs

MOF-808 was synthesized here by literature[124] with minor changes. It was dried in a vacuum oven for 24 h at ambient temperature first then another 24 h at 150 °C.

(I) MOF-808-BA: MOF-808 and excess saturated sodium benzoate solution were charged in round bottom flask for three days at ambient temperature, with stirring every two hours. The solid was subsequently filtered and washed with acetone, dried in a vacuum oven at 70 °C for 24 h, then 150 °C for another 24 h.

(II) MOF-808-DABCO: 35.4 mg 1,4-diazabicyclo[2.2.2]octane-2-carboxylic acid (**14**) was dissolved in 3.0 mL of water in a 2-dram vial before 21.3 mg MOF-808 was added. The heterogeneous mixture was mixed evenly and heated at 60 °C for 24 h. The mixture was washed with acetone, acetonitrile, and dichloromethane three times, respectively, then soaked in each for one day. The solid was subsequently filtered and dried at ambient temperature in a vacuum oven before a light yellow powder was formed.

References

[1] D. W. Schaefer, "Engineered porous materials," *MRS Bulletin*, vol. 19, no. 4, pp. 14–19, 1994.

[2] F. Fajula, A. Galarneau, and F. Di Renzo, "Advanced porous materials: New developments and emerging trends," *Microporous and Mesoporous Materials*, vol. 82, no. 3, pp. 227–239, 2005.

[3] M. E. Davis, "Ordered porous materials for emerging applications," *Nature*, vol. 417, no. 6891, pp. 813–821, 2002.

[4] B. A. Schrefler, "Mechanics and thermodynamics of saturated/unsaturated porous materials and quantitative solutions," *Applied Mechanics Reviews*, vol. 55, no. 4, pp. 351–388, 2002.

[5] M. O. Adebajo, R. L. Frost, J. T. Kloprogge, O. Carmody, and S. Kokot, "Porous materials for oil spill cleanup: a review of synthesis and absorbing properties," *Journal of Porous Materials*, vol. 10, no. 3, pp. 159–170, 2003.

[6] A. L. Myers and P. A. Monson, "Adsorption in porous materials at high pressure: theory and experiment," *Langmuir*, vol. 18, no. 26, pp. 10261–10273, 2002.

[7] C. M. Parlett, K. Wilson, and A. F. Lee, "Hierarchical porous materials: catalytic applications," *Chemical Society Reviews*, vol. 42, no. 9, pp. 3876–3893, 2013.

[8] T. A. Makal, J.-R. Li, W. Lu, and H.-C. Zhou, "Methane storage in advanced porous materials," *Chemical Society Reviews*, vol. 41, no. 23, pp. 7761–7779, 2012.

[9] E. J. Anglin, L. Cheng, W. R. Freeman, and M. J. Sailor, "Porous silicon in drug delivery devices and materials," *Advanced Drug Delivery Reviews*, vol. 60, no. 11, pp. 1266–1277, 2008.

[10] B. M. Weckhuysen and J. Yu, "Recent advances in zeolite chemistry and catalysis," *Chemical Society Reviews*, vol. 44, no. 20, pp. 7022–7024, 2015.

[11] Y. Ma, W. Tong, H. Zhou, and S. L. Suib, "A review of zeolite-like porous materials," *Microporous and Mesoporous Materials*, vol. 37, no. 1, pp. 243–252, 2000.

[12] S. Villar-Rodil, F. Suarez-Garcia, J. I. Paredes, A. Martinez-Alonso, and J. M. Tascon, "Activated carbon materials of uniform porosity from polyaramid fibers," *Chemistry of Materials*, vol. 17, no. 24, pp. 5893–5908, 2005.

[13] H.-C. Zhou, J. R. Long, and O. M. Yaghi, "Introduction to metal–organic frameworks," *Chemical Reviews*, vol. 112, no. 2, pp. 673–674, 2012.

[14] H.-C. Zhou and S. Kitagawa, "Metal–organic frameworks (MOFs)," *Chemical Society Reviews*, vol. 43, no. 16, pp. 5415–5418, 2014.

[15] W. Lu, Z. Wei, Z.-Y. Gu, T.-F. Liu, J. Park, J. Park, J. Tian, M. Zhang, Q. Zhang, T. Gentle III, M. Bosch, and H.-C. Zhou, "Tuning the structure and function of

metal–organic frameworks *via* linker design," *Chemical Society Reviews*, vol. 43, no. 16, pp. 5561–5593, 2014.

[16] A. Schneemann, V. Bon, I. Schwedler, I. Senkovska, S. Kaskel, and R. A. Fischer, "Flexible metal–organic frameworks," *Chemical Society Reviews*, vol. 43, no. 16, pp. 6062–6096, 2014.

[17] M. Peplow, "The hole story," *Nature*, vol. 520, no. 7546, pp. 148–150, 2015.

[18] O. M. Yaghi, M. O'keeffe, N. W. Ockwig, H. K. Chae, M. Eddaoudi, and J. Kim, "Reticular synthesis and the design of new materials," *Nature*, vol. 423, no. 6941, pp. 705–714, 2003.

[19] H. Deng, C. J. Doonan, H. Furukawa, R. B. Ferreira, J. Towne, C. B. Knobler, B. Wang, and O. M. Yaghi, "Multiple functional groups of varying ratios in metal–organic frameworks," *Science*, vol. 327, no. 5967, pp. 846–850, 2010.

[20] H. Deng, S. Grunder, K. E. Cordova, C. Valente, H. Furukawa, M. Hmadeh, F. Gándara, A. C. Whalley, Z. Liu, S. Asahina, H. Kazumori, M. O'Keeffe, O. Terasaki, J. F. Stoddart, and O. M. Yaghi, "Large-pore apertures in a series of metal–organic frameworks," *Science*, vol. 336, no. 6084, pp. 1018–1023, 2012.

[21] G. K. Shimizu, "Metal–organic frameworks: Model, make, measure," *Nature Chemistry*, vol. 2, no. 11, pp. 909–911, 2010.

[22] J. H. Cavka, S. Jakobsen, U. Olsbye, N. Guillou, C. Lamberti, S. Bordiga, and K. P. Lillerud, "A new zirconium inorganic building brick forming metal organic

frameworks with exceptional stability," *Journal of the American Chemical Society*, vol. 130, no. 42, pp. 13850–13851, 2008.

[23] M. J. Katz, Z. J. Brown, Y. J. Colón, P. W. Siu, K. A. Scheidt, R. Q. Snurr, J. T. Hupp, and O. K. Farha, "A facile synthesis of UiO-66, UiO-67 and their derivatives," *Chemical Communications*, vol. 49, no. 82, pp. 9449–9451, 2013.

[24] P. Deria, J. E. Mondloch, E. Tylianakis, P. Ghosh, W. Bury, R. Q. Snurr, J. T. Hupp, and O. K. Farha, "Perfluoroalkane functionalization of NU-1000 *via* solvent-assisted ligand incorporation: synthesis and CO_2 adsorption studies," *Journal of the American Chemical Society*, vol. 135, no. 45, pp. 16801–16804, 2013.

[25] S. Surblé, C. Serre, C. Mellot-Draznieks, F. Millange, and G. Férey, "A new isoreticular class of metal–organic frameworks with the MIL-88 topology," *Chemical Communications*, no. 3, pp. 284–286, 2006.

[26] D. Feng, Z.-Y. Gu, J.-R. Li, H.-L. Jiang, Z. Wei, and H.-C. Zhou, "Zirconium-metalloporphyrin PCN-222: mesoporous metal–organic frameworks with ultra-high stability as biomimetic catalysts," *Angewandte Chemie International Edition*, vol. 51, no. 41, pp. 10307–10310, 2012.

[27] H. Li, M. Eddaoudi, M. O'Keeffe, and O. M. Yaghi, "Design and synthesis of an exceptionally stable and highly porous metal–organic framework," *Nature*, vol. 402, no. 6759, pp. 276–279, 1999.

[28] K. S. Park, Z. Ni, A. P. Côté, J. Y. Choi, R. Huang, F. J. Uribe-Romo, H. K. Chae, M. O'Keeffe, and O. M. Yaghi, "Exceptional chemical and thermal stability of

zeolitic imidazolate frameworks," *Proceedings of the National Academy of Sciences*, vol. 103, no. 27, pp. 10186–10191, 2006.

[29] Y. Bai, Y. Dou, L.-H. Xie, W. Rutledge, J.-R. Li, and H.-C. Zhou, "Zr-based metal–organic frameworks: design, synthesis, structure, and applications," *Chemical Society Reviews*, vol. 45, no. 8, pp. 2327–2367, 2016.

[30] S. Yuan, L. Zou, H. Li, Y.-P. Chen, J. Qin, Q. Zhang, W. Lu, M. B. Hall, and H.-C. Zhou, "Flexible zirconium metal–organic frameworks as bioinspired switchable catalysts," *Angewandte Chemie International Edition*, vol. 55, no. 36, pp. 10776–10780, 2016.

[31] S. Yuan, Y.-P. Chen, J.-S. Qin, W. Lu, L. Zou, Q. Zhang, X. Wang, X. Sun, and H.-C. Zhou, "Linker installation: engineering pore environment with precisely placed functionalities in zirconium MOFs," *Journal of the American Chemical Society*, vol. 138, no. 28, pp. 8912–8919, 2016.

[32] T. C. Wang, W. Bury, D. A. Gómez-Gualdrón, N. A. Vermeulen, J. E. Mondloch, P. Deria, K. Zhang, P. Z. Moghadam, A. A. Sarjeant, R. Q. Snurr, J. F. Stoddart, J. T. Hupp, and O. K. Farha, "Ultrahigh surface area zirconium MOFs and insights into the applicability of the BET theory," *Journal of the American Chemical Society*, vol. 137, no. 10, pp. 3585–3591, 2015.

[33] N. L. Rosi, J. Kim, M. Eddaoudi, B. Chen, M. O'Keeffe, and O. M. Yaghi, "Rod packings and metal–organic frameworks constructed from rod-shaped secondary building units," *Journal of the American Chemical Society*, vol. 127, no. 5, pp. 1504–1518, 2005.

[34] P. D. Dietzel, R. E. Johnsen, R. Blom, and H. Fjellvåg, "Structural changes and coordinatively unsaturated metal atoms on dehydration of honeycomb analogous microporous metal–organic frameworks," *Chemistry-A European Journal*, vol. 14, no. 8, pp. 2389–2397, 2008.

[35] S. R. Caskey, A. G. Wong-Foy, and A. J. Matzger, "Dramatic tuning of carbon dioxide uptake *via* metal substitution in a coordination polymer with cylindrical pores," *Journal of the American Chemical Society*, vol. 130, no. 33, pp. 10870–10871, 2008.

[36] J.-R. Li, J. Sculley, and H.-C. Zhou, "Metal–organic frameworks for separations," *Chemical Reviews*, vol. 112, no. 2, pp. 869–932, 2011.

[37] M. P. Suh, H. J. Park, T. K. Prasad, and D.-W. Lim, "Hydrogen storage in metal–organic frameworks," *Chemical Reviews*, vol. 112, no. 2, pp. 782–835, 2011.

[38] K. Sumida, D. L. Rogow, J. A. Mason, T. M. McDonald, E. D. Bloch, Z. R. Herm, T.-H. Bae, and J. R. Long, "Carbon dioxide capture in metal–organic frameworks," *Chemical Reviews*, vol. 112, no. 2, pp. 724–781, 2012.

[39] H. Wu, Q. Gong, D. H. Olson, and J. Li, "Commensurate adsorption of hydrocarbons and alcohols in microporous metal organic frameworks," *Chemical Reviews*, vol. 112, no. 2, pp. 836–868, 2012.

[40] S. Chaemchuen, N. A. Kabir, K. Zhou, and F. Verpoort, "Metal–organic frameworks for upgrading biogas *via* CO_2 adsorption to biogas green energy," *Chemical Society Reviews*, vol. 42, no. 24, pp. 9304–9332, 2013.

[41] B. Van de Voorde, B. Bueken, J. Denayer, and D. De Vos, "Adsorptive separation on metal–organic frameworks in the liquid phase," *Chemical Society Reviews*, vol. 43, no. 16, pp. 5766–5788, 2014.

[42] N. A. Khan, Z. Hasan, and S. H. Jhung, "Adsorptive removal of hazardous materials using metal–organic frameworks (MOFs) : a review," *Journal of Hazardous Materials*, vol. 244, pp. 444–456, 2013.

[43] E. Barea, C. Montoro, and J. A. Navarro, "Toxic gas removal–metal–organic frameworks for the capture and degradation of toxic gases and vapours," *Chemical Society Reviews*, vol. 43, no. 16, pp. 5419–5430, 2014.

[44] J. B. DeCoste and G. W. Peterson, "Metal–organic frameworks for air purification of toxic chemicals," *Chemical Reviews*, vol. 114, no. 11, pp. 5695–5727, 2014.

[45] R. Schlögl, "Heterogeneous catalysis," *Angewandte Chemie International Edition*, vol. 54, no. 11, pp. 3465–3520, 2015.

[46] A. Dhakshinamoorthy, A. M. Asiri, and H. García, "Metal–organic framework (MOF) compounds: photocatalysts for redox reactions and solar fuel production," *Angewandte Chemie International Edition*, vol. 55, no. 18, pp. 5414–5445, 2016.

[47] Y. Liu, A. J. Howarth, N. A. Vermeulen, S.-Y. Moon, J. T. Hupp, and O. K. Farha, "Catalytic degradation of chemical warfare agents and their simulants by metal–organic frameworks," *Coordination Chemistry Reviews*, vol. 346, pp. 101–111, 2017.

[48] A. H. Chughtai, N. Ahmad, H. A. Younus, A. Laypkov, and F. Verpoort, "Metal–organic frameworks: versatile heterogeneous catalysts for efficient catalytic organic transformations," *Chemical Society Reviews*, vol. 44, no. 19, pp. 6804–6849, 2015.

[49] L. Wang, Y. Han, X. Feng, J. Zhou, P. Qi, and B. Wang, "Metal–organic frameworks for energy storage: Batteries and supercapacitors," *Coordination Chemistry Reviews*, vol. 307, pp. 361–381, 2016.

[50] H. Wang, Q.-L. Zhu, R. Zou, and Q. Xu, "Metal–organic frameworks for energy applications," *Chem*, vol. 2, no. 1, pp. 52–80, 2017.

[51] A. L. Balch and K. Winkler, "Two-component polymeric materials of fullerenes and the transition metal complexes: A bridge between metal–organic frameworks and conducting polymers," *Chemical Reviews*, vol. 116, no. 6, pp. 3812–3882, 2016.

[52] L. E. Kreno, K. Leong, O. K. Farha, M. Allendorf, R. P. Van Duyne, and J. T. Hupp, "Metal–organic framework materials as chemical sensors," *Chemical Reviews*, vol. 112, no. 2, pp. 1105–1125, 2012.

[53] M. Zhang, Z.-Y. Gu, M. Bosch, Z. Perry, and H.-C. Zhou, "Biomimicry in metal–organic materials," *Coordination Chemistry Reviews*, vol. 293, pp. 327–356, 2015.

[54] M. Giménez-Marqués, T. Hidalgo, C. Serre, and P. Horcajada, "Nanostructured metal–organic frameworks and their bio-related applications," *Coordination Chemistry Reviews*, vol. 307, pp. 342–360, 2016.

[55] P. Horcajada, R. Gref, T. Baati, P. K. Allan, G. Maurin, P. Couvreur, G. Férey, R. E. Morris, and C. Serre, "Metal–organic frameworks in biomedicine," *Chemical Reviews*, vol. 112, no. 2, pp. 1232–1268, 2011.

[56] L. Sun, M. G. Campbell, and M. Dincă, "Electrically conductive porous metal–organic frameworks," *Angewandte Chemie International Edition*, vol. 55, no. 11, pp. 3566–3579, 2016.

[57] R. N. Amador, M. Carboni, and D. Meyer, "Photosensitive titanium and zirconium metal organic frameworks: current research and future possibilities," *Materials Letters*, vol. 166, pp. 327–338, 2016.

[58] V. Stavila, A. A. Talin, and M. D. Allendorf, "MOF-based electronic and opto-electronic devices," *Chemical Society Reviews*, vol. 43, no. 16, pp. 5994–6010, 2014.

[59] O. M. Yaghi, G. Li, and H. Li, "Selective binding and removal of guests in a microporous metal–organic framework," *Nature*, vol. 378, no. 6558, pp. 703–706, 1995.

[60] M. Eddaoudi, J. Kim, N. Rosi, D. Vodak, J. Wachter, M. O'keeffe, and O. M. Yaghi, "Systematic design of pore size and functionality in isoreticular MOFs and their application in methane storage," *Science*, vol. 295, no. 5554, pp. 469–472, 2002.

[61] N. L. Rosi, J. Eckert, M. Eddaoudi, D. T. Vodak, J. Kim, M. O'keeffe, and O. M. Yaghi, "Hydrogen storage in microporous metal–organic frameworks," *Science*, vol. 300, no. 5622, pp. 1127–1129, 2003.

[62] J. E. Mondloch, O. Karagiaridi, O. K. Farha, and J. T. Hupp, "Activation of metal–organic framework materials," *CrystEngComm*, vol. 15, no. 45, pp. 9258–9264, 2013.

[63] P. Atkins and J. d. Paula, *Atkins's physical chemistry*. Oxford University Press, 2010.

[64] D. J. Collins and H.-C. Zhou, "Hydrogen storage in metal–organic frameworks," *Journal of Materials Chemistry*, vol. 17, no. 30, pp. 3154–3160, 2007.

[65] L. J. Murray, M. Dincă, and J. R. Long, "Hydrogen storage in metal–organic frameworks," *Chemical Society Reviews*, vol. 38, no. 5, pp. 1294–1314, 2009.

[66] R. B. Getman, Y.-S. Bae, C. E. Wilmer, and R. Q. Snurr, "Review and analysis of molecular simulations of methane, hydrogen, and acetylene storage in metal–organic frameworks," *Chemical Reviews*, vol. 112, no. 2, pp. 703–723, 2012.

[67] S. S. Kaye, A. Dailly, O. M. Yaghi, and J. R. Long, "Impact of preparation and handling on the hydrogen storage properties of Zn_4O(1,4-benzenedicarboxylate)$_3$ (MOF-5)," *Journal of the American Chemical Society*, vol. 129, no. 46, pp. 14176–14177, 2007.

[68] J. L. Rowsell, A. R. Millward, K. S. Park, and O. M. Yaghi, "Hydrogen sorption in functionalized metal–organic frameworks," *Journal of the American Chemical Society*, vol. 126, no. 18, pp. 5666–5667, 2004.

[69] L. Pan, M. B. Sander, X. Huang, J. Li, M. Smith, E. Bittner, B. Bockrath, and J. K. Johnson, "Microporous metal organic materials: promising candidates as

sorbents for hydrogen storage," *Journal of the American Chemical Society*, vol. 126, no. 5, pp. 1308–1309, 2004.

[70] A. G. Wong-Foy, A. J. Matzger, and O. M. Yaghi, "Exceptional H_2 saturation uptake in microporous metal–organic frameworks," *Journal of the American Chemical Society*, vol. 128, no. 11, pp. 3494–3495, 2006.

[71] W. Zhou, H. Wu, M. R. Hartman, and T. Yildirim, "Hydrogen and methane adsorption in metal–organic frameworks: a high-pressure volumetric study," *The Journal of Physical Chemistry C*, vol. 111, no. 44, pp. 16131–16137, 2007.

[72] O. K. Farha, A. Ö. Yazaydın, I. Eryazici, C. D. Malliakas, B. G. Hauser, M. G. Kanatzidis, S. T. Nguyen, R. Q. Snurr, and J. T. Hupp, "*De novo* synthesis of a metal–organic framework material featuring ultrahigh surface area and gas storage capacities," *Nature Chemistry*, vol. 2, no. 11, pp. 944–948, 2010.

[73] P. Jaramillo, W. M. Griffin, and H. S. Matthews, "Comparative life-cycle air emissions of coal, domestic natural gas, LNG, and SNG for electricity generation," *Environmental Science & Technology*, vol. 41, no. 17, pp. 6290–6296, 2007.

[74] B. Li, H.-M. Wen, W. Zhou, J. Q. Xu, and B. Chen, "Porous metal–organic frameworks: Promising materials for methane storage," *Chem*, vol. 1, no. 4, pp. 557–580, 2016.

[75] Y. He, W. Zhou, G. Qian, and B. Chen, "Methane storage in metal–organic frameworks," *Chemical Society Reviews*, vol. 43, no. 16, pp. 5657–5678, 2014.

[76] Y. Peng, V. Krungleviciute, I. Eryazici, J. T. Hupp, O. K. Farha, and T. Yildirim, "Methane storage in metal–organic frameworks: current records, surprise findings, and challenges," *Journal of the American Chemical Society*, vol. 135, no. 32, pp. 11887–11894, 2013.

[77] S. Solomon, G.-K. Plattner, R. Knutti, and P. Friedlingstein, "Irreversible climate change due to carbon dioxide emissions," *Proceedings of the National Academy of Sciences*, vol. 106, no. 6, pp. 1704–1709, 2009.

[78] T. J. Crowley and R. A. Berner, "CO_2 and climate change," *Science*, vol. 292, no. 5518, pp. 870–872, 2001.

[79] J.-R. Li, Y. Ma, M. C. McCarthy, J. Sculley, J. Yu, H.-K. Jeong, P. B. Balbuena, and H.-C. Zhou, "Carbon dioxide capture-related gas adsorption and separation in metal–organic frameworks," *Coordination Chemistry Reviews*, vol. 255, no. 15, pp. 1791–1823, 2011.

[80] J. A. Botas, G. Calleja, M. Sánchez-Sánchez, and M. G. Orcajo, "Cobalt doping of the MOF-5 framework and its effect on gas-adsorption properties," *Langmuir*, vol. 26, no. 8, pp. 5300–5303, 2010.

[81] A. H. Goldstein, C. D. Koven, C. L. Heald, and I. Y. Fung, "Biogenic carbon and anthropogenic pollutants combine to form a cooling haze over the southeastern united states," *Proceedings of the National Academy of Sciences*, vol. 106, no. 22, pp. 8835–8840, 2009.

[82] V. Ramanathan and Y. Feng, "Air pollution, greenhouse gases and climate change: Global and regional perspectives," *Atmospheric Environment*, vol. 43, no. 1, pp. 37–50, 2009.

[83] T. Teichert, M. Vossoughi, A. Vierkötter, D. Sugiri, T. Schikowski, T. Schulte, M. Roden, C. Luckhaus, C. Herder, and U. Krämer, "Association between traffic-related air pollution, subclinical inflammation and impaired glucose metabolism: results from the SALIA study," *PLoS One*, vol. 8, no. 12, p. e83042, 2013.

[84] D. Vallero, *Fundamentals of air pollution*. Academic press, 2014.

[85] T. G. Glover, G. W. Peterson, B. J. Schindler, D. Britt, and O. Yaghi, "MOF-74 building unit has a direct impact on toxic gas adsorption," *Chemical Engineering Science*, vol. 66, no. 2, pp. 163–170, 2011.

[86] A. Dhakshinamoorthy, M. Alvaro, and H. Garcia, "Metal–organic frameworks as heterogeneous catalysts for oxidation reactions," *Catalysis Science & Technology*, vol. 1, no. 6, pp. 856–867, 2011.

[87] Q.-L. Zhu, J. Li, and Q. Xu, "Immobilizing metal nanoparticles to metal–organic frameworks with size and location control for optimizing catalytic performance," *Journal of the American Chemical Society*, vol. 135, no. 28, pp. 10210–10213, 2013.

[88] J. Lee, O. K. Farha, J. Roberts, K. A. Scheidt, S. T. Nguyen, and J. T. Hupp, "Metal–organic framework materials as catalysts," *Chemical Society Reviews*, vol. 38, no. 5, pp. 1450–1459, 2009.

[89] A. Corma, H. Garcia, and F. X. Llabrés i Xamena, "Engineering metal organic frameworks for heterogeneous catalysis," *Chemical Reviews*, vol. 110, no. 8, pp. 4606–4655, 2010.

[90] J. Liu, L. Chen, H. Cui, J. Zhang, L. Zhang, and C.-Y. Su, "Applications of metal–organic frameworks in heterogeneous supramolecular catalysis," *Chemical Society Reviews*, vol. 43, no. 16, pp. 6011–6061, 2014.

[91] U. Ravon, M. E. Domine, C. Gaudillere, A. Desmartin-Chomel, and D. Farrusseng, "MOFs as acid catalysts with shape selectivity properties," *New Journal of Chemistry*, vol. 32, no. 6, pp. 937–940, 2008.

[92] D. Sun, Y. Fu, W. Liu, L. Ye, D. Wang, L. Yang, X. Fu, and Z. Li, "Studies on photocatalytic CO_2 reduction over NH_2-UiO-66 (Zr) and its derivatives: Towards a better understanding of photocatalysis on metal–organic frameworks," *Chemistry-A European Journal*, vol. 19, no. 42, pp. 14279–14285, 2013.

[93] C. M. Granadeiro, S. O. Ribeiro, M. Karmaoui, R. Valença, J. C. Ribeiro, B. de Castro, L. Cunha-Silva, and S. S. Balula, "Production of ultra-deep sulfur-free diesels using a sustainable catalytic system based on UiO-66 (Zr)," *Chemical Communications*, vol. 51, no. 72, pp. 13818–13821, 2015.

[94] O. Zybaylo, O. Shekhah, H. Wang, M. Tafipolsky, R. Schmid, D. Johannsmann, and C. Wöll, "A novel method to measure diffusion coefficients in porous metal–organic frameworks," *Physical Chemistry Chemical Physics*, vol. 12, no. 28, pp. 8093–8098, 2010.

[95] D. Banerjee, Z. Hu, S. Pramanik, X. Zhang, H. Wang, and J. Li, "Vapor phase detection of nitroaromatic and nitroaliphatic explosives by fluorescence active metal–organic frameworks," *CrystEngComm*, vol. 15, no. 45, pp. 9745–9750, 2013.

[96] S. S. Nagarkar, B. Joarder, A. K. Chaudhari, S. Mukherjee, and S. K. Ghosh, "Highly selective detection of nitro explosives by a luminescent metal–organic framework," *Angewandte Chemie International Edition*, vol. 52, no. 10, pp. 2881–2885, 2013.

[97] N. Stock and S. Biswas, "Synthesis of metal–organic frameworks (MOFs): routes to various MOF topologies, morphologies, and composites," *Chemical Reviews*, vol. 112, no. 2, pp. 933–969, 2011.

[98] A. Rabenau, "The role of hydrothermal synthesis in preparative chemistry," *Angewandte Chemie International Edition*, vol. 24, no. 12, pp. 1026–1040, 1985.

[99] U. Mueller, M. Schubert, F. Teich, H. Puetter, K. Schierle-Arndt, and J. Pastré, "Metal–organic frameworks-prospective industrial applications," *Journal of Materials Chemistry*, vol. 16, no. 7, pp. 626–636, 2006.

[100] D. M. D'Alessandro, B. Smit, and J. R. Long, "Carbon dioxide capture: prospects for new materials," *Angewandte Chemie International Edition*, vol. 49, no. 35, pp. 6058–6082, 2010.

[101] J. A. Mason, K. Sumida, Z. R. Herm, R. Krishna, and J. R. Long, "Evaluating metal–organic frameworks for post-combustion carbon dioxide capture *via* temperature swing adsorption," *Energy & Environmental Science*, vol. 4, no. 8, pp. 3030–3040, 2011.

[102] D.-J. Lee, Q. Li, H. Kim, and K. Lee, "Preparation of Ni-MOF-74 membrane for CO_2 separation by layer-by-layer seeding technique," *Microporous and Mesoporous Materials*, vol. 163, pp. 169–177, 2012.

[103] R. Lyndon, K. Konstas, A. W. Thornton, A. J. Seeber, B. P. Ladewig, and M. R. Hill, "Visible light-triggered capture and release of CO_2 from stable metal–organic frameworks," *Chemistry of Materials*, vol. 27, no. 23, pp. 7882–7888, 2015.

[104] T. M. McDonald, J. A. Mason, X. Kong, E. D. Bloch, D. Gygi, A. Dani, V. Crocella, F. Giordanino, S. O. Odoh, W. S. Drisdell, B. Vlaisavljevich, A. L. Dzubak, R. Poloni, S. K. Schnell, N. Planas, K. Lee, T. Pascal, L. F. Wan, D. Prendergast, J. B. Neaton, B. Smit, J. B. Kortright, L. Gagliardi, S. Bordiga, J. A. Reimer, and J. R. Long, "Cooperative insertion of CO_2 in diamine-appended metal–organic frameworks," *Nature*, vol. 519, no. 7543, p. 303, 2015.

[105] Z. Qiao, N. Wang, J. Jiang, and J. Zhou, "Design of amine-functionalized metal–organic frameworks for CO_2 separation: the more amine, the better?," *Chemical Communications*, vol. 52, no. 5, pp. 974–977, 2016.

[106] U. Müller, H. Pütter, M. Hesse, H. Wessel, M. Schubert, J. Huff, and M. Guzmann, "Verfahren zur elektrochemischen herstellung eines kristallinen porösen metallorganischen gerüstmaterials," June 2 2005. WO Patent App. PCT/EP2004/013,236.

[107] R. Ameloot, L. Pandey, M. Van der Auweraer, L. Alaerts, B. F. Sels, and D. E. De Vos, "Patterned film growth of metal–organic frameworks based on galvanic displacement," *Chemical Communications*, vol. 46, no. 21, pp. 3735–3737, 2010.

[108] M. Schlesinger, S. Schulze, M. Hietschold, and M. Mehring, "Evaluation of synthetic methods for microporous metal–organic frameworks exemplified by the competitive formation of $[Cu_2(BTC)_3(H_2O)_3]$ and $[Cu_2(BTC)(OH)(H_2O)]$," *Microporous and Mesoporous Materials*, vol. 132, no. 1, pp. 121–127, 2010.

[109] M. Hartmann, S. Kunz, D. Himsl, O. Tangermann, S. Ernst, and A. Wagener, "Adsorptive separation of isobutene and isobutane on $Cu_3(BTC)_2$," *Langmuir*, vol. 24, no. 16, pp. 8634–8642, 2008.

[110] R. Ameloot, L. Stappers, J. Fransaer, L. Alaerts, B. F. Sels, and D. E. De Vos, "Patterned growth of metal–organic framework coatings by electrochemical synthesis," *Chemistry of Materials*, vol. 21, no. 13, pp. 2580–2582, 2009.

[111] J. S. Benjamin, "Dispersion strengthened superalloys by mechanical alloying," *Metallurgical Transactions*, vol. 1, no. 10, pp. 2943–2951, 1970.

[112] A. Delori, T. Friščić, and W. Jones, "The role of mechanochemistry and supramolecular design in the development of pharmaceutical materials," *CrystEngComm*, vol. 14, no. 7, pp. 2350–2362, 2012.

[113] L. Takacs, "Self-sustaining reactions induced by ball milling," *Progress in Materials Science*, vol. 47, no. 4, pp. 355–414, 2002.

[114] A. Stolle, T. Szuppa, S. E. Leonhardt, and B. Ondruschka, "Ball milling in organic synthesis: solutions and challenges," *Chemical Society Reviews*, vol. 40, no. 5, pp. 2317–2329, 2011.

[115] T. Friščić, "Supramolecular concepts and new techniques in mechanochemistry: cocrystals, cages, rotaxanes, open metal–organic frameworks," *Chemical Society Reviews*, vol. 41, no. 9, pp. 3493–3510, 2012.

[116] A. Pichon, A. Lazuen-Garay, and S. L. James, "Solvent-free synthesis of a microporous metal–organic framework," *CrystEngComm*, vol. 8, no. 3, pp. 211–214, 2006.

[117] P. J. Beldon, L. Fábián, R. S. Stein, A. Thirumurugan, A. K. Cheetham, and T. Friščić, "Rapid room-temperature synthesis of zeolitic imidazolate frameworks by using mechanochemistry," *Angewandte Chemie International Edition*, vol. 49, no. 50, pp. 9640–9643, 2010.

[118] T. Friščić, "New opportunities for materials synthesis using mechanochemistry," *Journal of Materials Chemistry*, vol. 20, no. 36, pp. 7599–7605, 2010.

[119] W. Yuan, T. Friščić, D. Apperley, and S. L. James, "High reactivity of metal–organic frameworks under grinding conditions: parallels with organic molecular materials," *Angewandte Chemie*, vol. 122, no. 23, pp. 4008–4011, 2010.

[120] T. D. Bennett, S. Cao, J. C. Tan, D. A. Keen, E. G. Bithell, P. J. Beldon, T. Friščić, and A. K. Cheetham, "Facile mechanosynthesis of amorphous zeolitic imidazolate frameworks," *Journal of the American Chemical Society*, vol. 133, no. 37, pp. 14546–14549, 2011.

[121] T. Friščić, P. A. Julien, and C. Mottillo, "Environmentally-friendly designs and syntheses of metal–organic frameworks (MOFs)," in *Green Technologies for the Environment*, pp. 161–183, ACS Publications, 2014.

[122] D. Prochowicz, K. Sokołowski, I. Justyniak, A. Kornowicz, D. Fairen-Jimenez, T. Friščić, and J. Lewiński, "A mechanochemical strategy for IRMOF assembly based on pre-designed oxo-zinc precursors," *Chemical Communications*, vol. 51, no. 19, pp. 4032–4035, 2015.

[123] K. Užarević, T. C. Wang, S.-Y. Moon, A. M. Fidelli, J. T. Hupp, O. K. Farha, and T. Friščić, "Mechanochemical and solvent-free assembly of zirconium-based metal–organic frameworks," *Chemical Communications*, vol. 52, no. 10, pp. 2133–2136, 2016.

[124] H. Furukawa, F. Gándara, Y.-B. Zhang, J. Jiang, W. L. Queen, M. R. Hudson, and O. M. Yaghi, "Water adsorption in porous metal–organic frameworks and related materials," *Journal of the American Chemical Society*, vol. 136, no. 11, pp. 4369–4381, 2014.

[125] J. Jiang, F. Gándara, Y.-B. Zhang, K. Na, O. M. Yaghi, and W. G. Klemperer, "Superacidity in sulfated metal–organic framework-808," *Journal of the American Chemical Society*, vol. 136, no. 37, pp. 12844–12847, 2014.

[126] J. Klinowski, F. A. A. Paz, P. Silva, and J. Rocha, "Microwave-assisted synthesis of metal–organic frameworks," *Dalton Transactions*, vol. 40, no. 2, pp. 321–330, 2011.

[127] M. Taddei, P. V. Dau, S. M. Cohen, M. Ranocchiari, J. A. van Bokhoven, F. Costantino, S. Sabatini, and R. Vivani, "Efficient microwave assisted synthesis of metal–organic framework UiO-66: optimization and scale up," *Dalton Transactions*, vol. 44, no. 31, pp. 14019–14026, 2015.

[128] V. I. Isaeva, A. L. Tarasov, L. E. Starannikova, Y. P. Yampol'skii, A. Y. Alent'ev, and L. M. Kustov, "Microwave-assisted synthesis of mesoporous metal–organic framework NH_2-MIL-101 (Al)," *Russian Chemical Bulletin*, vol. 64, no. 12, pp. 2791–2795, 2015.

[129] Z.-J. Lin, Z. Yang, T.-F. Liu, Y.-B. Huang, and R. Cao, "Microwave-assisted synthesis of a series of lanthanide metal–organic frameworks and gas sorption properties," *Inorganic Chemistry*, vol. 51, no. 3, pp. 1813–1820, 2012.

[130] P. J. Dunn, "The importance of green chemistry in process research and development," *Chemical Society Reviews*, vol. 41, no. 4, pp. 1452–1461, 2012.

[131] H. Reinsch, ""Green" synthesis of metal–organic frameworks," *European Journal of Inorganic Chemistry*, vol. 2016, no. 27, pp. 4290–4299, 2016.

[132] A. D. Burrows, *The Chemistry of Metal–Organic Frameworks. Synthesis, Characterization, and Applications, 2 Volumes. Edited by Stefan Kaskel.* Wiley Online Library, 2017.

[133] A. D. Burrows, K. Cassar, R. M. Friend, M. F. Mahon, S. P. Rigby, and J. E. Warren, "Solvent hydrolysis and templating effects in the synthesis of metal–organic frameworks," *CrystEngComm*, vol. 7, no. 89, pp. 548–550, 2005.

[134] J. Clayton Jr, J. Barnes, D. Hood, and G. W. Schepers, "The inhalation toxicity of dimethylformamide (DMF)," *American Industrial Hygiene Association Journal*, vol. 24, no. 2, pp. 144–154, 1963.

[135] C. A. Redlich, W. S. Beckett, J. Sparer, K. W. Barwick, C. A. Riely, H. Miller, S. L. Sigal, S. L. Shalat, and M. R. Cullen, "Liver disease associated with occupational exposure to the solvent dimethylformamide," *Annals of Internal Medicine*, vol. 108, no. 5, pp. 680–686, 1988.

[136] D. W. Lynch, "NTP technical report on the toxicity studies of *N,N-Dimethylformamide* (CAS No. 68-12-2) administered by inhalation to F344/N rats and B6C3F1 mice.," *Toxicity Report Series*, vol. 22, pp. 1–D20, 1992.

[137] G. Long, B. Meek, and M. Lewis, *N,N-Dimethylformamide*. Geneva: World Health Organization, 2001.

[138] D. W. Lynch, M. E. Placke, R. Persing, and M. Ryan, "Thirteen-week inhalation toxicity of *N,N-dimethylformamide in F344/N rats and B6C3F1* mice," *Toxicological Sciences*, vol. 72, no. 2, pp. 347–358, 2003.

[139] "Regulation (EC) No 1907/2006 of the European Parliament and of the Council," 18 December 2006. Concerning the Registration, Evaluation, Authorisation and Restriction of Chemicals (REACH), establishing a European Chemicals Agency, amending Directive 1999/45/EC and repealing Council Regulation (EEC) No 793/93 and Commission Regulation (EC) No 1488/94 as well as Council Directive 76/769/EEC and Commission Directives 91/155/EEC, 93/67/EEC, 93/105/EC and 2000/21/EC.

[140] J. Sherwood, A. Constantinou, L. Moity, C. R. McElroy, T. J. Farmer, T. Duncan, W. Raverty, A. J. Hunt, and J. H. Clark, "Dihydrolevoglucosenone (Cyrene) as

a bio-based alternative for dipolar aprotic solvents," *Chemical Communications*, vol. 50, no. 68, pp. 9650–9652, 2014.

[141] S. Shafiee and E. Topal, "When will fossil fuel reserves be diminished?," *Energy Policy*, vol. 37, no. 1, pp. 181–189, 2009.

[142] C. Withagen, "Pollution and exhaustibility of fossil fuels," *Resource and Energy Economics*, vol. 16, no. 3, pp. 235–242, 1994.

[143] R. A. Berner, "The long-term carbon cycle, fossil fuels and atmospheric composition," *Nature*, vol. 426, no. 6964, pp. 323–326, 2003.

[144] A. A. Fatah, J. A. Barrett, R. D. Arcilisi Jr, K. J. Ewing, C. H. Lattin, M. S. Helinski, and I. A. Baig, "Guide for the selection of chemical and biological decontamination equipment for emergency first responders, NIJ Guide 103-00, Volume I," 2001.

[145] F. R. Sidell and J. Borak, "Chemical warfare agents: II. nerve agents," *Annals of Emergency Medicine*, vol. 21, no. 7, pp. 865–871, 1992.

[146] J. Ott, V. Gronemann, F. Pontzen, E. Fiedler, G. Grossmann, D. B. Kersebohm, G. Weiss, and C. Witte, *Ullmann's encyclopedia of industrial chemistry*. Germany: Wiley-VCH, 2012.

[147] W. A. Andrews, *Guide to the study of environmental pollution*. NJ, Prentice-Hall, 1972.

[148] J. H. Clark, T. J. Farmer, A. J. Hunt, and J. Sherwood, "Opportunities for bio-based solvents created as petrochemical and fuel products transition towards re-

newable resources," *International Journal of Molecular Sciences*, vol. 16, no. 8, pp. 17101–17159, 2015.

[149] C. M. Hansen, *Hansen solubility parameters: a user's handbook*. CRC press, 2007.

[150] J. B. DeCoste, M. S. Denny Jr, G. W. Peterson, J. J. Mahle, and S. M. Cohen, "Enhanced aging properties of HKUST-1 in hydrophobic mixed-matrix membranes for ammonia adsorption," *Chemical Science*, vol. 7, no. 4, pp. 2711–2716, 2016.

[151] N. C. Jeong, B. Samanta, C. Y. Lee, O. K. Farha, and J. T. Hupp, "Coordination-chemistry control of proton conductivity in the iconic metal–organic framework material HKUST-1," *Journal of the American Chemical Society*, vol. 134, no. 1, pp. 51–54, 2011.

[152] J. Moellmer, A. Moeller, F. Dreisbach, R. Glaeser, and R. Staudt, "High pressure adsorption of hydrogen, nitrogen, carbon dioxide and methane on the metal–organic framework HKUST-1," *Microporous and Mesoporous Materials*, vol. 138, no. 1, pp. 140–148, 2011.

[153] A. S. Münch and F. O. Mertens, "HKUST-1 as an open metal site gas chromatographic stationary phase-capillary preparation, separation of small hydrocarbons and electron donating compounds, determination of thermodynamic data," *Journal of Materials Chemistry*, vol. 22, no. 20, pp. 10228–10234, 2012.

[154] B. Sun, S. Kayal, and A. Chakraborty, "Study of HKUST (copper benzene-1,3,5-tricarboxylate, Cu-BTC MOF)-1 metal–organic frameworks for CH_4 adsorption: an experimental investigation with GCMC (grand canonical Monte-carlo) simulation," *Energy*, vol. 76, pp. 419–427, 2014.

[155] J. L. Rowsell and O. M. Yaghi, "Effects of functionalization, catenation, and variation of the metal oxide and organic linking units on the low-pressure hydrogen adsorption properties of metal–organic frameworks," *Journal of the American Chemical Society*, vol. 128, no. 4, pp. 1304–1315, 2006.

[156] C. G. P. Ltd., *Safety Data Sheet: Dihydrolevoglucosenone*. Circa Group Pty Ltd., 2017.

[157] M. E. Silvestre, M. Franzreb, P. G. Weidler, O. Shekhah, and C. Wöll, "Magnetic cores with porous coatings: Growth of metal–organic frameworks on particles using liquid phase epitaxy," *Advanced Functional Materials*, vol. 23, no. 9, pp. 1210–1213, 2013.

[158] C. A. Trickett, K. J. Gagnon, S. Lee, F. Gándara, H.-B. Bürgi, and O. M. Yaghi, "Definitive molecular level characterization of defects in UiO-66 crystals," *Angewandte Chemie International Edition*, vol. 54, no. 38, pp. 11162–11167, 2015.

[159] D. Sun, Y. Fu, W. Liu, L. Ye, D. Wang, L. Yang, X. Fu, and Z. Li, "Studies on photocatalytic CO_2 reduction over NH_2-UiO-66 (Zr) and its derivatives: Towards a better understanding of photocatalysis on metal–organic frameworks," *Chemistry-A European Journal*, vol. 19, no. 42, pp. 14279–14285, 2013.

[160] G. Calleja, R. Sanz, G. Orcajo, D. Briones, P. Leo, and F. Martínez, "Copper-based MOF-74 material as effective acid catalyst in Friedel–Crafts acylation of anisole," *Catalysis Today*, vol. 227, pp. 130–137, 2014.

[161] A. J. Rieth, Y. Tulchinsky, and M. Dincă, "High and reversible ammonia uptake in mesoporous azolate metal–organic frameworks with open Mn, Co, and Ni sites," *Journal of the American Chemical Society*, vol. 138, no. 30, pp. 9401–9404, 2016.

[162] P. A. Julien, K. Užarević, A. D. Katsenis, S. A. Kimber, T. Wang, O. K. Farha, Y. Zhang, J. Casaban, L. S. Germann, M. Etter, R. Dinnebier, S. L. James, I. Halasz, and T. Friščić, "*In situ* monitoring and mechanism of the mechanochemical formation of a microporous MOF-74 framework," *Journal of the American Chemical Society*, vol. 138, no. 9, pp. 2929–2932, 2016.

[163] S.-H. Cho, B. Ma, S. T. Nguyen, J. T. Hupp, and T. E. Albrecht-Schmitt, "A metal–organic framework material that functions as an enantioselective catalyst for olefin epoxidation," *Chemical Communications*, no. 24, pp. 2563–2565, 2006.

[164] A. M. Shultz, A. A. Sarjeant, O. K. Farha, J. T. Hupp, and S. T. Nguyen, "Post-synthesis modification of a metal–organic framework to form metallosalen-containing MOF materials," *Journal of the American Chemical Society*, vol. 133, no. 34, pp. 13252–13255, 2011.

[165] L. K. Cadman, J. K. Bristow, N. E. Stubbs, D. Tiana, M. F. Mahon, A. Walsh, and A. D. Burrows, "Compositional control of pore geometry in multivariate metal–organic frameworks: an experimental and computational study," *Dalton Transactions*, vol. 45, no. 10, pp. 4316–4326, 2016.

[166] Y. Kim, R. Haldar, H. Kim, J. Koo, and K. Kim, "The guest-dependent thermal response of the flexible MOF $Zn_2(BDC)_2(DABCO)$," *Dalton Transactions*, vol. 45, no. 10, pp. 4187–4192, 2016.

[167] H. K. Kim, W. S. Yun, M.-B. Kim, J. Y. Kim, Y.-S. Bae, J. Lee, and N. C. Jeong, "A chemical route to activation of open metal sites in the copper-based metal–organic framework materials HKUST-1 and Cu-MOF-2," *Journal of the American Chemical Society*, vol. 137, no. 31, pp. 10009–10015, 2015.

[168] Z. Hu, S. Faucher, Y. Zhuo, Y. Sun, S. Wang, and D. Zhao, "Combination of optimization and metalated-ligand exchange: an effective approach to functionalize UiO-66 (Zr) MOFs for CO_2 separation," *Chemistry-A European Journal*, vol. 21, no. 48, pp. 17246–17255, 2015.

[169] L. Garzón-Tovar, A. Carné-Sánchez, C. Carbonell, I. Imaz, and D. Maspoch, "Optimised room temperature, water-based synthesis of CPO-27-M metal–organic frameworks with high space-time yields," *Journal of Materials Chemistry A*, vol. 3, no. 41, pp. 20819–20826, 2015.

[170] Z. Liang, M. Marshall, and A. L. Chaffee, "CO_2 adsorption, selectivity and water tolerance of pillared-layer metal organic frameworks," *Microporous and Mesoporous Materials*, vol. 132, no. 3, pp. 305–310, 2010.

[171] A. J. Howarth, M. J. Katz, T. C. Wang, A. E. Platero-Prats, K. W. Chapman, J. T. Hupp, and O. K. Farha, "High efficiency adsorption and removal of selenate and selenite from water using metal–organic frameworks," *Journal of the American Chemical Society*, vol. 137, no. 23, pp. 7488–7494, 2015.

[172] T. C. Wang, N. A. Vermeulen, I. S. Kim, A. B. Martinson, J. F. Stoddart, J. T. Hupp, and O. K. Farha, "Scalable synthesis and post-modification of a mesoporous

metal–organic framework called NU-1000," *Nature protocols*, vol. 11, no. 1, p. 149, 2016.

[173] D. N. Dybtsev, H. Chun, and K. Kim, "Rigid and flexible: A highly porous metal–organic framework with unusual guest-dependent dynamic behavior," *Angewandte Chemie International Edition*, vol. 43, no. 38, pp. 5033–5036, 2004.

[174] D. J. Babu, F. G. Kühl, S. Yadav, D. Markert, M. Bruns, M. J. Hampe, and J. J. Schneider, "Adsorption of pure SO_2 on nanoscaled graphene oxide," *RSC Advances*, vol. 6, no. 43, pp. 36834–36839, 2016.

[175] C. Stiehler, F. Calaza, W.-D. Schneider, N. Nilius, and H.-J. Freund, "Molecular adsorption changes the quantum structure of oxide-supported gold nanoparticles: chemisorption versus physisorption," *Physical Review Letters*, vol. 115, no. 3, p. 036804, 2015.

[176] A. Franceschetti, S. J. Pennycook, and S. T. Pantelides, "Oxygen chemisorption on Au nanoparticles," *Chemical Physics Letters*, vol. 374, no. 5, pp. 471–475, 2003.

[177] H. Yabu, T. Jinno, K. Koike, T. Higuchi, and M. Shimomura, "Three-dimensional assembly of gold nanoparticles in spherically confined microphase-separation structures of block copolymers," *Macromolecules*, vol. 44, no. 15, pp. 5868–5873, 2011.

[178] V. Kirichenko, Y. Filatov, and A. Budyka, "Electrospinning of micro-and nanofibers: fundamentals in separation and filtration processes," *International Journal for Multiscale Computational Engineering*, vol. 8, no. 4, 2010.

[179] E. Armstrong and C. O'Dwyer, "Artificial opal photonic crystals and inverse opal structures–fundamentals and applications from optics to energy storage," *Journal of Materials Chemistry C*, vol. 3, no. 24, pp. 6109–6143, 2015.

[180] A. C. Pierre and G. M. Pajonk, "Chemistry of aerogels and their applications," *Chemical Reviews*, vol. 102, no. 11, pp. 4243–4266, 2002.

[181] Y. Si, Q. Fu, X. Wang, J. Zhu, J. Yu, G. Sun, and B. Ding, "Superelastic and superhydrophobic nanofiber-assembled cellular aerogels for effective separation of oil/water emulsions," *ACS Nano*, vol. 9, no. 4, pp. 3791–3799, 2015.

[182] A. Walcarius and M. M. Collinson, "Analytical chemistry with silica sol-gels: traditional routes to new materials for chemical analysis," *Annual Review of Analytical Chemistry*, vol. 2, pp. 121–143, 2009.

[183] H. Sai, R. Fu, L. Xing, J. Xiang, Z. Li, F. Li, and T. Zhang, "Surface modification of bacterial cellulose aerogels' web-like skeleton for oil/water separation," *ACS Applied Materials & Interfaces*, vol. 7, no. 13, pp. 7373–7381, 2015.

[184] S. Sircar, T. C. Golden, and M. B. Rao, "Activated carbon for gas separation and storage," *Carbon*, vol. 34, no. 1, pp. 1–12, 1996.

[185] L. Li, P. A. Quinlivan, and D. R. Knappe, "Effects of activated carbon surface chemistry and pore structure on the adsorption of organic contaminants from aqueous solution," *Carbon*, vol. 40, no. 12, pp. 2085–2100, 2002.

[186] R. V. Siriwardane, M.-S. Shen, E. P. Fisher, and J. A. Poston, "Adsorption of CO_2 on molecular sieves and activated carbon," *Energy & Fuels*, vol. 15, no. 2, pp. 279–284, 2001.

[187] H. Sun, A. Li, Z. Zhu, W. Liang, X. Zhao, P. La, and W. Deng, "Superhydrophobic activated carbon-coated sponges for separation and absorption," *ChemSusChem*, vol. 6, no. 6, pp. 1057–1062, 2013.

[188] S. C. Sarkar and A. Bose, "Role of activated carbon pellets in carbon dioxide removal," *Energy Conversion and Management*, vol. 38, pp. S105–S110, 1997.

[189] K.-T. Chue, J.-N. Kim, Y.-J. Yoo, S.-B. Cho, and R. T. Yang, "Comparison of activated carbon and zeolite 13X for CO_2 recovery from flue gas by pressure swing adsorption," *Industrial & Engineering Chemistry Research*, vol. 34, no. 2, pp. 591–598, 1995.

[190] K. Kusakabe, T. Kuroda, A. Murata, and S. Morooka, "Formation of a y-type zeolite membrane on a porous α-alumina tube for gas separation," *Industrial & Engineering Chemistry Research*, vol. 36, no. 3, pp. 649–655, 1997.

[191] Z. Lai, G. Bonilla, I. Diaz, J. G. Nery, K. Sujaoti, M. A. Amat, E. Kokkoli, O. Terasaki, R. W. Thompson, M. Tsapatsis, and D. G. Vlachos, "Microstructural optimization of a zeolite membrane for organic vapor separation," *Science*, vol. 300, no. 5618, pp. 456–460, 2003.

[192] R. Krishna and J. M. Van Baten, "Using molecular simulations for screening of zeolites for separation of CO_2/CH_4 mixtures," *Chemical Engineering Journal*, vol. 133, no. 1, pp. 121–131, 2007.

[193] N. B. Shukla and G. Madras, "Kinetics of adsorption of methylene blue and rhodamine 6G on acrylic acid-based superabsorbents," *Journal of Applied Polymer Science*, vol. 126, no. 2, pp. 463–472, 2012.

[194] D. Cooney, *Adsorption Design for Wastewater Treatment*. Taylor & Francis, 1998.

[195] B. Deguin and P. Vogel, "Hetero-Diels-Alder addition of sulfur dioxide to 1,3-dienes. suprafaciality, regioselectivity, and stereoselectivity," *Journal of the American Chemical Society*, vol. 114, no. 23, pp. 9210–9211, 1992.

[196] D. Suárez, J. González, T. L. Sordo, and J. A. Sordo, "*Ab Initio* study of the thermal and Lewis acid-catalyzed hetero-Diels-Alder reactions of 1,3-butadiene and isoprene with sulfur dioxide," *The Journal of Organic Chemistry*, vol. 59, no. 26, pp. 8058–8064, 1994.

[197] D. Zheng and J. Wu, *Sulfur Dioxide Insertion Reactions for Organic Synthesis*. Springer, 2017.

[198] P. J. Harrington and K. A. DiFiore, "A preparation of 3-aryl-2,5-dihydrothiophene-1,1-dioxides from aryl iodides," *Tetrahedron Letters*, vol. 28, no. 5, pp. 495–498, 1987.

[199] G. S. Andrade, J. E. Berkner, C. L. Liotta, C. Eckert, D. A. Schiraldi, A. Andersen, and D. M. Collard, "The one-pot synthesis and Diels-Alder reactivity of 2,5-dihydrothiophene-1,1-dioxide-3-carboxylic acid," *Synthetic Communications*, vol. 33, no. 20, pp. 3643–3650, 2003.

[200] M. J. Katz, S.-Y. Moon, J. E. Mondloch, M. H. Beyzavi, C. J. Stephenson, J. T. Hupp, and O. K. Farha, "Exploiting parameter space in mofs: a 20-fold enhancement of phosphate-ester hydrolysis with UiO-66-NH_2," *Chemical Science*, vol. 6, no. 4, pp. 2286–2291, 2015.

[201] V. Guillerm, S. Gross, C. Serre, T. Devic, M. Bauer, and G. Férey, "A zirconium methacrylate oxocluster as precursor for the low-temperature synthesis of porous zirconium (IV) dicarboxylates," *Chemical Communications*, vol. 46, no. 5, pp. 767–769, 2010.

[202] H. Wu, Y. S. Chua, V. Krungleviciute, M. Tyagi, P. Chen, T. Yildirim, and W. Zhou, "Unusual and highly tunable missing-linker defects in zirconium metal–organic framework UiO-66 and their important effects on gas adsorption," *Journal of the American Chemical Society*, vol. 135, no. 28, pp. 10525–10532, 2013.

[203] G. C. Shearer, S. Chavan, J. Ethiraj, J. G. Vitillo, S. Svelle, U. Olsbye, C. Lamberti, S. Bordiga, and K. P. Lillerud, "Tuned to perfection: ironing out the defects in metal–organic framework UiO-66," *Chemistry of Materials*, vol. 26, no. 14, pp. 4068–4071, 2014.

[204] C. A. Trickett, K. J. Gagnon, S. Lee, F. Gándara, H.-B. Bürgi, and O. M. Yaghi, "Definitive molecular level characterization of defects in UiO-66 crystals," *Angewandte Chemie International Edition*, vol. 54, no. 38, pp. 11162–11167, 2015.

[205] P. Ghosh, Y. J. Colón, and R. Q. Snurr, "Water adsorption in UiO-66: the importance of defects," *Chemical Communications*, vol. 50, no. 77, pp. 11329–11331, 2014.

[206] S. Øien, D. Wragg, H. Reinsch, S. Svelle, S. Bordiga, C. Lamberti, and K. P. Lillerud, "Detailed structure analysis of atomic positions and defects in zirconium metal–organic frameworks," *Crystal Growth & Design*, vol. 14, no. 11, pp. 5370–5372, 2014.

[207] M. J. Cliffe, J. A. Hill, C. A. Murray, F.-X. Coudert, and A. L. Goodwin, "Defect-dependent colossal negative thermal expansion in UiO-66 (Hf) metal–organic framework," *Physical Chemistry Chemical Physics*, vol. 17, no. 17, pp. 11586–11592, 2015.

[208] G. C. Shearer, S. Chavan, S. Bordiga, S. Svelle, U. Olsbye, and K. P. Lillerud, "Defect engineering: tuning the porosity and composition of the metal–organic framework UiO-66 *via* modulated synthesis," *Chemistry of Materials*, vol. 28, no. 11, pp. 3749–3761, 2016.

[209] S. Ling and B. Slater, "Dynamic acidity in defective UiO-66," *Chemical Science*, vol. 7, no. 7, pp. 4706–4712, 2016.

[210] G. Fini and B. Fortunato, "Raman and IR spectra of 3-sulfolene," *Spectrochimica Acta Part A: Molecular Spectroscopy*, vol. 32, no. 2, pp. 423–426, 1976.

[211] J. B. DeCoste, T. J. Demasky, M. J. Katz, O. K. Farha, and J. T. Hupp, "A UiO-66 analogue with uncoordinated carboxylic acids for the broad-spectrum removal of toxic chemicals," *New Journal of Chemistry*, vol. 39, no. 4, pp. 2396–2399, 2015.

[212] V. K. Ol'khovik, A. A. Pap, V. Vasilevskii, N. A. Galinovskii, and S. Tereshko, "Synthesis and properties of luminophores derived from fluorinated biphenyls," *Russian Journal of Organic Chemistry*, vol. 44, no. 8, pp. 1172–1179, 2008.

[213] S. Sengupta and S. Bhattacharyya, "A facile synthesis of 3-arylbutadiene sulfones," *Synthetic Communications*, vol. 26, no. 2, pp. 231–236, 1996.

[214] V. K. Ol'khovik, V. Vasilevskii, and N. A. Galinovskii, "Synthesis of new poly-conjugated compounds based on 9,10-diphenylphenanthrene," *Russian Journal of Organic Chemistry*, vol. 46, no. 8, pp. 1167–1172, 2010.

[215] H. Woolven, C. González-Rodríguez, I. Marco, A. L. Thompson, and M. C. Willis, "DABCO-bis (sulfur dioxide), DABSO, as a convenient source of sulfur dioxide for organic synthesis: utility in sulfonamide and sulfamide preparation," *Organic Letters*, vol. 13, no. 18, pp. 4876–4878, 2011.

[216] H. Li, M. Yang, X. Zhang, L. Yan, J. Li, and Y. Qi, "Mesoporous silica-supported copper-catalysts for homocoupling reaction of terminal alkynes at room-temperature," *New Journal of Chemistry*, vol. 37, no. 5, pp. 1343–1349, 2013.